# Scalable Spin Squeezing for Quantum-Enhanced Magnetometry with Bose-Einstein Condensates

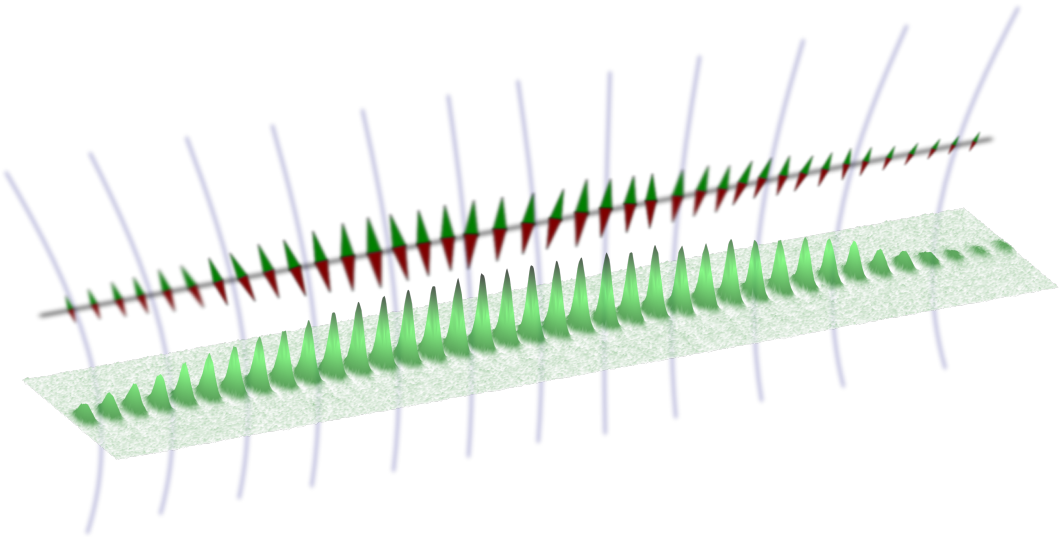

Wolfgang Müssel

2014

Dissertation

submitted to the

Combined Faculties of the Natural Sciences and Mathematics

of the Ruperto-Carola-University of Heidelberg. Germany

for the degree of

Doctor of Natural Sciences

Put forward by

Wolfgang Müssel

born in: Schwäbisch Hall, Germany

Oral examination: 17 December 2014

# Scalable Spin Squeezing for Quantum-Enhanced Magnetometry with Bose-Einstein Condensates

Referees: Prof. Dr. Markus K. Oberthaler
Prof. Dr. Philipp Treutlein

# Abstract

In this thesis, we experimentally study the generation of metrologically useful *spin squeezed states* and investigate their scalability to large atom numbers. Two different experimental schemes that generate these entangled spin states are implemented for two internal states of a Bose-Einstein condensate. We investigate both the previously realized *one-axis twisting scenario* and a new method which relies on the quantum evolution at an unstable fixed point, which we term *bifurcation squeezing*. The temporal evolution and the atom number dependence of the final states are examined for both schemes, and the optimal conditions for the creation of squeezing are extracted. We find spin squeezing below $-7$ dB in this two-mode scenario.

By use of parallelized squeezing generation of up to 30 independent condensates in a one-dimensional lattice potential, we show that the squeezing of the individual condensates can be scaled up to the full ensemble containing more than 12 300 atoms. With a differential analysis, which rejects common mode fluctuations, we find a suppression of fluctuations by $\xi^2_{\text{rel}} = -5.3(5)$ dB for the full ensemble. We directly demonstrate the applicability of this quantum resource for enhanced magnetometry, which is implemented via a modified Ramsey sequence. A transfer to a different set of hyperfine states ensures negligible nonlinearity during the interrogation time and strongly enhances the magnetic sensitivity. We find a quantum-enhanced single-shot sensitivity of $310(47)$ pT with the full ensemble, and apply the technique for an accurate determination of the magnetic field gradient in our setup.

# Zusammenfassung

Diese Arbeit beschäftigt sich mit der Herstellung so genannter *gequetschter* verschränkter Zustände in einem Bose-Einstein-Kondensat und deren Skalierbarkeit zu großen Atomzahlen. Zunächst werden dabei zwei Herstellungsverfahren analysiert. Neben der bereits mehrfach eingesetzten *one-axis twisting*-Methode untersuchen wir eine neuartige Technik, die auf der Quantendynamik an einem instabilen Fixpunkt beruht und als *Bifurkations-Methode* bezeichnet wird. Wir analysieren die Zeitentwicklung sowie die Atomzahlabhängigkeiten der Prozesse in einem einzelnen Kondensat und finden unter optimalen Bedigungen eine Unterdrückung der Quantenfluktuationen von mehr als 7 dB.

Durch parallele Herstellung gequetschter Zustände in bis zu 30 unabhängigen Kondensaten in einem optischen Gitter kann diese Rauschunterdrückung auf das gesamte Ensemble von mehr als 12 300 Atomen übertragen werden. Eine Relativanalyse ergibt eine Reduktion der Fluktuationen von $\xi^2_{\text{rel}} = -5.3(5)$ dB für die hochskalierte Teilchenzahl. Die praktische Nutzbarkeit dieser Quantenressource demonstrieren wir, indem wir sie in einem quantenverstärkten Magnetometer einsetzen, das auf einer modifizierten Ramsey-Sequenz beruht. Hierbei wird durch einen Zustandstransfer während der Phasenevolutionszeit die magnetische Sensitivität erhöht und die nichtlineare Wechselwirkung stark reduziert. Dieses Magnetometer, das eine quantenmechanisch verbesserte Sensitivität von $310(47)$ pT pro Messpunkt besitzt, nutzen wir für die präzise Bestimmung eines Magnetfeldgradienten in unserem Experiment.

# Contents

# List of Figures

# 1. Introduction

Since the early days of quantum mechanics, entanglement has been one of its key concepts and subject of intriguing debates [1], as it constitutes one of the most counterintuitive predictions of quantum theory. In his seminal paper in 1935, Erwin Schrödinger even stated that he *'would not call that **one** but rather **the** characteristic trait of quantum mechanics, the one that enforces its entire departure from classical lines of thought'* [2].
Decades after these fundamental discussions on quantum correlations, entanglement now appears to be a central building block for future improvements in a variety of technological tasks, such as communication, computations or measurements. During the past thirty years, great advance has been made in the development of techniques for the generation of entanglement in a broad variety of systems, ranging from photonic [3] over ionic [4] and neutral atom [5] to solid state [6] implementations.
One of the major challenges in this context is the scalability of the methods both for creation and characterization of entangled states to large ensemble sizes, as the generation of entangled states with substantial particle numbers is a key prerequisite for practical applicability. This can be well understood in the context of metrology, where entanglement is a promising tool for enhancing the sensitivity of the measurement devices. In many of the state-of-the art instruments, the measurement uncertainty is limited by the statistical quantum fluctuations of the individual classical particles [7, 8, 9]. Quantum-mechanical correlations can reduce this uncertainty. Specifically, the sensitivity of a measurement device can be quantified in terms of the *Cramér-Rao bound* [10, 11]

$$\Delta\theta \geq \frac{1}{\sqrt{F_Q}} \geq \frac{1}{N}, \tag{1.1}$$

which relates the best attainable phase sensitivity $\Delta\theta$ of a measurement to its quantum resources, quantified by the quantum Fisher information $F_Q$. This quantity itself is bound by the number of employed particles $F_Q \leq N^2$, which is saturated only for maximally entangled states and yields the fundamental *Heisenberg limit* of the phase sensitivity $\Delta\theta \geq 1/N$ [12].
For a classical state without quantum correlations, the maximal quantum Fisher information is $F_Q \leq N$ and we find the well-known *shot noise limit* $\Delta\theta \geq 1/\sqrt{N}$. This has two consequences: First, a classical state with sufficiently larger atom number can in principle always outperform entangled input states in phase estimation. Thus, the application of entangled states only makes sense if the number of particles that can be used is constrained. Secondly, this means that in such a scenario, quantum entanglement can yield an enormous gain if a large enough entangled state can be engineered. This is the driving force behind the development of technologies for entanglement generation, characterization and, finally, the implementation in actual devices.

In the realm of quantum optics, the technological development has reached the level that squeezed states of light [13] are now routinely employed to enhance the precision of gravitational wave detectors [14], twenty-five years after their first experimental observation [15]. Multiparticle entanglement has been observed for up to eight optical photons [16] and up to ten qubits by exploiting hyper-entanglement of multiple of the photons' degrees of freedom [17]. For these multiparticle entangled states, the scaling to larger photon numbers is limited by the brightness of the available correlated photon sources [16].
Beautiful experiments in the microwave regime have studied the decoherence of such maximally entangled states made up from 11 photons in superconducting cavities [18]. Recent progress on superconducting solid state devices [19] has enabled the creation of a wide range of superposition states, including cat states containing up to 111 microwave photons, and a demonstration of Heisenberg limited phase estimation for up to 22.5 photons [6].

In the atomic world, a large variety of entangled states of several ions has been created, including an eight-qubit W state [20] and maximally entangled cat states of up to 14 ions [21, 22]. Proof-of-principle demonstrations with three ions have shown that such states can be employed for spectroscopy close to the Heisenberg limit [23]. However, the scalability to larger qubit numbers is difficult due to the necessity to reduce the speed of the entangling gates caused by the denser mode spectrum [4]. Also, it has been shown that the decay times of the generated maximally entangled states scale quadratically with the number of qubits [22].

The vast majority of these ionic systems uses a bottom-up approach, which relies on a series of entangling operations for the individual qubits. In contrast, most strategies that have been employed for neutral ground state atoms build on collective top-down operations with no direct experimental access to the single qubits.
Recently, entanglement of at least 13 atoms was detected in Dicke states of 41 atoms, which were generated in an optical fiber cavity by use of a projective measurement [24].
The most promising route and most active area of research, however, are spin squeezed states [25], which are relatively robust against decoherence and particle loss [26, 27, 28, 29] and can be obtained with a variety of different experimental systems and techniques.
Early work focused on transferring photonic entanglement to the atomic systems and the generation of conditional spin squeezing using quantum non-demolition measurements in thermal ensembles [30, 31, 32]. Since these first experimental observations, intense research has been put into generating such squeezed states in the ground states of those systems, creating spin squeezing that is applicable for Ramsey spectroscopy, and further reducing the back-action of the quantum non-demolition measurements [33, 34, 35, 36, 37, 38]. Impressive results have been obtained in this context, generating up to $10.2\,\mathrm{dB}$ of metrologically applicable squeezing for more than $10^5$ atoms [38]. A different technique relying on cavity feedback has demonstrated $5.6\,\mathrm{dB}$ of metrologically relevant unconditional squeezing for $5 \times 10^4$ atoms [39]. Experimental demonstrations have shown that these entangled states can be used to improve the performance of atomic clocks [40, 41] and cold atom magnetometers [37, 42].

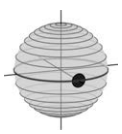

Even though many of these experiments are based on cold atomic clouds, a wide range of important applications necessitates even colder temperatures due to the requirement of interrogation times in the order of several seconds. For the experiments that are performed in microgravity or in large atomic fountains, temperatures in the order of 1 nanokelvin have to be achieved to limit the spread of the atomic cloud during free fall [43]. Additionally, ultralow temperatures allow to reach higher spatial resolution, as the timescale of diffusion grows with decreasing temperature. Their high densities and long coherence times make Bose-Einstein condensates (BECs) ideal systems for such measurements.

In Bose-Einstein condensates, squeezing via atom-light interaction has not yet been demonstrated so far. Successful generation of spin squeezed states in Bose-Einstein condensates has been based on interatomic interactions, a scheme which was proposed by *Sørensen et al.* as a pathway for creating many-particle entanglement [44]. Proof-of-principle experiments based on this proposal have shown the controlled creation of two-mode spin squeezed states in BECs of up to 1800 atoms [5, 45, 46, 47] and demonstrated the applicability of such states for quantum-enhanced metrology [45, 48].

Entangled states containing larger atom numbers have been created by spin-mixing dynamics in a three-mode system [49, 50, 51], including $-10.3\,\mathrm{dB}$ of quadrature squeezing in a SU(2) subspace of the SU(3) system containing 45 000 particles [52]. However, the actual implementation of measurement applications using three-mode systems is non-trivial, and it has not yet been shown that this *spin-nematic* squeezing can be metrologically exploited. In contrast, two-mode systems are routinely employed for the measurement of a wide range of quantities, such as accelerations, rotations, magnetic fields and frequencies [53, 54, 55, 56, 57].

For those squeezed two-mode systems in Bose-Einstein condensates, increasing the number of atoms to large system sizes has been shown to be challenging due to the presence of increased losses as well as dephasing and mixing of the different spatial modes [28, 58, 59]. In this thesis, we will present a method that, based on the controlled generation of many replica in a one-dimensional lattice potential, allows the scaling of such squeezed states in Bose-Einstein condensates to large particle numbers. It evades the spurious effects of strongly increased losses or multi-mode dynamics on the generated states, and transfers the well-controlled generation of small spin squeezed condensates to the macroscopic regime.

In terms of practical applicability, another difficulty arises in our experimental system from the fact that the squeezed states are generated on two levels with increased nonlinearity, which is caused by their asymmetric interaction strengths. This strong nonlinearity is required for production of the entangled states, but cannot easily be switched off, as it is enhanced by an interspecies Feshbach resonance. In this thesis, we will demonstrate that the spin squeezed states can be transferred to a different set of internal levels which have negligible nonlinearity. As the chosen levels in our situation are magnetically sensitive, we can implement a quantum-enhanced Ramsey magnetometer with our upscaled resource and use it to measure a magnetic field gradient in our setup. This experimental demonstration of state swapping could also be employed for precision measurements of other quantities, depending on the choice of the final levels, and shows the broad applicability of the generated entangled resource.



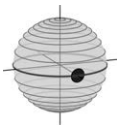

This thesis is structured as follows. After this introduction, in Chapter 2 we will present a basic theoretical description for the interacting binary Bose-Einstein condensate with tunable linear interconversion which was employed for the results presented in this thesis. Chapter 3 will give an overview of our experimental system, including an introduction to the absorption imaging system that was used for the detection of our atomic clouds, and will show the experimental characterization of the parameters that govern the internal dynamics in our system. The basic analysis methods and the resulting dynamics of the *one-axis twisting* squeezing Hamiltonian for the condensates in single lattice sites will be described in Chapter 4, along with a characterization of the generated states in terms of spin squeezing. Chapter 5 will describe the analogous results for the temporal evolution of a quantum system that is prepared on an unstable fixed point, and demonstrate that this instability can be employed for generating entanglement using *bifurcation squeezing*. In Chapter 6, we will show how the resources of the single lattice sites can be combined to scale up the number of particles in the two-mode squeezed states to large system sizes, and analyze the technical fluctuations that limit a direct analysis. We will conclude this thesis with the demonstration of a quantum-enhanced magnetometer building on this upscaled resource, and analyze the performance of this device.
The results dealing with the scalability of the squeezed states and their application for magnetometry are summarized in a publication [60]. Related work showing the generation of entangled non-Gaussian spin states in the unstable fixed point scenario and their characterization using Fisher information was published in [61]. A detailed characterization of the employed absorption imaging system is given in [62], and an alternative detection method using fluorescence imaging was explored in [63].

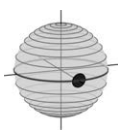

# 2. Theory of an Interacting Two-Mode Bose-Einstein Condensate with Linear Coupling

This chapter provides an introduction into the basic theoretical concepts which are relevant for this thesis. We will start by discussing the Hamiltonian of an interacting two-mode Bose-Einstein condensate, and derive a description in a pseudospin representation. Afterwards, we will show how an internal Bosonic Josephson Junction can be realized in such a system by the addition of linear interconversion. The basic concepts of coherent spin states, the visualization of collective atomic states on a generalized Bloch sphere, and spin squeezing will be introduced. Finally, we will discuss the mean field limit of our Hamiltonian and show how the quantum dynamics of the system can be understood from the topology of the corresponding classical phase space.

## 2.1. Hamiltonian of an Interacting Binary Condensate

In the following, we will consider an interacting Bose-Einstein condensate of atoms in the two modes $|a\rangle$ and $|b\rangle$, which are two internal eigenstates of the employed atomic species. The two atomic states interact via elastic scattering, parametrized by their respective intraspecies scattering lengths $a_{aa}$ and $a_{bb}$ and the interspecies scattering length $a_{ab}$.
The Hamiltonian of this system can be written in the form

$$\mathcal{H} = \mathcal{H}_a + \mathcal{H}_b + \mathcal{H}_{ab}, \tag{2.1}$$

where $\mathcal{H}_a$ and $\mathcal{H}_b$ denote the Hamiltonians for each of the individual components, and $\mathcal{H}_{ab}$ describes their interspecies interaction. In second quantization, the single-component Hamiltonian for $|a\rangle$, occupying the spatial mode $\psi_a(\mathbf{x})$ and experiencing an external potential $V_a(\mathbf{x})$, is given by [64, 65]

$$\mathcal{H}_a = \int \mathrm{d}^3\mathbf{x}\, \hat{\psi}_a^{\dagger}(\mathbf{x}) \left( -\frac{\hbar^2}{2m}\nabla^2 + V_a(\mathbf{x}) + \frac{4\pi a_{aa}}{2m}\hat{\psi}_a^{\dagger}(\mathbf{x})\hat{\psi}_a(\mathbf{x}) \right) \hat{\psi}_a(\mathbf{x}), \tag{2.2}$$

where $m$ denotes the atomic mass. The second component $|b\rangle$ can be described by an analogous Hamiltonian, and the interspecies interaction is captured by

$$\mathcal{H}_{ab} = \frac{4\pi a_{ab}}{m} \int \mathrm{d}^3\mathbf{x}\, \hat{\psi}_a^{\dagger}(\mathbf{x})\hat{\psi}_b^{\dagger}(\mathbf{x})\hat{\psi}_a(\mathbf{x})\hat{\psi}_b(\mathbf{x}). \tag{2.3}$$

We define the interaction strengths $g_{ij} = \frac{4\pi a_{ij}}{m}$ and assume that all atoms of each component are in a single spatial wave function, such that we can replace the field operators $\hat{\psi}_a^\dagger(\mathbf{x}) = \hat{a}_a^\dagger \phi_a(\mathbf{x})$ and $\hat{\psi}_b^\dagger(\mathbf{x}) = \hat{a}_b^\dagger \phi_b(\mathbf{x})$. Here $\hat{a}_{a,b}^\dagger$ and $\hat{a}_{a,b}$ are the bosonic creation and annihilation operators fulfilling the commutation relations $[\hat{a}_i, \hat{a}_j^\dagger] = \delta_{ij}$ and $[\hat{a}_i^\dagger, \hat{a}_j^\dagger] = [\hat{a}_i, \hat{a}_j] = 0$, and $\phi_{a,b}(\mathbf{x})$ are normalized single-particle wave functions. We thus find for the combined Hamiltonians of the individual species

$$\begin{aligned}\mathcal{H}_a + \mathcal{H}_b = \frac{1}{2}\int \mathrm{d}^3\mathbf{x}\, \Big[&\phi_a(\mathbf{x})\omega_a\phi_a(\mathbf{x})\hat{a}_a^\dagger\hat{a}_a + g_{aa}|\phi_a(\mathbf{x})|^4\hat{a}_a^\dagger\hat{a}_a^\dagger\hat{a}_a\hat{a}_a \\ &+\phi_b(\mathbf{x})\omega_b\phi_b(\mathbf{x})\hat{a}_b^\dagger\hat{a}_b + g_{bb}|\phi_b(\mathbf{x})|^4\hat{a}_b^\dagger\hat{a}_b^\dagger\hat{a}_b\hat{a}_b\Big],\end{aligned} \tag{2.4}$$

using the single-particle Hamiltonians of each component $\omega_i = -\frac{\hbar^2}{2m}\nabla^2 + V_a(\mathbf{x})$. The inter-component interaction term is then given by

$$\mathcal{H}_{ab} = \int \mathrm{d}^3\mathbf{x}\, g_{ab}|\phi_a(\mathbf{x})|^2|\phi_b(\mathbf{x})|^2 \cdot \hat{a}_a^\dagger\hat{a}_b^\dagger\hat{a}_a\hat{a}_b. \tag{2.5}$$

Using the definitions

$$\tilde{\omega}_i = \int \mathrm{d}^3\mathbf{x}\, \phi_i(\mathbf{x})\omega_i\phi_i(\mathbf{x}), \tag{2.6}$$

$$\chi_{ii} = \int \mathrm{d}^3\mathbf{x}\, g_{ii}|\phi_i(\mathbf{x})|^4, \text{ and} \tag{2.7}$$

$$\chi_{ij} = \int \mathrm{d}^3\mathbf{x}\, g_{ij}|\phi_i(\mathbf{x})|^2|\phi_j(\mathbf{x})|^2, \tag{2.8}$$

we can rewrite the full Hamiltonian in the two-mode approximation:

$$\mathcal{H} = \tilde{\omega}_a\hat{a}_a^\dagger\hat{a}_a + \tilde{\omega}_b\hat{a}_b^\dagger\hat{a}_b + \frac{\chi_{aa}}{2}\hat{a}_a^\dagger\hat{a}_a^\dagger\hat{a}_a\hat{a}_a + \frac{\chi_{bb}}{2}\hat{a}_b^\dagger\hat{a}_b^\dagger\hat{a}_b\hat{a}_b + \chi_{ab}\hat{a}_a^\dagger\hat{a}_b^\dagger\hat{a}_a\hat{a}_b \tag{2.9}$$

## 2.2. Pseudospin Representation

### 2.2.1. Pseudospin Operators

We can now introduce an angular momentum representation [66] to describe this system, employing the pseudospin operators

$$\hat{J}_x = \frac{1}{2}(\hat{a}_a^\dagger\hat{a}_b + \hat{a}_b^\dagger\hat{a}_a) \tag{2.10}$$

$$\hat{J}_y = \frac{1}{2i}(\hat{a}_b^\dagger\hat{a}_a - \hat{a}_a^\dagger\hat{a}_b) \tag{2.11}$$

$$\hat{J}_z = \frac{1}{2}(\hat{a}_b^\dagger\hat{a}_b - \hat{a}_a^\dagger\hat{a}_a), \tag{2.12}$$

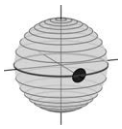

which satisfy the SU(2) angular momentum commutation relation

$$[\hat{J}_i, \hat{J}_j] = \mathrm{i}\epsilon_{ijk}\hat{J}_k. \tag{2.13}$$

The $z$ component of the angular momentum is proportional to the population difference $\hat{N}_b - \hat{N}_a = 2\hat{J}_z$ of the two components, and the $x$ and $y$ components are the corresponding coherences of the two-level system.
Employing

$$\hat{J} = \frac{1}{2}\left(\hat{a}_a^\dagger \hat{a}_a + \hat{a}_b^\dagger \hat{a}_b\right) = \frac{N}{2} \tag{2.14}$$

with $N$ being the constant total number of particles, and

$$\hat{\mathbf{J}}^2 = J(J+1) \tag{2.15}$$

with $J = \langle \hat{J} \rangle = N/2$, we find the identities

$$\hat{a}_a^\dagger \hat{a}_a = \hat{J} - \hat{J}_z, \tag{2.16}$$
$$\hat{a}_b^\dagger \hat{a}_b = \hat{J} + \hat{J}_z, \tag{2.17}$$
$$\hat{a}_a^\dagger \hat{a}_a^\dagger \hat{a}_a \hat{a}_a = -2\hat{J} + \hat{\mathbf{J}}^2 - (2\hat{J} - 1)\hat{J}_z + \hat{J}_z^2, \tag{2.18}$$
$$\hat{a}_b^\dagger \hat{a}_b^\dagger \hat{a}_b \hat{a}_b = -2\hat{J} + \hat{\mathbf{J}}^2 + (2\hat{J} - 1)\hat{J}_z + \hat{J}_z^2, \text{ and} \tag{2.19}$$
$$\hat{a}_b^\dagger \hat{a}_b^\dagger \hat{a}_a \hat{a}_a = \hat{\mathbf{J}}^2 - \hat{J}_z^2 - \hat{J}. \tag{2.20}$$

### 2.2.2. One-Axis Twisting Hamiltonian in Spin Representation

We can use Eq. 2.16-2.20 to rewrite the Hamiltonian Eq. 2.9 in the pseudospin representation, yielding

$$\begin{aligned}\mathcal{H} = \left(\frac{\chi_{aa}}{2} + \frac{\chi_{bb}}{2} + \chi_{ab}\right)\hat{\mathbf{J}}^2 + \left(\tilde{\omega}_a + \tilde{\omega}_b - \chi_{aa} - \chi_{bb} - \chi_{ab}\right)\hat{J} \\ + \left(\tilde{\omega}_b - \tilde{\omega}_a + (2\hat{J} - 1)\delta_\chi\right)\hat{J}_z + \chi\hat{J}_z^2,\end{aligned} \tag{2.21}$$

where $\delta_\chi = (\chi_{bb} - \chi_{aa})/2$ is given by the difference of the intraspecies scattering lengths, and $\chi = (\chi_{bb} + \chi_{aa} - 2\chi_{ab})/2$ is determined by the difference between intra- and interspecies interactions. The first two terms of Eq. 2.21 are constant and thus can be neglected. Defining a mean-field detuning $\delta_M = \tilde{\omega}_b - \tilde{\omega}_a + (2\hat{J} - 1)\delta_\chi$, the Hamiltonian reduces to

$$\mathcal{H}_{\mathrm{OAT}} = \delta_M \hat{J}_z + \chi\hat{J}_z^2, \tag{2.22}$$

which is known as the one-axis twisting Hamiltonian [25]. Here, the $\hat{J}_z^2$ term leads to a redistribution of the uncertainty of a quantum state, which can be employed for creating spin squeezed states in two-component Bose-Einstein condensates.

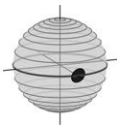

## 2.3. Rabi Coupling and the Lipkin-Meshkov-Glick Hamiltonian

The dynamics of this two-component system can be strongly modified by adding linear interconversion of the two species. In second quantization, linear coupling can be captured by the Hamiltonian

$$\mathcal{H}_{\text{cpl}} = -\frac{\hbar\Omega_r}{2}\int d^3\mathbf{x}\,\left(\hat{\psi}_a(\mathbf{x})\hat{\psi}_b^\dagger(\mathbf{x})\mathrm{e}^{-\mathrm{i}(\delta_c t+\varphi_0)} + \text{h.c.}\right), \tag{2.23}$$

where $\Omega_r$ denotes the Rabi frequency, i.e. the coupling strength, $\delta_c$ is the detuning of the coupling frequency relative to the atomic transition, and $\varphi_0$ denotes the phase between coupling and the atomic transition dipole. Analogous to section 2.1, in the two-mode approximation this simplifies to

$$\mathcal{H}_{\text{cpl}} = -\frac{\hbar\tilde{\Omega}}{2}\left(\hat{a}_a\hat{a}_b^\dagger\mathrm{e}^{-\mathrm{i}(\delta_c t+\varphi_0)} + \text{h.c.}\right) \tag{2.24}$$

with $\tilde{\Omega} = \Omega_r\int d^3\mathbf{x}\,\phi_a(\mathbf{x})\phi_b(\mathbf{x})$, which is equivalent to $\Omega_r$ for perfectly overlapping clouds. In the pseudospin representation, after transformation to the Schrödinger picture, this can be expressed as

$$\mathcal{H}_{\text{cpl}} = -\frac{\hbar\tilde{\Omega}}{2}\left(\cos(\varphi_0)\hat{J}_x + \sin(\varphi_0)\hat{J}_y\right) + \frac{\hbar\delta_c}{2}\hat{J}_z. \tag{2.25}$$

Assuming $\phi_a = \phi_b$ and $\varphi_0 = 0$, we can express an interacting two-component BEC with additional coupling using the Hamiltonians 2.22 and 2.25

$$\mathcal{H}_{\text{LMG}} = \chi\hat{J}_z^2 - \Omega\hat{J}_x + \delta\hat{J}_z, \tag{2.26}$$

where $\Omega = \frac{\hbar\tilde{\Omega}}{2}$ and $\delta = \frac{\hbar}{2}(\delta_M + \delta_c)$. This is a special case of the well-known Lipkin-Meshkov-Glick Hamiltonian [67], which has been intensely studied in the context of nuclear physics and can be used to describe the quantum dynamics of a Bosonic Josephson Junction.
Depending on the choice of the parameters $\chi, \Omega$ and $\delta$, the dynamics governing the system drastically change, ranging from Rabi oscillations to nonlinear self-trapping [66, 68, 69, 70]. This can be nicely understood from the corresponding classical mean field Hamiltonian, which will be discussed in section 2.6.

## 2.4. Generalized Bloch Sphere and Husimi Q Representation

### Coherent spin states

In the pseudospin picture, a single particle with two levels $|a\rangle$ and $|b\rangle$ can be described as a spin with length $J = 1/2$. In this representation, state $|a\rangle$ corresponds to the eigenstate of $\hat{J}_z$ with $j_z = -1/2$ and $|b\rangle$ to $j_z = +1/2$. Every pure state of such a system can be written in the form $|\theta,\phi\rangle = \sin(\theta/2)|a\rangle + \cos(\theta/2)\mathrm{e}^{\mathrm{i}\varphi}|b\rangle$ and displayed on a Bloch sphere (see Fig. 2.1). Here, the coordinates are chosen such that the pseudospin operators coincide

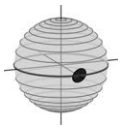

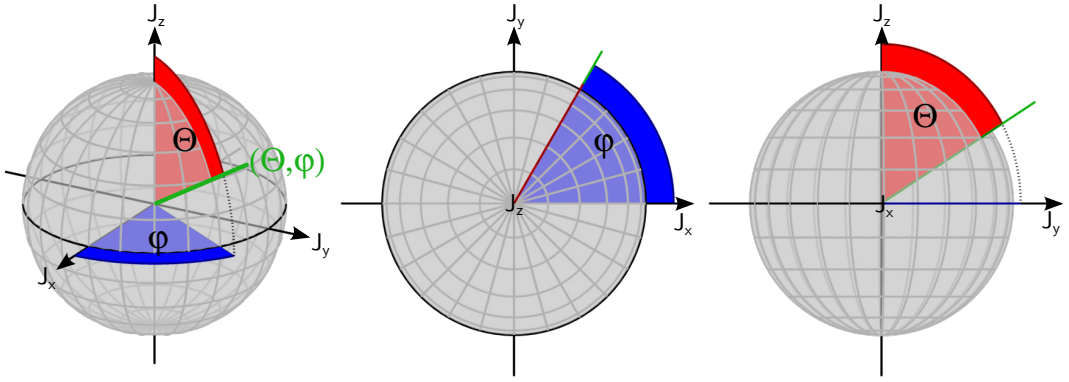


Figure 2.1.: **Bloch sphere representation of spin-1/2 system.** Any pure state of a single particle in a two-level system can be written in the form $|\theta,\phi\rangle = \sin(\theta/2)|a\rangle + \cos(\theta/2)\mathrm{e}^{\mathrm{i}\varphi}|b\rangle$ and displayed on a Bloch sphere (left panel). The relative phase is given by the azimuthal angle $\varphi$ (middle), whereas the polar angle $\theta$ (right panel) is related to the population difference of the two levels.

with the definitions given in Eq. 2.10-2.12. This means that the $z$ direction of the spin is proportional to the population difference, $|b\rangle\langle b| - |a\rangle\langle a|$, which is described by the polar angle $\theta$, and the phase $\phi$ is determined by the coherences $\hat{J}_x$ and $\hat{J}_y$.
A general pure state of $N$ particles can be written as the tensor product of all $N$ single particle states [71]

$$|\Psi\rangle = \prod_{n=1}^{N} |\theta_n,\phi_n\rangle = \prod_{n=1}^{N} \sin(\theta_n/2)|a\rangle + \cos(\theta_n/2)\mathrm{e}^{\mathrm{i}\varphi_n}|b\rangle. \tag{2.27}$$

Assuming exchange symmetry between all particles, which is the case for our system of indistinguishable particles, restricts this general $2^N$ dimensional Hilbert space to the subspace of dimension $N+1$, for which the spin length is given by $J = N/2$.
A natural basis in this subspace are the Dicke states [72], which are the eigenstates of both $\hat{J}^2$ and $\hat{J}_z$. They can be labeled as $|J,M\rangle$, where $J = N/2$ is the spin length and $M$ denotes the $\hat{J}_z$ projection of the state. However, these number states are not the natural states of uncorrelated particles in this system and can be highly entangled. Only the two extremal Dicke states $|J,-J\rangle$ and $|J,+J\rangle$, corresponding to all particles in one of the components, naturally occur, and the generation of all other Dicke states requires elaborate experimental methods [24, 51].
The collective state for $N$ uncorrelated particles which are all occupying the single-particle state $|\theta,\phi\rangle$ in the symmetric subspace is given by

$$|N,\theta,\phi\rangle = |\theta,\phi\rangle^{\otimes N}. \tag{2.28}$$

These states are analogous to coherent states of a radiation field and thus are referred to as *atomic coherent states* [71] or *coherent spin states* (CSS) [73]. They can be obtained by rotating an initial extremal Dicke state $|J,+J\rangle$ through an angle $(\theta,\phi)$ in the angular momentum



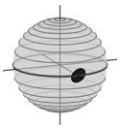

space, yielding

$$|N,\theta,\phi\rangle = R_{\theta,\phi}|J,+J\rangle. \tag{2.29}$$

Such a rotation can be written as $R_{\theta,\phi} = \mathrm{e}^{-\mathrm{i}\theta(J_x\sin(\phi)-J_y\cos(\phi))}$ and can be realized through Rabi coupling as in Eq. 2.25. This allows to obtain the expansion of the coherent spin states in terms of the Dicke state basis, yielding [71, 74]

$$|N,\theta,\phi\rangle = \sum_{M=-J}^{J} \binom{2J}{M+J}^{1/2} \sin\left(\frac{\theta}{2}\right)^{J+M} \cos\left(\frac{\theta}{2}\right)^{J-M} \mathrm{e}^{-\mathrm{i}(J+M)\varphi}|J,m\rangle. \tag{2.30}$$

Note that the amplitudes in the Dicke state basis are given by a binomial distribution. This can be intuitively grasped as being a statistical distribution of $N$ independent particles in a superposition between the two single-particle states (see section 4.1.1). It also means that the coherent spin states become more localized for larger particle number.
Coherent spin states are non-orthogonal and their overlap is given by [71]

$$\langle\tilde{\theta},\tilde{\phi}|\theta,\phi\rangle = \mathrm{e}^{\mathrm{i}J(\phi-\tilde{\phi})}\left[\cos\left(\frac{\theta-\tilde{\theta}}{2}\right)\cos\left(\frac{\phi-\tilde{\phi}}{2}\right) - \mathrm{i}\cos\left(\frac{\theta+\tilde{\theta}}{2}\right)\sin\left(\frac{\phi-\tilde{\phi}}{2}\right)\right]^{2J}. \tag{2.31}$$

### Husimi Q representation

In the case of a single particle, the system is fully described by the two variables $(\theta,\phi)$ and can thus be displayed on the Bloch sphere without any additional assumptions. This is not the case for the collective states of $N$ particles in a $N+1$ dimensional Hilbert space, where an exact mapping of the state onto a sphere is not possible. However, many properties of such states can be grasped from the projection of the collective state onto the coherent states of the system.
The coherent spin states $|N,\theta,\phi\rangle$ form a complete basis for the symmetric $N+1$ dimensional Hilbert space, and represent the most localized non-entangled collective states in a given direction $(\theta,\phi)$. A general state in this Hilbert space, described by a density matrix $\rho$, can thus be conveniently visualized by calculating its diagonal elements in the coherent state representation [75]

$$Q(\theta,\phi) = \frac{2J+1}{4\pi}\langle\theta,\phi|\rho|\theta,\phi\rangle. \tag{2.32}$$

This probability distribution corresponds to the normalized Husimi Q representation and can be displayed on a generalized Bloch sphere. As in the single particle case, the $z$ projection is proportional to the population imbalance of the two components. The poles of the sphere denote the collective states $|a\rangle^{\otimes N}$ and $|b\rangle^{\otimes N}$ with all atoms in one of the internal states. Note that due to the convolution with the CSS, the extension of arbitrary states in the Husimi representation will always be larger than the employed coherent states.
As the CSS are non-orthogonal (see Eq. 2.31), the Husimi Q distribution of an arbitrary coherent spin state is non-zero in a specific angular range and spreads over a finite region, as shown in Figure 2.2.

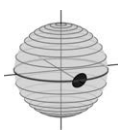

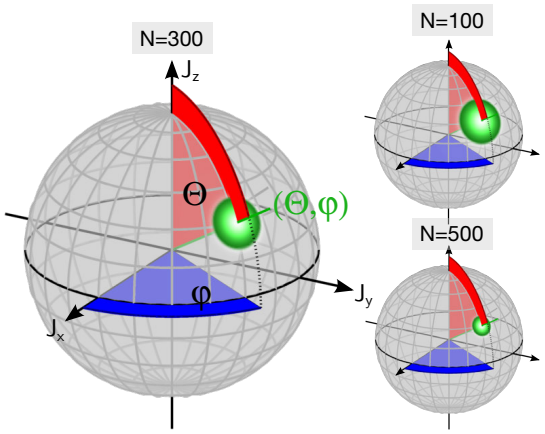


Figure 2.2.: **Husimi distribution of coherent spin states on a generalized Bloch sphere.** The collective states of N particles can be conveniently visualized via the Husimi distribution on a generalized Bloch sphere, which measures the overlap of a general state with the coherent spin states of the system. The $z$ projection of the sphere is proportional to the population difference – the north pole is equivalent to the collective state $|b\rangle^{\otimes N}$, and the lower pole to $|a\rangle^{\otimes N}$. The left panel shows the coherent state $|N = 300, \theta = \pi/3, \phi = \pi/3\rangle$. The coherent states become more localized for increasing atom number. This is demonstrated by the Husimi distributions for the coherent states $|100, \pi/3, \pi/3\rangle$ and $|500, \pi/3, \pi/3\rangle$ in the right panel.

## 2.5. Quantum Uncertainties and Spin Squeezing

The non-vanishing commutator of the pseudospin operators $[\hat{J}_i, \hat{J}_j] = \mathrm{i}\epsilon_{ijk}\hat{J}_k$ leads to a Heisenberg uncertainty relation given by

$$\mathrm{Var}(\hat{J}_i)\mathrm{Var}(\hat{J}_j) \geq \frac{1}{4}|\epsilon_{ijk}|\langle \hat{J}_k\rangle^2, \tag{2.33}$$

where the variances are given by $\mathrm{Var}(\hat{J}_i) = \langle \hat{J}_i^2\rangle - \langle \hat{J}_i\rangle^2$.
For a single particle, i.e. $J = 1/2$, in state $|\theta, \phi\rangle$, this leads to a Heisenberg uncertainty product of $\mathrm{Var}(\hat{J}_{\mathbf{n_1}})\mathrm{Var}(\hat{J}_{\mathbf{n_2}}) = \frac{1}{4}\cdot\frac{1}{4}$ for the components $n_1$ and $n_2$ orthogonal to the mean spin direction. This means that these components have the maximum possible uncertainty, corresponding to a variance of $\frac{1}{4}$.
The coherent spin states described above are collective states of $N$ uncorrelated particles. Thus, the corresponding variances for the collective state are simply given by the sum of the single particle variances

$$\mathrm{Var}(\hat{J}_{\mathbf{n_1}}) = \mathrm{Var}(\hat{J}_{\mathbf{n_2}}) = \frac{N}{4} = \frac{J}{2}. \tag{2.34}$$

This means that coherent spin states have isotropic uncertainties and reach the minimal uncertainty product allowed by the Heisenberg uncertainty relation.

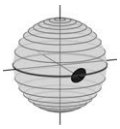

The presence of quantum mechanical correlations between the particles allows to redistribute uncertainties by partly canceling the fluctuations along one direction at the expense of increased uncertainty in orthogonal direction [25]. This concept is called *spin squeezing*. A state is squeezed if the variance along a certain direction orthogonal to its mean spin vector is reduced below $N/4$. Such states can be generated by introducing correlations via nonlinear spin-spin interactions [25, 76], quantum non-demolition measurements [32] or interaction of the atoms with squeezed light fields [30, 31].

Spin squeezing requires quantum correlations between the particles. Thus, as shown by *Sørensen et al.* [44], it can be employed as an entanglement witness. Specifically, this can be quantified in terms of the spin squeezing parameter

$$\xi_{\mathrm{S}}^2 = \frac{N\mathrm{Var}(\hat{J}_{\mathbf{n_1}})}{\langle \hat{J}_{\mathbf{n_2}} \rangle^2 + \langle \hat{J}_{\mathbf{n_3}} \rangle^2}, \tag{2.35}$$

where $\hat{J}_{\mathbf{n_i}}$ denotes three mutually orthogonal spin components. If the spin squeezing inequality

$$\xi_{\mathrm{S}}^2 < 1 \tag{2.36}$$

is fulfilled, this means that the state of the atoms is entangled. Furthermore, the *depth of entanglement* of the many-particle state can be detected by measuring the variance in one spin direction and the coherence of the system, i.e. the mean spin length of the state [77]. The depth of entanglement denotes the minimum number of particles that are entangled, which means that the density matrix of the full ensemble cannot be decomposed into products of density matrices which are smaller than this number. Both quantities that are required for this criterion can be straight-forwardly detected in the experiment. This has enabled the identification of multiparticle entanglement of up to 170 particles in experimentally generated squeezed states [45, 46, 47]. Note that the spin squeezing inequality is a sufficient, but not a necessary criterion for entanglement, and states can be entangled but not squeezed.
A detailed description of how spin squeezed states in Bose-Einstein condensates can be experimentally generated and characterized will be given in Chapter 4.

## 2.6. Mean Field Hamiltonian: The Classical Description

As depicted in Fig. 2.2, the coherent spin states $|N, \theta, \phi\rangle$ become more and more localized for larger atom numbers. For $N \to \infty$, the spin can be treated as a classical quantity, and the operators are replaced by c-numbers [78], i.e.

$$\hat{J} \to \frac{N}{2} \left(\sin\theta\cos\phi, \sin\theta\sin\phi, \cos\theta\right). \tag{2.37}$$

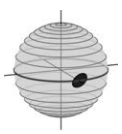

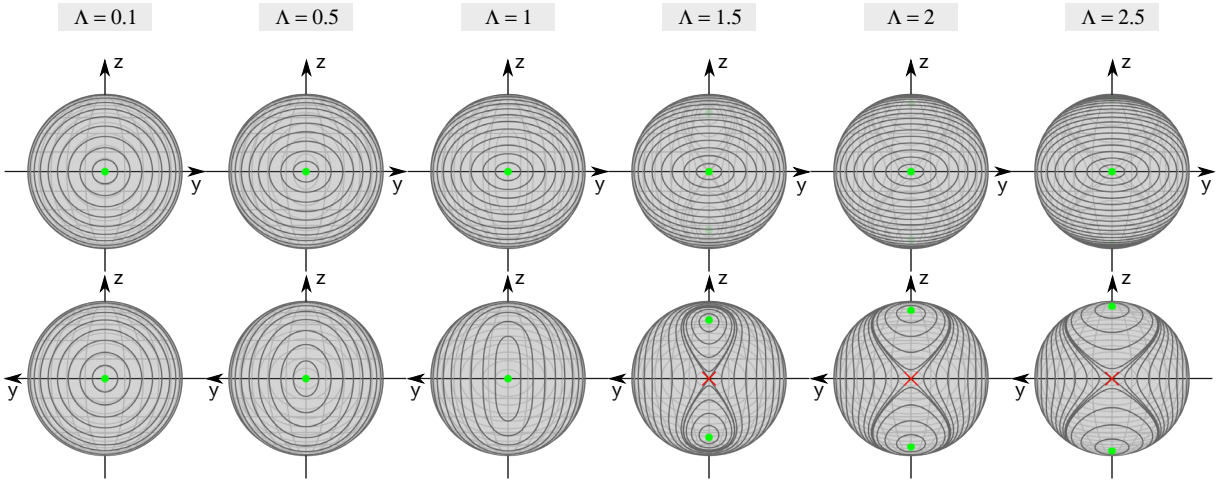


Figure 2.3.: **Classical phase space of the resonant Lipkin-Meshkov-Glick Hamiltonian for different values of Λ.** Depending on the choice of $\Lambda$, the topology of the classical phase space, governed by the Hamiltonian Eq. 2.41, strongly changes. The upper row shows the classical phase space on the region of the sphere around $\phi = 0$ for the resonant case ($\tilde{\delta} = 0$), in which the dynamics only depend on $\Lambda$. Larger interactions, corresponding to larger $\Lambda$, lead to stronger deformation of the *plasma oscillations*. The lower panel depicts the other side of the sphere ($\phi = \pi$). Here, at $\Lambda = 1$, the formerly stable (as marked with a green dot) fixed point $F_\pi$ becomes unstable (red cross), and two new stable fixed points $F_+$ and $F_-$ appear above and below $F_\pi$. The trajectories around these fixed points are separated from the plasma oscillations by an eight-shaped separatrix, which passes through the unstable fixed point. For even stronger interaction ($\Lambda > 2$), the separatrix encloses the poles. Note that in our experiment, the situation during the strong coupling pulses corresponds to $\Lambda = 0.1$, where the deviations from regular Rabi oscillations are still small. For the experiments that demonstrate the generation of spin squeezing in the bifurcated scenario, $\Lambda \approx 1.5$ is employed.

This implies that the expectation values of the product of operators factorize. In this description, the polar angle $\theta$ is determined by the expectation value of $\hat{J}_z$ by $\theta = \arccos\left(\frac{2\langle \hat{J}_z \rangle}{N}\right)$, and the phase is given from the expectation values of the coherences $\phi = \arctan\left(\frac{\langle \hat{J}_y \rangle}{\langle \hat{J}_x \rangle}\right)$.
Replacing the operators in the Hamiltonian by the classical expectation values allows us to obtain insights into the underlying classical phase space and the corresponding dynamics.
Specifically, for the one-axis twisting Hamiltonian (Eq. 2.22), we find the classical mean-field Hamiltonian

$$\mathcal{H}_{\text{MF\_OAT}} = \frac{N^2\chi}{4} z^2 + \frac{N\delta}{2} z, \tag{2.38}$$

using $z = \cos\theta$.

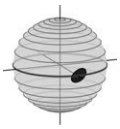

The corresponding equations of motion obtained from $\dot{z}(t) = -\frac{\partial \mathcal{H}}{\partial \phi}$ and $\dot{\phi}(t) = \frac{\partial \mathcal{H}}{\partial z}$ are given by

$$\dot{z}(t) = 0 \quad \text{and} \tag{2.39}$$

$$\dot{\phi}(t) = \frac{N^2\chi}{2} z + \frac{N\delta}{2}. \tag{2.40}$$

Thus, the dynamics of the one-axis twisting Hamiltonian does not alter the population imbalance and solely leads to an imbalance-dependent phase evolution. This causes a redistribution of quantum uncertainty and results in spin squeezing of initially isotropic quantum states.

The situation is much more complex for the Lipkin-Meshkov-Glick Hamiltonian (Eq. 2.26). Here, replacing the operators with the classical expectation values leads to a mean-field Hamiltonian reading

$$\mathcal{H}_{\text{MF\_LMG}} = \frac{N\Omega}{2}\left(\frac{\Lambda}{2} z^2 - \sqrt{1-z^2}\cos\phi + \tilde{\delta} z\right), \tag{2.41}$$

where the system parameters have been absorbed as $\Lambda = \chi N/\Omega$, and $\tilde{\delta} = \delta/\Omega$. The corresponding canonical equations of motion yield

$$\dot{z}(t) = -\frac{N\Omega}{2}\sqrt{1-z^2(t)}\sin\phi(t), \tag{2.42}$$

$$\dot{\phi}(t) = \frac{N\Omega}{2}\left(\Lambda z + \frac{z}{\sqrt{1-z^2}}\cos\phi + \tilde{\delta}\right). \tag{2.43}$$

These equations of motion can be solved numerically or analytically in terms of Jacobian and Weierstrassian elliptic functions [69]. The corresponding trajectories for a set of initial conditions reveal the underlying topology of the mean field Hamiltonian, which strongly depends on the choice of the parameters $\Lambda$ and $\tilde{\delta}$.

Let us for simplicity consider the resonant case first, i.e. $\tilde{\delta} = 0$. Interestingly, in this case the Hamiltonian 2.41 is equivalent to the description of a non-rigid pendulum with tilt angle $\phi$, angular momentum $z$ and length $\sqrt{1-z^2}$ [69].
The topology of the dynamics for this system solely depends on the parameter $\Lambda = \chi N/\Omega$, which is determined by the relative strength of the nonlinear interaction and the linear interconversion. Fig. 2.3 depicts the dependence of this classical phase space on the parameter $\Lambda$. The timescale of the corresponding dynamics is set by the prefactor $N\Omega/2$, and thus depends on the coupling strength and the atom number.
In the case of dominant Rabi coupling (*Rabi regime*, $\Lambda < 1$), the system features two stable fixed points at $F_0 = (z, \phi) = (0, 0)$ and $F_\pi = (0, \pi)$. The dynamics are given by Rabi oscillations which are deformed in the presence of the nonlinear interaction, called *plasma oscillations* for the trajectories enclosing $F_0$ and $\pi$ *oscillations* for those around $F_\pi$ [69, 70]. These oscillations differ in speed and shape. The oscillation frequency of the plasma oscillations is enhanced and given by

$$\omega_{\text{pl}} = \Omega\sqrt{1+\Lambda} \tag{2.44}$$

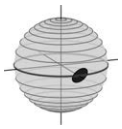

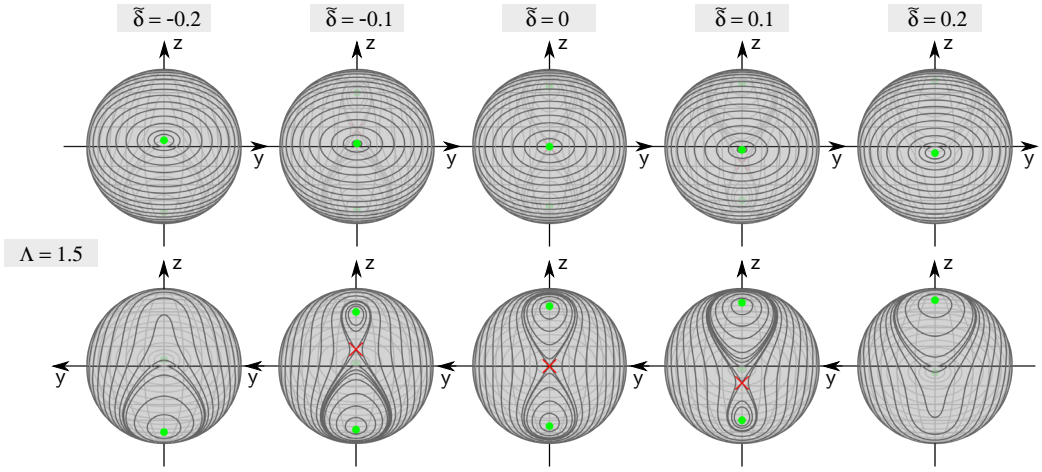


Figure 2.4.: **Classical phase space for various $\tilde{\delta}$ and $\Lambda = 1.5$.** The classical phase space of the system is strongly altered by the presence of a finite detuning $\tilde{\delta}$. For the plasma oscillations, this induces a tilt of the rotation axis, corresponding to a shift of the stable fixed point (upper panel). On the $\pi$ side of the sphere, the bifurcated scenario with one unstable and two stable fixed points is only recovered for weak detunings. In the case of a large detuning, one of the stable fixed points $F_{+/-}$ and the unstable fixed point $F_\pi$ vanish, and only one stable fixed point remains.

for small amplitudes, whereas the $\pi$ oscillation frequency is given by

$$\omega_\pi = \Omega\sqrt{1-\Lambda}. \tag{2.45}$$

This can be understood from the fact that on the $\pi$ side of the sphere, the rotation of the coupling and the nonlinear interaction counteract, whereas they enhance each other on the other side. Both kinds of oscillations have been observed in the experiment [79, 80, 70].

The dynamics of this system drastically changes for $\Lambda > 1$. This situation is called the *Josephson regime*, as the dynamical effects occurring in this situation are similar to the Josephson effect in weakly linked superconductors. In this regime, the formerly stable fixed point $F_\pi$ becomes unstable, and two additional stable fixed points $F_+ = (+\sqrt{1-1/\Lambda^2}, \pi)$ and $F_- = (-\sqrt{1-1/\Lambda^2}, \pi)$ appear on the $\pi$ side of the sphere (see lower panel of Fig. 2.3). In this bifurcated system, the trajectories around $F_+$ and $F_-$ have, in contrast to those around $F_0$ and $F_\pi$, a non-vanishing expectation value of $z$. This situation is referred to as *macroscopic self-trapping* [69, 70]. The corresponding trajectories are separated from the plasma oscillations by an eight-shaped *separatrix*, which is centered at the unstable fixed point $F_\pi$. With further increasing $\Lambda$, the stable fixed points move towards the poles, and for $\Lambda > 2$, the separatrix encloses the poles.
The topology of the phase space becomes more complex by the addition of a finite detuning $\tilde{\delta}$. Depending on the relative size of $\Lambda$ and $\tilde{\delta}$, the corresponding phase space distinctly



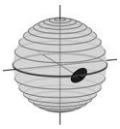

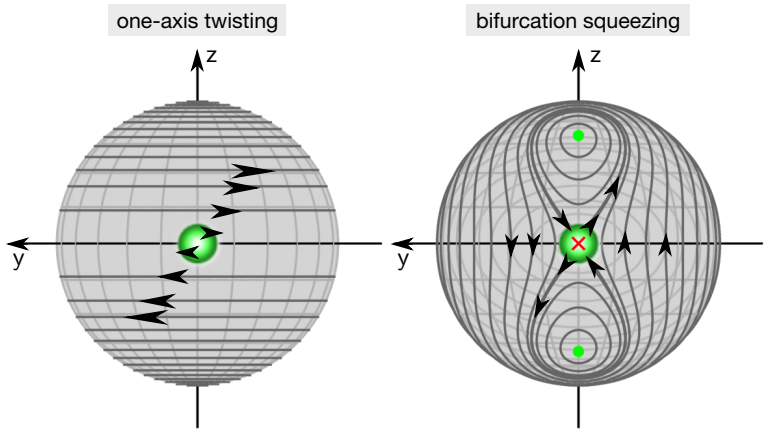


Figure 2.5.: **Squeezing generation and classical trajectories.** The generation of squeezing can also be intuitively understood from the mean field trajectories. In the one-axis twisting case (left), the equations of motion (Eq. 2.39) show that the phase evolution $\dot{\phi} \propto z$. An initial coherent state of N particles spreads over a region of size $1/\sqrt{N}$ in $z$ direction, and thus gets deformed by the $z$ dependent phase evolution. In the Lipkin-Meshkov-Glick model, squeezing can be generated on the unstable fixed point in the bifurcated regime (right panel). Here, the classical trajectories lead to a compression of the state along one direction of the separatrix, and elongation along the other axis, as indicated by the black arrows.

changes. This is demonstrated in Fig. 2.4, which depicts the classical phase space for $\Lambda = 1.5$ and various detunings $\tilde{\delta}$. In the case of strong detuning, one of the stable fixed points $F_{+/-}$ and the unstable fixed point vanish. The bifurcated situation is recovered only for relatively small detunings. Note the strong sensitivity on small parameter changes: For our typical experimental parameters of $N\chi = 2\pi \times 30\,\mathrm{Hz}$, the depicted situation is given for a coupling strength of $\Omega = 2\pi \times 20\,\mathrm{Hz}$. Thus, the corresponding detunings in Fig. 2.4 are as small as $\delta = 2\pi \times [-4,\, -2,\, 0,\, +2,\, +4]\,\mathrm{Hz}$. A detailed description of the mean field dynamics of this system can be found in [81].

### Squeezing generation in the bifurcated regime

A state that evolves under the one-axis twisting Hamiltonian is squeezed by the redistribution of the finite quantum uncertainty along the $z$ direction caused by the $\hat{J}_z^2$ term, as described above (Fig. 2.5).
The instability in the bifurcated regime can also be employed to generate squeezing [82]. This can be intuitively understood from the trajectories of the classical phase space. In the bifurcated regime, the fixed point $F_\pi$ is a saddle point in the potential landscape. An initial isotropic coherent spin state which is prepared onto this unstable fixed point is compressed along one direction and elongated due to rapid spreading along the other axis of the separatrix (see right

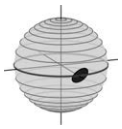

panel of Fig. 2.5). This process is expected to generate squeezing on faster timescales compared to the one-axis twisting scenario. For longer evolution times, the generation of highly entangled non-Gaussian states is expected [78]. In this thesis, we will study the short-time dynamics and the associated generation of squeezed states. The long-time dynamics and the corresponding entangled states are beyond the scope of this thesis and described elsewhere [61].



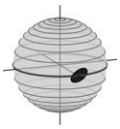

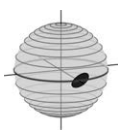

# 3. The Experiment: Generation, Characterization and Detection of the Condensates

Having introduced the basic theoretical concepts in the previous chapter, we will now discuss the system which we employ for experimentally realizing these Hamiltonians. We will shortly present the experimental setup that generates an array of $^{87}$Rb Bose-Einstein condensates, and show how Rabi coupling and nonlinearity are implemented in our experiment. Afterwards, we will characterize some important properties of our condensates, such as the strength of different atomic loss channels and atom number dependences of the experimental parameters. In the last section of this chapter, we will describe the absorption imaging procedure which is employed for state-selective detection of the particle numbers in the condensates.

## 3.1. An Array of Bose-Einstein Condensates of $^{87}$Rb

The atomic resource for the measurements presented in this thesis consists of an array of around 30 independent Bose-Einstein condensates, which is generated by a shallow dipole trap with a superimposed optical lattice potential. In the following, we we will shortly review the current state of the setup. A more detailed description of the experimental system can be found elsewhere [83].

To attain our ultracold atomic cloud, we start with laser-cooled $^{87}$Rb atoms in a 3D magneto-optical trap (MOT) that is loaded out of a cold atomic beam from a 2D MOT. The trapped atoms are subsequently exposed to sub-Doppler cooling during a short period in an optical molasses, optically pumped into the $F = 1$ manifold of the ground state and loaded into a magnetic trap with time-orbiting potential (TOP) [84]. In the TOP trap, evaporative circle-of-death cooling further lowers the temperature to slightly above $T_c$, the critical temperature for Bose-Einstein condensation. Our evaporation scheme yields around $10^6$ atoms close to $T_c$ after 25 s of evaporative cooling. This cold cloud is subsequently loaded into a crossed dipole trap created from a single 1030 nm commercial diode pumped solid state laser source (Innolight Corona IR). A second stage of evaporation is performed in the optical trap by lowering the intensity of one of the trapping beams, yielding a pure BEC with up to $10^5$ atoms. For the spinor physics discussed in this thesis, further evaporation reduces the particle number down to approximately $10^4$ atoms.

After these evaporation ramps, one of the dipole trap beams is slowly switched off, and the condensate is allowed to expand within the shallow potential of the remaining trapping beam, which has a large aspect ratio of $\approx 50$. Subsequently, a 1D lattice potential is ramped up

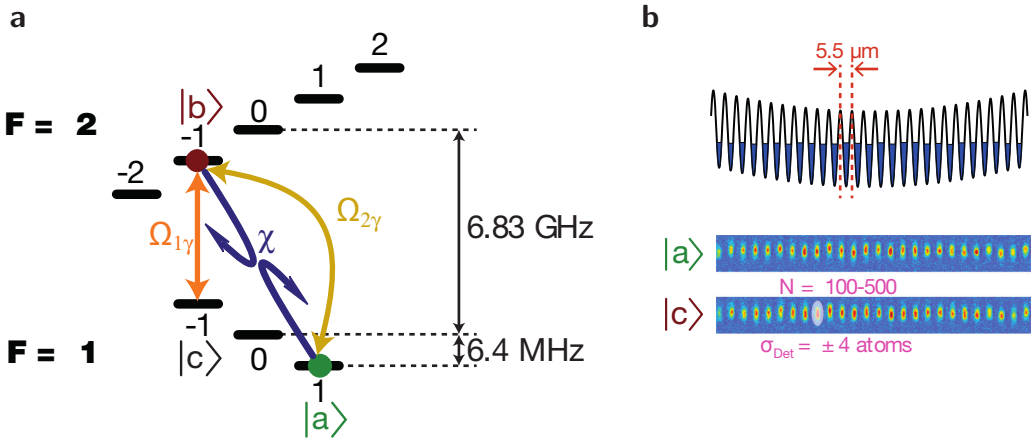


Figure 3.1.: **Level scheme of $^{87}$Rubidium at 9.1 G and trapping geometry** a) We condense the atomic clouds in a single hyperfine state $|c\rangle = |F = 1, m_F = -1\rangle$ of the electronic ground state. Subsequently, a rapid adiabatic passage transfers all atoms to $|a\rangle = |1, +1\rangle$. A Feshbach resonance at 9.1 G is employed to tune the nonlinearity $\chi$ between the levels $|a\rangle$ and $|b\rangle = |2, -1\rangle$. Coupling between those levels is implemented via combined radio frequency and microwave radiation with the resonant two-photon Rabi frequency $\Omega_{2\gamma} = 2\pi \times 310\,\text{Hz}$. One-photon coupling between $|b\rangle$ and $|c\rangle$ with a Rabi frequency of $\Omega_{1\gamma} = 2\pi \times 7\,\text{kHz}$ can be applied using microwave radiation. b) The initial condensate is split into up to 30 independent condensates using a 1D lattice with $5.5\,\mu\text{m}$ spacing. Each lattice site contains several hundred atoms. State selective imaging allows detecting all hyperfine components with an atom number resolution of $\sigma_{\text{Det}} = \pm 4$.

to create around 30 independent condensates, each containing several hundred atoms. This standing wave potential is created by the interference of two laser beams which are obtained from the same source, a *Coherent 899* Ti:Sapphire laser running at 820 nm wavelength. They are crossed under a small angle such that the lattice spacing is 5.5 µm. The intensity of the lattice beams is chosen high enough such that tunneling is negligible on the experimental timescales, yielding 30 independent condensates.

The resulting trap frequencies for the single lattice sites are 130 Hz in radial and 660 Hz in lattice direction, leading to condensate wave functions that are slightly smaller than the spin healing length of the condensate. Thus, each of the condensates in the individual lattice sites can be considered to be in a single spatial mode, and interplay between external and internal dynamics is negligible.

During the cooling procedure, a homogeneous magnetic bias field is ramped to 9.12 G, which is in the vicinity of an interspecies Feshbach resonance of $^{87}$Rb [85, 86] (see section 3.2). All condensed atoms are initially prepared in the magnetically trappable state $|c\rangle = |F = 1, m_F = -1\rangle$. After the cooling scheme, a rapid adiabatic passage transfers these atoms to the state $|a\rangle = |1, +1\rangle$, which is the starting point for further experiments. The pulse sequences for the spinor experiments are implemented via resonant microwave and radio frequency (RF)

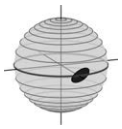

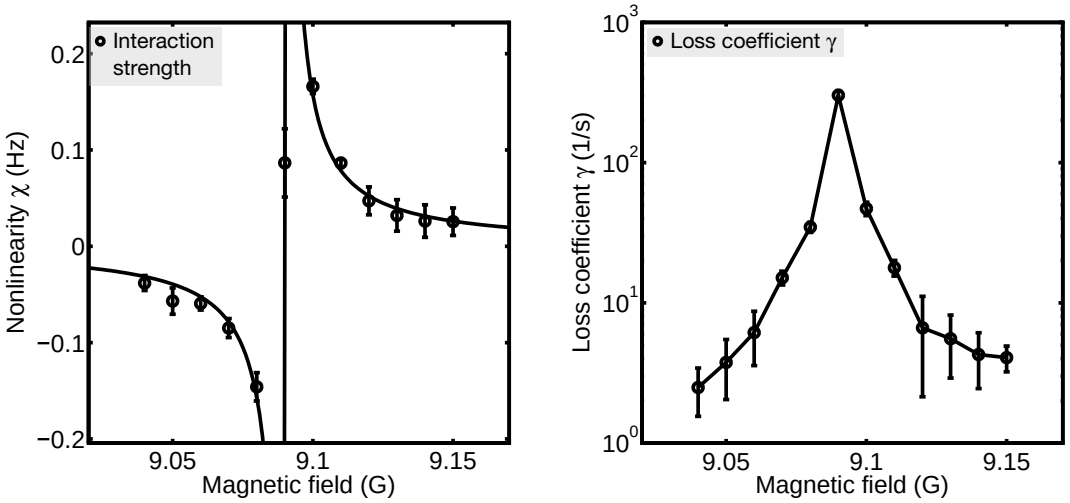


Figure 3.2.: **Interspecies Feshbach resonance of $^{87}$Rb at 9.09 G.** A Feshbach resonance between the levels $|a\rangle$ and $|b\rangle$ allows to tune the interspecies scattering length $a_{ab}$ by changing the magnetic offset field, and thus makes a significant nonlinear interaction strength $\chi$ attainable in our system. The left panel shows the measured values of $\chi$ obtained from plasma and $\pi$ oscillations (Eq. 3.1). The solid line is a fit of type $f = \delta B/(B - B_0)$, indicating the typical shape of a Feshbach resonance. For the choice of the working field, also the enhanced loss rate close to the Feshbach resonance has to be considered (right panel). In our experiments, we choose $B = 9.12\,\mathrm{G}$, which combines significantly increased nonlinear interaction with modest loss rates. Unless stated otherwise, all error bars in this thesis denote statistical 1.s.d. intervals.

radiation, as described in section 3.3. After these pulse sequences, the atoms are detected via state-selective absorption imaging, which will be explained in more detail in section 3.6.

## 3.2. Feshbach Resonance for Nonlinearity Tuning

Our spinor experiments are carried out in the vicinity of a Feshbach resonance [87, 88] of $^{87}$Rb, which can be used to tune the interspecies scattering length between the levels $|a\rangle$ and $|b\rangle = |2, -1\rangle$ by changing the magnetic bias field. The background scattering lengths of $^{87}$Rb are almost equal between all hyperfine components. Consequently, in our system a change of the interspecies scattering length is essential for attaining significant nonlinearities, which are the basic ingredients for the generation of entangled states. The Feshbach resonance employed in our experiment is centered at a magnetic field of $B_0 = 9.09\,\mathrm{G}$ [85, 86], and has a width of 1.6(2) mG [89]. In our setup, this bias field is provided by a pair of large Helmholtz coils (edge length 1 m) and actively stabilized by use of a fluxgate magnetometer (Bartington Instruments Mag-03MS1000) near the experimental chamber [90]. This stabilization reduces the shot-to-shot variation of the field down to 30 µG at our working field. Including slow drifts



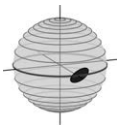

due to the temperature dependence of the fluxgate sensor, we achieve a long-term stability of 45 µG over the course of a several days.
The Feshbach resonance allows tuning the interspecies interaction $a_{ab}$ by around 30% and thus changing the strength of the nonlinearity $\chi$ by a large factor (see Fig. 3.2). Experimentally, we can extract this change from frequency measurements of small amplitude plasma and $\pi$ oscillations. Using Eq. 2.44 and 2.45, we find

$$\chi = \frac{\omega_{\mathrm{pl}}^2 - \omega_\pi^2}{N\sqrt{2(\omega_{\mathrm{pl}}^2 + \omega_\pi^2)}}. \tag{3.1}$$

We experimentally observe strongly increased interaction strength close to the resonance (left panel of Fig. 3.2). For choosing a specific magnetic field as the working point, however, also the increased atom loss close to the Feshbach resonance has to be taken into account (right panel of Fig. 3.2). The strong enhancement of the loss rates close to the resonance makes this regime unsuitable even though the interaction is strongly increased. Far away from the resonance, we observe long lifetimes but only small interaction strengths. For the experiments described in this thesis, we thus choose a field of 9.12 G in the intermediate regime, which offers both enhanced interaction and suitable lifetimes for the generation of entangled states. At this field, we find typical nonlinear interaction strengths of $N\chi = 2\pi \times 30\,\mathrm{Hz}$ for 500 particles (see also section 3.5 for a discussion of the dependence on atom number). This implies that the experimental timescale for the generation of squeezed states is on the order of tens of milliseconds.

## 3.3. Coupling with Radio Frequency and Microwave Radiation

Coupling between the different Zeeman substates is achieved by shining resonant microwave and radio frequency (RF) radiation onto the atoms. In this thesis, two relevant transitions are addressed, for which the implementation of the coupling differs. We will describe the details of those schemes in this section.

### Two-photon coupling between $|a\rangle$ and $|b\rangle$

Coupling between the levels $|a\rangle$ and $|b\rangle$ is implemented by a combined two-photon RF and microwave transition. These are the levels exhibiting the interspecies Feshbach resonance (section 3.2). Resonant two-photon coupling on this transition is achieved by detuning both the microwave and the radio frequency source by $-200\,\mathrm{kHz}$ from the respective single-photon transitions $|1,+1\rangle \leftrightarrow |2,0\rangle$ and $|2,0\rangle \leftrightarrow |2,-1\rangle$. The combined two-photon Rabi frequency is $\Omega_{2\gamma} \approx 310\,\mathrm{Hz}$. It is measured using Rabi flopping, i.e. changing the length of the coupling pulse at fixed power and performing a sinusoidal fit to the resulting population imbalance of the two levels. Note that this transition is only in second order sensitive to magnetic fields, as

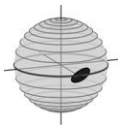

the linear Zeeman shifts of $|a\rangle$ and $|b\rangle$ cancel. A detailed discussion of the magnetic sensitivities can be found in Appendix A.
We can conveniently control the power and phase of the coupling with an arbitrary waveform generator which is used as the radio frequency source. The ability of performing fast and reproducible phase changes of the coupling is an important prerequisite for the generation, manipulation and application of entangled spin states in interferometry.
One important aspect of this two-photon transition is the light shift which is induced by the AC Zeeman effect of the off-resonant coupling radiation. The off-resonant radio frequency and microwave radiation cause shifts of $\Delta f_{\mathrm{RF}} \approx 70\,\mathrm{Hz}$ and $\Delta f_{\mathrm{MW}} \approx 120\,\mathrm{Hz}$, respectively, which are measured using Ramsey spectroscopy. This detuning is compensated by shifting the RF frequency accordingly.
For reaching the bifurcated situation in the Lipkin-Meshkov-Glick Hamiltonian, i.e. $\Lambda = N\chi/\Omega > 1$, the coupling strength has to be smaller than the nonlinearity, which is on the order of $N\chi = 2\pi \times 30\,\mathrm{Hz}$ for our system. Even though such a low coupling strength can in principle also be attained by only reducing the RF power, this is impractical due to the remaining strong light shifts of the full-power microwave radiation. Thus, we attenuate both our microwave source by 10.8 dB by use of a switch in combination with a fixed attenuator, and lower the output power of our RF source by 14 dB. This yields a total attenuation of 24.8 dB and a coupling strength of $\Omega_{\mathrm{att}} \approx 2\pi \times 18\,\mathrm{Hz}$, equivalent to $\Lambda \approx 1.6$. The remaining light shifts during the attenuated coupling are strongly reduced down to 10 Hz for the microwave and 3 Hz for the RF coupling, respectively. Note that switching between full power and attenuated microwave induces an additional phase shift from the attenuator. This shift can be extracted by minimizing the amplitude of resonant plasma and $\pi$ oscillations, and is then compensated with the RF phase.

To attain reproducible conditions for our experiments, we periodically perform automated Ramsey experiments in the presence of off-resonant microwave radiation on this transition. These measurements are used to compensate both small changes in light shift and slow temperature dependent drifts of the fluxgate sensor that is employed for the active stabilization of the magnetic bias field.

### One-photon coupling between $|b\rangle$ and $|c\rangle$

The second relevant coupling transition connects the levels $|b\rangle = |F = 2, m_F = -1\rangle$ and $|c\rangle = |F = 1, m_F = -1\rangle$ via resonant one-photon microwave coupling. This transition is magnetically sensitive as the linear Zeeman shifts of those two levels are in opposite direction, making it susceptible to magnetic field noise. However, the larger one-photon Rabi frequency of 7 kHz ensures good reproducibility even in the presence of small fluctuations of the magnetic bias field.



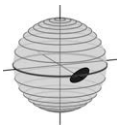

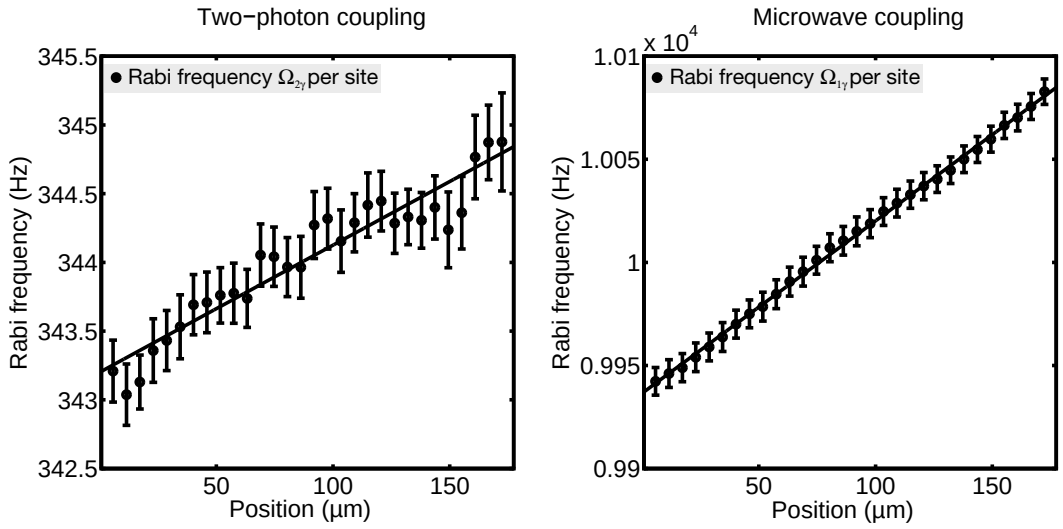


Figure 3.3.: **Gradient of the Rabi coupling strength $\Omega$ over the cloud.** The gradient of the Rabi frequency $\Omega_{2\gamma}$ is minimized by careful alignment of position and orientation of the employed loop antennas, yielding a maximal difference of 0.53% over a spatial range of 165 μm (left panel). In this configuration, the individual gradients of RF and microwave are stronger (1.4% for the microwave contribution, as shown in the right panel), but in opposite direction and thus compensate each other in the case of two-photon coupling.

### Spatial homogeneity of the coupling

The spatial extension of the cloud over more than 100 μm requires the minimization of gradients in the coupling power to ensure homogeneous conditions over all lattice sites. This is achieved by carefully optimizing the position and orientation of the loop antennas employed for irradiating the radio frequency and microwave coupling onto the atoms. For the two-photon coupling, the remaining gradient of $\Omega_{2\gamma}$ over the whole cloud (30 lattice sites, corresponding to 165 μm) is reduced to 0.53% (Fig. 3.3). The underlying gradients of RF and microwave coupling are larger but compensate each other, as can be seen from the remaining microwave gradient of 1.4% on the transition $|1,+1\rangle \leftrightarrow |2,0\rangle$ over the same spatial range in Figure 3.3.

## 3.4. Atom Loss in the Two-Component BEC

There are two major atomic loss processes which are relevant on the timescales of our experiments. Spin relaxation loss removes two particles from the excited state $|b\rangle$ and is unavoidable as it occurs even far away from the Feshbach resonance. The second relevant loss mechanism is enhanced inelastic loss close to the interspecies Feshbach resonance. Losses caused by background collisions and scattering of photons from the dipole trap light are on the time scale of 15 s and thus not relevant for our experiments.

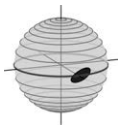

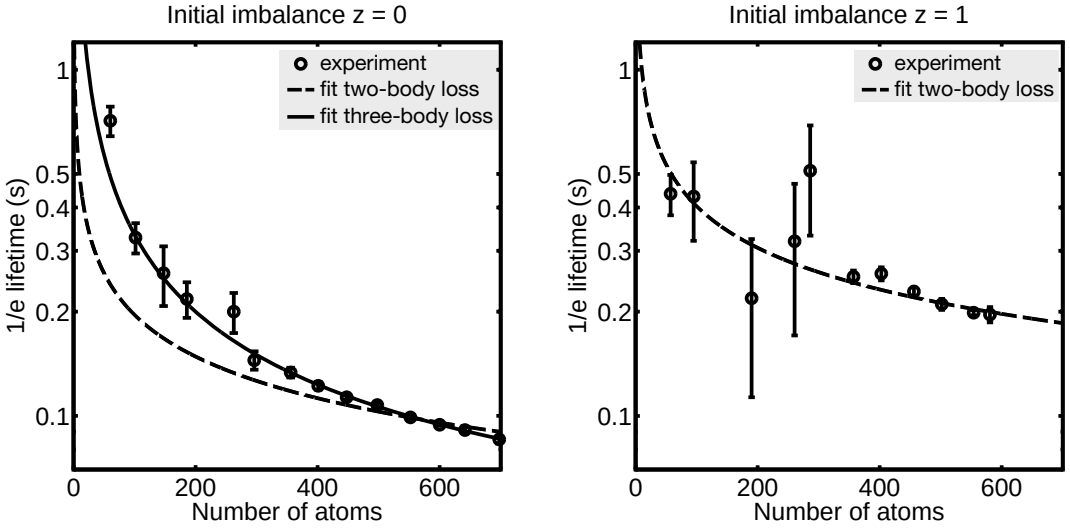


Figure 3.4.: **1/e lifetime $\tau$ versus initial atom number $N_0$ for different population imbalances.** The atomic loss rates at 9.12 G are strongly enhanced due to the close vicinity of the Feshbach resonance. For an equal superposition of the two components ($z = 0$), we find a strong dependence of $\tau$ (obtained from an exponential fit) on the initial atom number $N_0$ (left panel). This is well described by the functional dependence $\tau \propto N_0^{-4/5}$ expected for three-body loss (solid line), whereas a fit of $\tau \propto N_0^{-2/5}$, which would be expected for two-body processes, does not yield good agreement with the experimental data (dashed line). This points at three-body loss as the dominant process close to the Feshbach resonance. For 500 atoms, we find $\tau_{z=0} = 107(2)$ ms. Spin relaxation loss of the excited state $|b\rangle = |F = 2, m_F = -1\rangle$, which is also present far away from the Feshbach resonance, can be independently characterized by preparing a pure sample of all atoms in $|b\rangle$ (right panel). A fit of the atom number dependence with $\tau \propto N_0^{-2/5}$ yields good agreement (dashed line). For this loss process, we find $\tau_{z=1} = 210(8)$ ms for 500 atoms.

### Spin relaxation loss

Spin relaxation loss is caused by spin-changing collisions of two atoms in the excited state $|b\rangle = |F = 2, m_F = -1\rangle$. As the hyperfine quantum number $F$ is not a conserved quantity, one of the atoms can relax to the $F = 1$ hyperfine manifold during the collision [91, 92]. The energy difference between the hyperfine states of 6.8 GHz is much larger than the trap depth, which is on the order of kHz, and causes both atoms to leave the trap.
As this process is caused by two-body collisions, it depends on the density of the atomic species $n_b$ and thus on the atom number of the BEC. Specifically, one expects

$$\dot{N}(t) \propto \int \mathrm{d}^3\mathbf{r}\Gamma_{bb} n_b^2(\mathbf{r}, t) \tag{3.2}$$



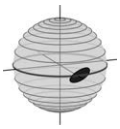

with the two-body loss coefficient $\Gamma_{bb}$. In the Thomas-Fermi regime, the chemical potential is $\mu \propto N^{2/5}$ [93]. The corresponding scaling of the wave function leads to loss rates of $\dot{N}(t)/N \propto N_0^{2/5}$ for two-body loss and $\dot{N}(t)/N \propto N_0^{4/5}$ for three-body processes [94].
We experimentally extract this atom number dependence by preparing different initial atom numbers in state $|b\rangle$ and varying the hold time. Up to 140 ms, we see no deviation from an exponential decay and thus parametrize the corresponding loss rate with the 1/e lifetime $\tau$ of the atomic cloud. We find strong dependence on atom number and a lifetime of $\tau_{z=1} = 210(8)$ ms for $N_0 = 500$ atoms (right panel of Fig. 3.4). A fit of $\tau_{z=1}$ versus initial atom number $N_0$ of the form $\tau \propto N_0^{-2/5}$, which is expected for a Thomas-Fermi profile, yields good agreement with the experimental data.

### Inelastic Feshbach loss

Close to the Feshbach resonance, the loss for binary mixtures of atoms in $|a\rangle$ and $|b\rangle$ is strongly increased due to the coupling to a molecular level, which enhances inelastic two- and three-body collisions [88, 87, 92]. These loss processes occur due to molecule formation and enhanced scattering into lower internal states, which releases the corresponding energy. Depending on the process, this energy is on the order of the corresponding Zeeman shift (in our case $\approx 6$ MHz), the hyperfine spacing (in our case $\approx 6.8$ GHz), or the vibrational energy of the excited molecular state (in the infrared range). For all cases, this is much larger than the depth of the trapping potential, and the atoms are removed from the trap.
These loss rates depend on the density of both components and thus are maximized for equal atom numbers $N_a = N_b$ in both components, i.e. for the population imbalance $z = (N_b - N_a)/(N_b + N_a) = 0$.
Here, we focus on this situation (see left panel of Fig. 3.4), as we prepare our atoms in equal superpositions of the two components for the generation of spin squeezing. We find a strong dependence on the total number of atoms, which is well described by $\tau \propto N_0^{-4/5}$, pointing at three-body processes as the dominant loss source, and a lifetime of $\tau_{z=0} = 107(2)$ ms for an initial atom number of $N_0 = 500$. This means that during typical evolution times of $t_{\text{evo}} = 20$ ms for the generation of squeezed states, approximately 85 atoms are lost from the condensate, corresponding to 17% of the total ensemble size.

## 3.5. Parameter Dependence on Atom Number

In our system, both nonlinear interaction strength $\chi$ and the mean-field detuning $\delta$ depend on the total number of atoms, as can be seen from the Eq. 2.7 and 2.21. The exact dependences of these parameters are non-trivial as they are governed by the change of the single-particle wave functions $\phi_i(\mathbf{x})$ with atom number. In principal, this can be calculated by numerically determining the ground state wave functions from the corresponding Gross-Pitaevskii equation for different atom numbers. However, such results critically depend on the exact values of the trap parameters and the different scattering lengths, which are not known well enough for a precise prediction of the behavior in our system.

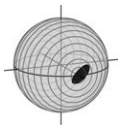

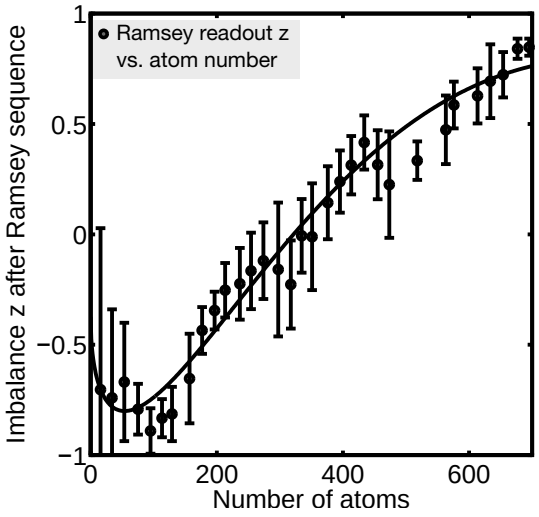


Figure 3.5.: **Extraction of the collisional shift from the N dependent phase shift of a Ramsey sequence** The atom number dependence of the collisional shift can be extracted from Ramsey measurements away from the Feshbach resonance. We find an atom number dependent population imbalance after the Ramsey sequence, corresponding to different phase shifts during the evolution time of 30 ms. We fit an empirical dependence of $\delta(N) = \delta_n\sqrt{N}$ according to Eq. 3.3 and find $\delta_{\mathrm{MFS}} = -0.79(2)\sqrt{N}$. This corresponds to a linearized shift of 57 atoms/Hz for 500 atoms.

Experimentally, the determination of these quantities is challenging because their size is on the order of a few Hertz, which necessitates measurement times of tens of milliseconds. Especially for large atom numbers, the loss processes described in section 3.4 are on similar time scales and complicate the extraction of the parameters as they change during the detection process.

### Mean field detuning

Changes of the transition frequency due to collisional shifts can be characterized by measuring atom number dependent phase shifts in Ramsey sequences. These shifts are proportional to $\delta_\chi = (\chi_{bb} - \chi_{aa})/2$ and thus independent of the interspecies interaction strength $\chi_{ab}$. This allows us to determine the atom number dependence of the mean field detuning at magnetic fields further away from the Feshbach resonance, where the performance of the Ramsey sequence is not degraded by nonlinear effects during the interrogation time.
Fig. 3.5 shows the dependence of the detected population imbalance after a Ramsey sequence with 30 ms evolution time at a magnetic field of 9.2 G, where the nonlinear interaction induced by the Feshbach resonance is negligible. We empirically model the detuning dependence with



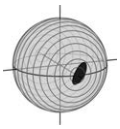

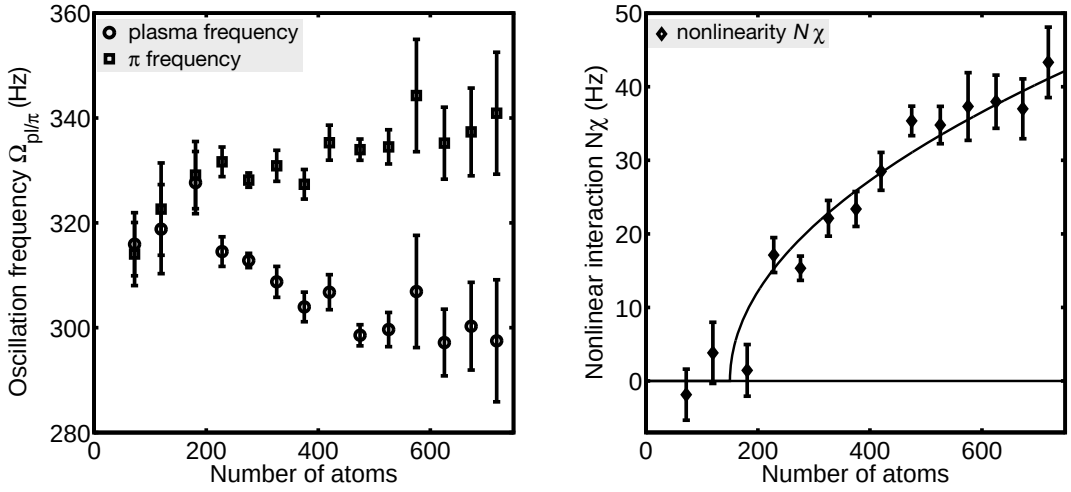


Figure 3.6.: **Strength of the nonlinearity $N\chi$ versus atom number.** The atom number dependence of the nonlinear interaction is clearly visible from the change of the frequencies of plasma (squares) and $\pi$ (circles) oscillations with atom number (left panel), which is given by $\omega_{\text{pl}/\pi} = \Omega\sqrt{1 \pm \Lambda}$. The resulting strength of the nonlinearity $N\chi$ is shown in the right panel. An empirical fit of $a\sqrt{x-b}$ is given as a guide to the eye. For typical atom numbers around 500, we find $N\chi \approx 2\pi \times 30$ Hz.

atom number as $\delta_n\sqrt{N}$, yielding an atom number dependent imbalance of

$$z_N = \mathcal{V}\sin\left(2\pi[\delta_n\sqrt{N} - \delta_0]t_{\text{int}}\right) \tag{3.3}$$

using the visibility $\mathcal{V}$ of the Ramsey fringe, the detuning offset $\delta_0$ and the Ramsey interrogation time $t_{\text{int}}$. Such a square root dependence is expected from the fact that our BEC is close to the Thomas-Fermi regime, where the interaction energy scales as $N^{2/5}$ [93]. Fitting Eq. 3.3 to the experimental data, we find $\delta_{MFS} = -0.79(2)\sqrt{N_f}$ for the atom number $N_f$ detected after 30 ms evolution time at 9.2 G (see Figure 3.5). This corresponds to a linearized shift of 57 atoms/Hz for 500 atoms. Note that atom loss during the evolution time caused by spin relaxation from $F = 2$ is not included in this analysis. As the dependence was calculated for the *final* atom number, which is compressed by the loss process, the actual dependence on the *initial* atom number is expected to be $\approx 5\%$ lower. Also, for the strongly increased loss close to the Feshbach resonance, the observed dependence of the parameters on the final atom number after the same evolution time appears stronger. This is because the nonlinear loss processes decrease differences in particle number, and thus rescale the atom number axis.

### Nonlinearity

The atom number dependence of the strength of the nonlinearity can be extracted from plasma and $\pi$ oscillations after appropriate postselection on atom number using Eq. 3.1. We experimentally find a clear dependence of both frequencies on atom number (left panel of Fig. 3.6).

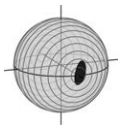

The resulting change of the nonlinear interaction also empirically resembles a square root behavior for larger atom numbers (right panel of Fig. 3.6). For our typical number of 500 atoms, we find a nonlinear interaction strength of around $2\pi \times 30\,\mathrm{Hz}$.

## 3.6. High Intensity Absorption Imaging

The precise knowledge of both the atom numbers in the different hyperfine components and the corresponding detection noise is essential for applications and also for the proper characterization of the generated states and the limits of our experimental system. Absorption imaging is the most common and well-established imaging method for ultracold quantum gases, as it offers high sensitivity in the regime of low and medium densities [95]. In this section, we will give a short introduction into the current setup and the theoretical background, and identify the limits for this technique. We will also shortly discuss alternative imaging scenarios such as phase-contrast imaging or fluorescence detection, which might even allow the detection of mesoscopic BECs with single atom resolution in the future [63].

### 3.6.1. Experimental Details

In our setup, the atom numbers of the different Zeeman sublevels of both hyperfine manifolds in the ground state of $^{87}$Rb are detected via high-intensity absorption imaging after Stern-Gerlach separation of the different magnetic sublevels. Here, we shortly summarize the imaging procedure used throughout this thesis, which is described in detail in [62].
In the experiment, we use an objective with a numerical aperture of 0.45 and a focal length of $f_1 = 31.23\,\mathrm{mm}$ (see [96] for a detailed description). A secondary lens with a focal length of $f_2 = 1000\,\mathrm{mm}$ images the cloud onto a back-illuminated deep depletion CCD camera (Princeton Instruments PIXIS BR1024), which is operated in Fast Kinetics Mode. The corresponding magnification of the imaging system including all optical elements is 30.96. The depth of field is 6.8 µm, which is much larger than the spatial extent of the atomic cloud. Taking into account the quadratic pixel size of 13 µm of the CCD camera, this setup yields a pixel size in object space of 420 nm, which is smaller than the attainable resolution of 1.1 µm according to the Rayleigh criterion. This is important in order to ensure the validity of the Beer-Lambert law employed in the imaging analysis, as detailed below. Additionally, the spatial resolution of 1.1 µm allows optically resolving the single lattice sites, which are separated by 5.5 µm.
Stray light from the dipole traps, in particular caused by the lattice beams at 820 nm which also enter the imaging system, is filtered out by two interference filters (Semrock BrightLine HC 780/12). These are centered at the employed D2 line of $^{87}$Rb at 780 nm and have a width of 24 nm. The total quantum efficiency of the imaging system including all optical elements and the CCD camera is calculated to be 79%.



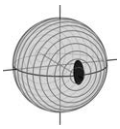

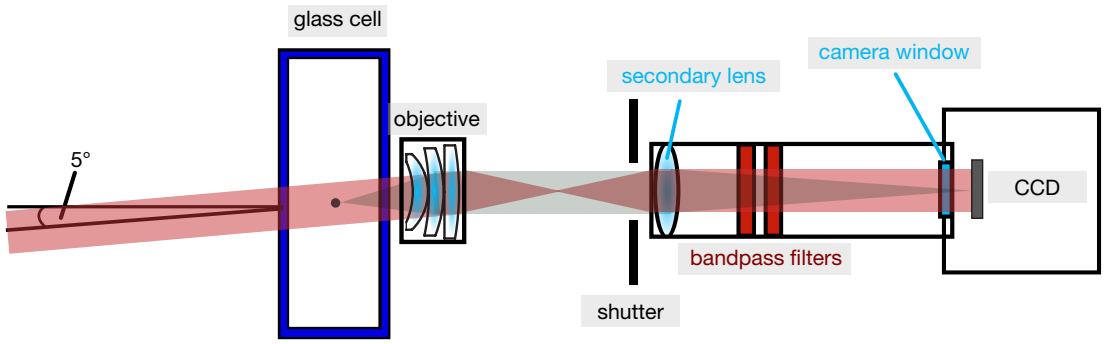


Figure 3.7.: **Schematic setup of the imaging system including all optical components.** The atomic cloud is imaged with an imaging beam (waist $\approx 2$ mm) which enters the experimental chamber under an angle of 5° to avoid etalon effects at the glass surfaces. The shadow of the atomic cloud is then imaged onto a PIXIS BR1024 CCD camera using a custom made objective (NA of 0.45, $f_1 = 31.23$ mm) and a secondary lens ($f_2 = 1000$ mm). Off-resonant stray light is blocked by two bandpass filters centered at the D2 line of $^{87}$Rb. Before the start of the imaging sequence, a mechanical shutter keeps out spurious resonant stray light.

### Imaging sequence

After each experimental pulse sequence, all atoms from state $|b\rangle$ are transferred to $|c\rangle$ using a resonant microwave $\pi$ pulse. This prevents further spin-relaxation loss from the $F = 2$ manifold and thereby allows a controlled ramp-down of the magnetic bias field to around 1 G, where the imaging sequence is performed. Additionally, this has the advantage that both spin states are imaged under symmetric conditions and in a single shot, reducing the effects of technical imperfections.
After a hold time of 300 ms, which is necessary to achieve stable conditions after the ramp-down of the field, the imaging sequence is started. We record 5 subsequent CCD images in frame shift mode, which is set to an exposure time of 600 µs and 656 µs for shifting of the frame. The first four images are exposed to imaging light, whereas the last 'dark' frame is used to extract the level of the offset added by the readout amplifier before the analog-to-digital conversion.
The sequence is initiated by switching off the dipole trap and applying a Stern-Gerlach gradient pulse to spatially separate the different $m_F$ states. At the end of the first exposure time, we apply a resonant $\pi$ polarized imaging pulse on the $5S_{1/2}, F = 2 \leftrightarrow 5P_{3/2}, F' = 3$ cycling transition with a duration of 15 µs and typical intensities of $I \approx 10$ saturation intensities. This first pulse images the atoms in the $F = 2$ manifold of the ground state. All atoms resonant to the imaging light are accelerated out of the trap by the radiation pressure of the pulse (see [62] for details). After the frame shifting time, repumping light is shone onto the atoms. This transfers all atoms from the $F = 1$ manifold of the ground state to $F = 2$ and allows sub-

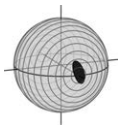

sequent imaging with a second imaging light pulse after a total time-of-flight of 1.3 ms. A reference image that does not contain atoms is recorded 1.25 ms later, employing the same pulse duration and light intensity. On the fourth frame, this is repeated to ensure that residual light scattering on the previous shifted frames is equivalent on the absorption and the reference image.

### 3.6.2. Theory of High-Intensity Absorption Imaging

The basic analysis method in high-intensity absorption imaging of ultracold atomic clouds is the integration of the Beer-Lambert law with the inclusion of saturation effects [97]. In this section, we will give a brief introduction and derive the relevant results for our imaging system.
The Beer-Lambert law for the intensity $I$ of resonant light in a saturable absorber with density $n(x, y, z)$ reads

$$\frac{dI}{dz} = -n(x, y, z)\sigma_0 \cdot \left( \frac{1}{\alpha + \frac{I}{I_{\text{sat}}}} \right) \cdot I, \tag{3.4}$$

where $\sigma_0$ is the (polarization dependent) scattering cross section of the transition, $I_{\text{sat}}$ denotes the effective saturation intensity and $\alpha$ is a dimensionless parameter correcting for polarization and optical pumping effects.
Rearranging the terms yields

$$\left( \frac{1}{\alpha I_{\text{sat}}} + \frac{1}{I} \right) dI = -\frac{n(x, y, z)\sigma_0}{\alpha} dz. \tag{3.5}$$

This differential equation can be solved by integrating both sides over the extent of the cloud, yielding the column density

$$n(x, y) = \int_{z_i}^{z_f} n(x, y, z)\, dz = -\frac{\alpha}{\sigma_0} \left[ \ln\left( \frac{I_{\text{f}}}{I_{\text{i}}} \right) + \frac{I_{\text{f}} - I_{\text{i}}}{\alpha I_{\text{eff}}} \right], \tag{3.6}$$

using the initial and final intensities $I_{\text{i}}$ and $I_{\text{f}}$ before and after the cloud. Further integration in $x$ and $y$ direction over each pixel yields the atom number for a single pixel

$$N_{\text{pix}} = \left[ -\alpha \cdot \ln\left( \frac{I_{\text{f}}}{I_{\text{i}}} \right) - \text{c}_{\text{cam}} \cdot \frac{(I_{\text{f}} - I_{\text{i}})}{I_{\text{sat}}} \right] \cdot \frac{d_p^2}{\sigma_0}, \tag{3.7}$$

using the pixel size in object space $d_p$ and a calibration constant $\text{c}_{\text{cam}}$ which takes into account the calibration of the CCD camera, the quantum efficiency of the imaging system and the duration of the light pulse. Note that the last integration is only valid if the pixel size is smaller than the optical resolution of the imaging system, as it assumes

$$\int_{\text{pixel}} \ln\left( \frac{I_{\text{f}}}{I_{\text{i}}} \right) = \ln\left( \frac{\int_{\text{pixel}} I_{\text{f}}}{\int_{\text{pixel}} I_{\text{i}}} \right), \tag{3.8}$$



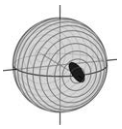

which only holds in the case of small variation across a pixel.
The spatial variation of the light intensity over the image, caused by interference fringes due to the coherent nature of the imaging light as well as other inhomogeneities, necessitates to record both an absorption and a reference image and evaluate Eq. 3.7 for each pixel. The total atom number of the atomic cloud is then obtained by summing over all pixels in a selected region of interest.

### 3.6.3. Calibration of the Imaging System

Using Eq. 3.7, we can calculate the atom number in each pixel if $\alpha$ and $I_{\text{sat}}$ are known. As these parameters depend on the microscopic details of the system (residual detuning of the imaging light, polarization etc.), they have to be determined experimentally. This is done using the projection noise of atomic superposition states with equal population in the two hyperfine levels, as described in [62]. For these coherent spin states, which can be generated with radio frequency and microwave pulses, the variance of the atom number difference $N_- = N_2 - N_1$ of the two hyperfine levels has to be equal to the sum $N_+ = N_2 + N_1$ of both components, i.e. $\text{Var}[N_-] = N_+ + \text{Var}_{\text{Det}}(I)$ for all atom numbers and all imaging intensities $I$ (see section 4.1.1 for a derivation). Here, $\text{Var}_{\text{Det}}(I)$ is the intensity dependent detection noise of the imaging process. An accurate calibration of $\alpha$ and $I_{\text{sat}}$ can thus be obtained if a linear dependence with unity slope is found for the relation of $\text{Var}[N_-]$ versus $N_+$ in a wide range of intensities.

### 3.6.4. Estimation of Detection Noise

The detection noise of our imaging system can be extracted from repeated measurements of images containing no atoms, or evaluation of regions on absorption images where no atoms are found, e.g. above or below the atomic clouds.
The main source of detection noise in our setup is photon shot noise, as our imaging procedure is performed with a classical light source with fluctuating photon number. On each pixel, for a mean photon number $\langle N_{\text{phot}} \rangle$, we expect fluctuations of at least $\sigma_{N\text{phot}} = \sqrt{\langle N_{\text{phot}} \rangle}$, which are present on both the absorption and the reference image. This directly translates into an uncertainty in the detected atom number, as can be seen from error propagation of Eq. 3.7 with respect to the detected intensities $I_{\text{i}}$ and $I_{\text{f}}$. This yields

$$\text{Var}_{\text{Det}}(N_{\text{pix}}) = \frac{d_p^4}{\sigma_0^2} \left( \left[ \frac{\alpha}{I_{\text{f}}} + \frac{\text{c}_{\text{cam}}}{I_{\text{sat}}} \right]^2 \text{Var}(I_{\text{f}}) + \left[ \frac{\alpha}{I_{\text{i}}} + \frac{\text{c}_{\text{cam}}}{I_{\text{sat}}} \right]^2 \text{Var}(I_{\text{i}}) \right). \tag{3.9}$$

We can obtain $\text{Var}(I_{\text{i}})$ and $\text{Var}(I_{\text{f}})$ from the pixel intensities $I_{\text{i}}$ and $I_{\text{f}}$ using a noise calibration of the CCD camera. This is performed employing homogeneous illumination of the chip with an incoherent light source and evaluating the corresponding variances in the count number for each mean number of counts. For this analysis, variations in the sensitivity of the single pixels, which cause a quadratical noise contribution for large count numbers, are canceled using a flat-field correcting analysis.
Using this error propagation, we can assess the photon shot noise contribution for each single

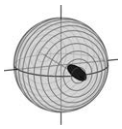

experimental realization on all lattice sites according to the local intensities during the chosen shot. As photon shot noise is the dominant contribution to the detection noise ($\approx 80\,\%$), we use solely this photon shot noise contribution and neglect the other noise sources for subtraction of detection noise (see Sec. 4.1.1). This ensures that we actually subtract the detection noise at the position of the cloud and the result is not perturbed by spatial inhomogeneities of our detection system.
Other noise sources in our imaging system are residual fringes due to the coherent imaging light. Stationary fringes are corrected by the pixel-by-pixel analysis. However, if vibrations of the setup induce movement of the fringe position on the CCD camera between absorption and reference image, they are not perfectly canceled and cause excess noise. Improvements of the experimental stability have reduced this contribution to around 20%. The noise of the readout amplifier of the CCD camera is much smaller than fringe noise and photon shot noise ($\approx 1\,\%$) and can be neglected in the analysis.
For the full atomic cloud, the corresponding detection noise depends on the size of the evaluated region of interest, as it is given by the sum over all pixels, i.e. $\mathrm{Var}_{\mathrm{Det}} = \sum_{\mathrm{roi}} \mathrm{Var}_{\mathrm{Det}}(N_{\mathrm{pix}})$. It is thus optimal to only evaluate the pixels actually containing atoms in order to avoid excess noise. We first manually select rectangular regions of interest around each lattice site. In post-processing, we subsequently select an area around the atomic sample that has the same elliptical shape as the cloud. We make sure that no atomic signal is lost by this elliptical mask by varying the size of the ellipse in both directions. The optimal shape of the mask is chosen such that the deduced atom number inside the selected region is well saturated. This reduction of evaluation size allows to reduce the detection noise by almost 50% [62], yielding typical values of $\sigma_{\mathrm{Det}}(N_{\mathrm{i}}) = \sqrt{\mathrm{Var}_{\mathrm{Det}}(N_{\mathrm{i}})} = 5 - 6$ atoms for a single cloud. Note that for binary condensates as in the experiments discussed within this thesis, two of these atomic clouds have to be imaged, leading to a detection noise in the atom number difference of $\sigma_{\mathrm{Det}}(N_-) = \sqrt{2}\sigma_{\mathrm{Det}}(N_{\mathrm{i}})$.
Further noise reduction can be obtained by applying a fringe removal algorithm, which constructs an optimal reference image as a linear combination from a set of reference images $R_{x,j}$ [98]. The coefficients $c_j$ for the optimal reference image $Q_x = \sum_j c_j R_{x,j}$ are attained by minimizing the least squares difference between the absorption and reference images in a region containing no atoms, i.e. above and below the atomic clouds. This procedure was originally developed to minimize the large fringe noise contribution in atom chip experiments, but also strongly reduces the photon shot noise of the reference image due to the averaging over many images. We routinely apply this algorithm in post analysis using 700 reference images. This reduces the detection noise down to $\sigma_{\mathrm{Det}}(N_{\mathrm{i}}) = 3.7$ atoms for a single cloud [62], corresponding to $\sigma_{\mathrm{Det}}(N_-) = 5.2$ atoms for atom number differences. For a two-component ensemble containing 600 atoms, this should allow the observation of interferometric precision down to $-13.5$ dB below the standard quantum limit.



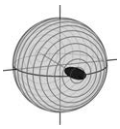

### 3.6.5. Limits of Absorption Imaging and Alternatives

In our setup, the attainable sensitivity for atom number detection with absorption imaging is limited by photon scattering, which both exerts radiation pressure and heats up the sample. For our settings, the maximum duration of the imaging pulse is 15 µs, as after this time the atoms have moved out of the focal plane of the imaging system [62]. This limits the best achievable sensitivity to the level of 3-4 atoms. A detailed discussion about these limitations can be found in [99].
Further improvement in the detection procedure would thus require alternative routes. Fluorescence imaging has shown the feasibility of detecting mesoscopic ensembles with single atom resolution [63] at the cost of losing spatial resolution. Here, one of the major challenges is the additional implementation of a scheme for state-selective simultaneous detection of several components. Near-resonant phase contrast imaging should also deliver a superior signal-to-noise ratio for our densities [99], but involves further complication in imaging setup and analysis.

Note that these improvements will be relevant for the detection of quantum interference, e.g. of non-trivial entangled states, at the single-particle level. For implementation of quantum-enhanced interferometry with squeezed states, this is not crucial, as the atom shot noise of the quantum state is much larger than the currently obtainable detection noise and no features in the distribution functions on the single-atom level are expected.

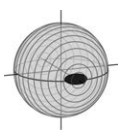

# 4. One-Axis Twisting: Spin Squeezing in a Two-Mode BEC

In the previous chapters, we have introduced the basic experimental properties and the corresponding Hamiltonians that govern the internal dynamics of the individual condensates in each of the lattice sites. In the following, we will theoretically describe and experimentally investigate these dynamics and verify the generation of spin squeezed states by use of the one-axis twisting Hamiltonian (Eq. 2.22) in such a two-mode system.
We will start by introducing the experimental procedure for the extraction of the squeezing properties of those states and the corresponding parameters, $\xi_{\mathrm{N}}^2$ for number squeezing and $\xi_{\mathrm{S}}^2$ for spin squeezing, which is relevant for quantifying the quantum resources contained in the system. In addition, we will introduce a relative squeezing parameter that measures the fluctuations between two condensates in a differential analysis, and thus gives access to the quantum fluctuations of the system without being sensitive to technical common mode noise. Subsequently, we will show the theoretical prediction for the temporal evolution of states under the one-axis twisting Hamiltonian, and analyze the influence of atom loss on the generation of squeezed states. Finally, we will discuss how this scheme is implemented in the experiment and study the temporal evolution and the atom number dependence of the squeezing parameters in our system.

## 4.1. Experimental Characterization of Squeezing

The experimental characterization of quantum states is one of the essential tasks in quantum metrology. For mesoscopic systems, a full quantitative tomographic reconstruction of the density matrix is unfeasible due to its extreme size and the inability to detect populations with single atom resolution.
Gaussian states are fully characterized by their means and variances. They can thus be characterized by measuring the quantum uncertainty along multiple directions, which can be quantified in terms of squeezing parameters.
Squeezed states have elongated uncertainty distributions. Its key parameters are given by the extension of the elongated *long axis* of the state as well as the compressed *short axis* of minimal fluctuations, and the angle $\alpha_{\mathrm{min}}$ along which these fluctuations are minimized (Fig. 4.1). Experimentally, we can access the quantum uncertainty along the $z$ direction from the fluctuations of the population imbalance $z = (N_b - N_a)/(N_b + N_a)$ of the two states in repeated measurements. Here, $N_a$ and $N_b$ denote the number of atoms in each of the two components. A tomographic analysis, i.e. the measurement of the state's quantum uncertainty along different directions, can be implemented by rotating the state around itself before reading out the

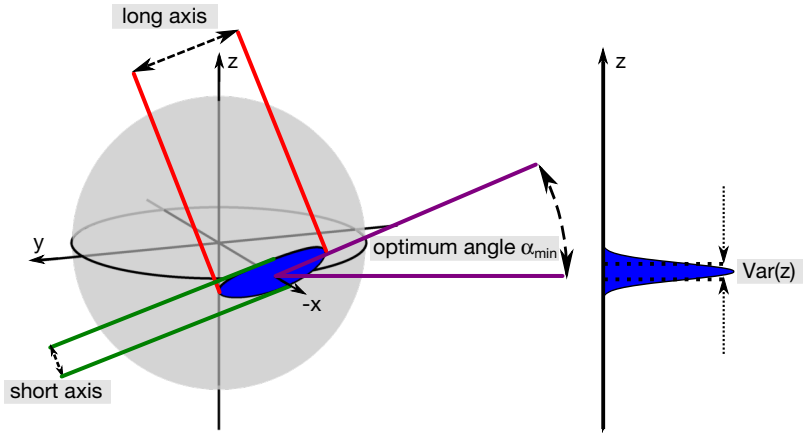


Figure 4.1.: **Characterization of a squeezed state.** The uncertainty of a squeezed state is characterized using three parameters (left panel): The extension along the elongated direction of the state (*long axis*), the length along the *short axis* of optimal number squeezing with the corresponding spin squeezing parameter, and the tomography rotation angle $\alpha_{\text{min}}$ to rotate the state onto this axis of optimal squeezing. The squeezing parameters are obtained from the variance of the fluctuations along the $z$ direction (right panel). A tomographic analysis is implemented by rotating the state around itself via two-photon coupling.

atomic populations. In our experiment, such a rotation can be induced by phase-controlled two-photon coupling.
In this section, we will show how the obtained fluctuations can be quantified in terms of squeezing factors and discuss the meaning and applicability of the different squeezing parameters.

### 4.1.1. Classical Limit: Fluctuations for N Independent Particles

We will start by examining the lower classical limit for the quantum fluctuations, which is reached by a coherent spin state (see section 2.4). For such a state, we expect isotropic quantum uncertainty and a binomial probability distribution. This can be intuitively understood in terms of a probabilistic analysis of $N$ particles [100], each of which is in an independent superposition state $|\psi\rangle = \sqrt{1-p}|a\rangle + \sqrt{p}|b\rangle$, where $p = (\langle z\rangle + 1)/2$ is the probability of finding the single atom in state $|b\rangle$. For $N$ independent particles, the probability of measuring $N_b$ particles in state $|b\rangle$ is thus given by

$$P(N_b; N, p) = \frac{N!}{N_b!(N-N_b)!} p^{N_b}(1-p)^{N-N_b}. \tag{4.1}$$

The variance of this binomial distribution can be shown to be

$$\text{Var}(N_b; N, p) = \text{Var}(N_a; N, 1-p) = p(1-p)N, \tag{4.2}$$

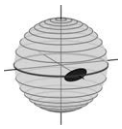

and the covariance

$$\mathrm{Cov}(N_a, N_b; p) = -p(1-p)N \tag{4.3}$$

has the same absolute value but opposite sign. Using Eq. 4.2 and 4.3, we consequently expect fluctuations in the difference of the particle number in the two states of

$$\mathrm{Var}(N_a - N_b)_{\mathrm{CSS}} = \mathrm{Var}(N_a) + \mathrm{Var}(N_b) - 2\,\mathrm{Cov}(N_a, N_b) = 4p(1-p)N \tag{4.4}$$

for a coherent spin state of $N$ particles. This variance is maximal for an equal superposition [$\mathrm{Var}(N_a - N_b) = N$ for $p = 0.5$] and vanishes for maximal population imbalance [$p = 0, 1$]. In terms of fluctuations of the population imbalance $z = (N_b - N_a)/N$, this translates into

$$\mathrm{Var}(z)_{\mathrm{CSS}} = \frac{\mathrm{Var}(N_a - N_b)}{N^2} = \frac{4p(1-p)}{N} = \frac{1 - \langle z \rangle^2}{N}. \tag{4.5}$$

### 4.1.2. Fluctuation Suppression: Number Squeezing $\xi_{\mathrm{N}}^2$

A suppression of fluctuations below this classical limit can be parametrized by the so-called number squeezing factor

$$\xi_{\mathrm{N}}^2 = \frac{\mathrm{Var}(z)_{\mathrm{exp}}}{\mathrm{Var}(z)_{\mathrm{CSS}}} = \frac{N \cdot \mathrm{Var}(z)_{\mathrm{exp}}}{4p(1-p)}. \tag{4.6}$$

In the experiment, the observed fluctuations $\mathrm{Var}(z)_{\mathrm{exp}}$ are not solely given by the quantum fluctuations of the state. Additionally, the detection noise of the imaging system as well as technical fluctuations during the state preparation add to these quantum fluctuations. For a proper characterization of the state's properties and resources, we can correct for known noise sources by subtracting the independently characterized fluctuations induced by these processes.

Of the above mentioned additional noise sources, the dominant contribution in our setup is the well-characterized detection noise of the absorption imaging [62]. A detailed description of the imaging procedure, our setup and its characterization is given in section 3.6. For a single lattice site, the detection noise yields additional fluctuations of $\mathrm{Var}_{\mathrm{Det}}(N_i) \approx 15$ atoms for each detected component $N_i$. The largest contribution of these fluctuations is caused by photon shot noise of the imaging light.

Additional technical noise due to imperfections during state preparation can be characterized by exploiting the parallelized production of independent BECs (see section 6.3). These fluctuations scale quadratically with atom number and are small if one analyzes single lattice sites in our system. In the case of large atom numbers, these fluctuations will eventually dominate and require a differential analysis, which will be detailed in section 4.1.4.

For the following analysis in this thesis, we only subtract the detection noise $\mathrm{Var}_{\mathrm{Det_{PS}}}$, which accounts for the photon shot noise contribution, from the observed experimental variances, as this can be independently characterized for each shot. Including this subtraction, the inferred number squeezing parameter is given by

$$\xi_{\mathrm{N}}^2 = \frac{N \cdot (\mathrm{Var}(z)_{\mathrm{exp}} - \mathrm{Var}_{\mathrm{Det_{PS}}}/N^2)}{4p(1-p)}. \tag{4.7}$$



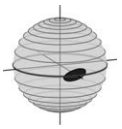

## 4.1.3. Spin Squeezing

The parameter that is directly connected to the entanglement properties and the phase sensitivity in an interferometer is the spin squeezing factor $\xi_S^2$ [25, 101], which was already introduced in section 2.5. In addition to the suppression of fluctuations, the parameter $\xi_S^2$ also accounts for the coherence of the quantum state. In particular, the mean spin length of a squeezed state is reduced due to the elongated nature of the quantum state. This results in a decreased visibility for the fringes obtained in Ramsey experiments.

### Spin squeezing parameter using classical expectation values

In the two-mode approximation, in which all particles in each state share the same spatial mode $\phi_i(\mathbf{x})$, the mean spin length can be directly extracted from the extension of the uncertainty of the state. If we assume that our state is a squeezed state which is strongly elongated along a certain axis and compressed in orthogonal direction, this mean spin length will be determined by the extension of the long axis.
Assuming that the pseudospin points in $x$ direction, i.e. $\langle \hat{J}_y \rangle = \langle \hat{J}_z \rangle = 0$, and the long axis of the state is aligned with the equator, the mean spin length for large $N$ and small population imbalance $z$ can be approximated by using the mean-field description as in Eq. 2.37, yielding

$$\langle \hat{J} \rangle = \langle \hat{J}_x \rangle = \frac{N}{2} \langle \cos(\phi) \rangle, \tag{4.8}$$

where $\phi = \arctan(J_y/J_x)$ [45] . This can be used to quantify the underlying spin squeezing [101, 44, 45] with the spin squeezing parameter

$$\xi_S^2 = \frac{2J \cdot \mathrm{Var}(\hat{J}_z)}{\langle \hat{J}_x^2 \rangle + \langle \hat{J}_y^2 \rangle} = \frac{\xi_N^2}{\langle \cos(\phi) \rangle^2}, \tag{4.9}$$

where we neglect the extension of the state along its short axis.
In this approximation, $\xi_S^2$ can be directly extracted from a tomographic squeezing analysis. This will be employed for characterizing the squeezing of the single lattice sites – for which the two-mode approximation is valid – as it does not require additional measurements of the visibility that can be obtained with the final states. However, in the case of squeezing in sums of several lattice sites, the two-mode approximation and thus Eq. 4.8 does not hold, and this method is not applicable.
Recall that spin squeezing serves as an entanglement witness [44, 77, 102, 103], which has been used to identify atomic entanglement for mesoscopic ensembles in several experimental realizations [5, 45, 46, 47]. This quantum resource can be employed for enhancing the performance of atomic clocks [40, 41], quantum metrology [45, 37, 48] and generally be used as a resource for quantum information tasks [104].

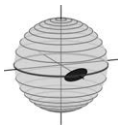

### Metrological spin squeezing parameter

The metrological spin squeezing parameter $\xi_R^2$, as defined by *Wineland et al.* [101], is valid beyond the two-mode approximation, as it extracts the spin length directly from the experimentally obtainable fringe visibility $\mathcal{V}$. Thus, this parameter also takes into account technical imperfections of the experimental system that lead to a reduced visibility and consequently quantifies the actual gain that can be achieved in a measurement. It is defined by

$$\xi_R^2 = \frac{\xi_N^2}{\mathcal{V}^2}, \tag{4.10}$$

which results in a possible improvement of $\xi_R$ for the phase sensitivity in comparison to a classical state, i.e. $\Delta\phi = \xi_R/\sqrt{N}$. Intuitively, this can be understood from error propagation for the phase $\phi \propto \arcsin(z/\mathcal{V})$ estimated from a sinusoidal Ramsey fringe. Here, the number squeezing decreases the phase uncertainty due to the decreased fluctuations in $z$, whereas the reduced visibility $\mathcal{V}$ reduces the slope of the sinusoidal fringe and thus deteriorates the sensitivity. A more detailed discussion on the phase estimation with spin squeezed states will be given in chapter 7.1.

## 4.1.4. Relative Squeezing

An analysis relying on the fluctuations of repeated measurements does not directly quantify the quantum uncertainty of the state. It is also sensitive to detection noise and additional noise sources connected to shot-to-shot variations of the experimental parameters, such as detunings induced by magnetic fields or preparation errors due to power fluctuations of the microwave sources.

Our 1D lattice setup allows the simultaneous generation of multiple squeezed ensembles in a single experimental realization. Technical fluctuations of homogeneous fields affect all lattice sites in the same way. This is why an analysis of the relative fluctuations between the lattice sites is insensitive to these common mode variations, and thus gives insights into the true quantum fluctuations of the state. In the following, we will develop the tools for a such a differential analysis. We will introduce a squeezing parameter $\xi_{\text{rel}}$ which quantifies the suppression of relative fluctuations between two atomic ensembles. This parameter is connected to the gradiometric sensitivity for these detectors, and equivalent to the number squeezing parameter in the case of equal atom numbers in both samples.

For the relative analysis, we analyze two atomic clouds with the respective population imbalances $z_1 = \frac{N_{1-}}{N_{1+}}$ and $z_2 = \frac{N_{2-}}{N_{2+}}$, where $N_{i+(-)}$ are the sum (difference) of the populations of the states $|a\rangle$ and $|b\rangle$ in cloud $i$. The relevant noise suppression in the relative analysis is found in the imbalance difference $\delta z = z_1 - z_2$. It is intuitive that common mode variations of both samples due to technical noise do not contribute to the fluctuations of $\delta z$, as they are canceled by the subtraction.

Analog to the case of a single two-component cloud, we first examine the classical limit of



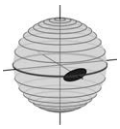

this system. Here, in analogy to section 4.1.1, the classical limit is given by

$$\mathrm{Var}(\delta z)_{\mathrm{class}} = \left[\mathrm{Var}\left(\frac{N_{1-}}{N_{1+}}\right) + \mathrm{Var}\left(\frac{N_{2-}}{N_{2+}}\right)\right]_{\mathrm{class}} = \frac{c_1}{N_{1+}} + \frac{c_2}{N_{2+}}, \tag{4.11}$$

using the binomial factors $c_1 = 4p_1(1-p_1)$ and $c_2 = 4p_2(1-p_2)$ accounting for the mean imbalances $\langle z_1 \rangle$ and $\langle z_2 \rangle$. Note that in the case of equal atom numbers and $\langle z_1 \rangle = \langle z_2 \rangle = 0$, this simplifies to $\mathrm{Var}(\delta z)_{\mathrm{class}} = 4/N$ with the total number of atoms $N = N_{1+} + N_{2+}$.
Also, we find that the minimal value for $\mathrm{Var}(\delta z)_{\mathrm{class}}$ is obtained for $N_{1+} = N_{2+}$, assuming $\langle z_1 \rangle = \langle z_2 \rangle = 0$. This can be seen by replacing $N_{2+} = kN$ (with $0 \leq k \leq 1$) and $N_{1+} = (1-k)N$, yielding

$$\mathrm{Var}(\delta z)_{\mathrm{class}} \propto \frac{1}{k(1-k)}, \tag{4.12}$$

which is minimal for $k = 1/2$. This shows that it is best to distribute $N$ particles into two clouds of equal size, as otherwise the increased quantum noise of the cloud with lower particle number dominates the variation of $\delta z$. As this variance $\mathrm{Var}(\delta z)$ is related to the attainable sensitivity in gradiometric operation, this also shows that the best performance of a gradiometer is attained with two samples of equal size.
Analogous to the number squeezing analysis, the relative squeezing factor is defined as the ratio between the experimentally measured variance and the classical limit, yielding

$$\xi^2_{\mathrm{rel}} = \frac{\mathrm{Var}(\delta z)_{\mathrm{exp}}}{\mathrm{Var}(\delta z)_{\mathrm{class}}} \approx \frac{N_{\mathrm{tot}}}{4} \cdot \mathrm{Var}(\delta z)_{\mathrm{exp}}, \tag{4.13}$$

where the last approximation holds for $N_{1+} \approx N_{\mathrm{tot}}/2$ and $\langle z_1 \rangle \approx \langle z_2 \rangle \approx 0$ as above.
We will now examine how this relative squeezing parameter $\xi^2_{\mathrm{rel}}$ is related to the number squeezing parameter $\xi^2_{\mathrm{N}}$ of the sum of both samples. In the absence of technical (i.e. common mode) fluctuations, we find that

$$\xi^2_{\mathrm{rel}} = k \cdot \xi^2_{\mathrm{N}_1} + (1-k) \cdot \xi^2_{\mathrm{N}_2}, \tag{4.14}$$

using the individual number squeezing parameters $\xi^2_{\mathrm{N}_1}$ and $\xi^2_{\mathrm{N}_2}$ and assuming $c_1 = c_2$. Summing the atom numbers of the individual components in both samples and calculating the number squeezing parameter yields

$$\xi^2_{\mathrm{N}_{\mathrm{tot}}} = (1-k) \cdot \xi^2_{\mathrm{N}_1} + k \cdot \xi^2_{\mathrm{N}_2}. \tag{4.15}$$

Thus, for similar atom numbers or identical individual number squeezing parameters, $\xi^2_{\mathrm{rel}}$ is equivalent to the number squeezing parameter of the total cloud. In our case, both of these conditions are well fulfilled and $\xi^2_{\mathrm{N}_{\mathrm{tot}}} \approx \xi^2_{\mathrm{rel}}$, allowing direct comparison between the two parameters.
To obtain the sensitivity for metrological applications, in analogy to the number squeezing evaluation, the visibilities of the Ramsey fringes $\mathcal{V}_1$ and $\mathcal{V}_2$ have to be taken into account. For

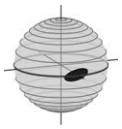

equal visibilities $\mathcal{V}$, the corresponding gradiometric spin squeezing parameter is thus given by

$$\xi^2_{\mathrm{S_{rel}}} = \frac{\xi^2_{\mathrm{rel}}}{\mathcal{V}^2}. \tag{4.16}$$

## 4.2. Creating Spin Squeezing in a Bose-Einstein Condensate

We will start this section by shortly reviewing the pathways that have been experimentally realized for generating spin squeezed states in BECs so far, and then add a detailed discussion of the one-axis twisting scenario, which has up to now been the standard route for spin squeezing in the internal states of Bose-Einstein condensates.

### 4.2.1. Nonlinearity and Squeezing in a Two-Component BEC

Spin squeezing in Bose-Einstein condensates has been achieved employing a variety of experimental methods. In the external degrees of freedom, squeezing was realized using controlled tunnel coupling between adjacent lattice sites, which can be precisely adjusted via the optical or magnetic trapping potentials [5, 47]. These experiments employed adiabatic ramping of the barrier height to generate spin squeezing in the population imbalance of the two sites.
In the internal states, the attainable nonlinearities are much lower, which makes the adiabatic methods unfeasible due to atom loss during the consequential long ramping times [89]. Here, squeezing has to be realized employing diabatic methods such as one-axis twisting.
As shown in chapter 2, the required nonlinear interaction in the internal degrees of freedom between the states $|a\rangle$ and $|b\rangle$ is given by

$$\chi \propto a_{aa} \int \mathrm{d}\mathbf{r} |\phi_a(\mathbf{r})|^4 + a_{bb} \int \mathrm{d}\mathbf{r} |\phi_b(\mathbf{r})|^4 - 2a_{ab} \int \mathrm{d}\mathbf{r} |\phi_a(\mathbf{r})|^2 |\phi_b(\mathbf{r})|^2 \tag{4.17}$$

and thus depends on both the scattering lengths $a_{ij}$ between the particles and the shape of the spatial wave functions $\phi_i(\mathbf{r})$. For $^{87}$Rb, the background scattering lengths between all hyperfine states of the $5S_{1/2}$ ground state are very similar. For example, for the states considered in this thesis, the intra- and interspecies scattering lengths are given by $a_{aa} = 100.44\, a_{\mathrm{B}}$, $a_{bb} = 95.47\, a_{\mathrm{B}}$ [86] and $a_{ab} = 97.7\, a_{\mathrm{B}}$ [105], where $a_{\mathrm{B}}$ denotes the Bohr radius. This means that $\Delta a_{\mathrm{NL}} = a_{aa} + a_{bb} - 2a_{ab} = 0.51\, a_{\mathrm{B}}$ is negligible. Thus for condensates in two perfectly overlapping spatial modes, i.e. $\phi_a(\mathbf{r}) = \phi_b(\mathbf{r})$, the nonlinearity vanishes.

Experimentally, two different pathways have been employed for increasing this nonlinear interaction. In the group of Philipp Treutlein, significant interaction strength has been attained by applying state-dependent potentials [46]. This leads to a spatial separation of the two wave functions $\phi_a(\mathbf{r})$ and $\phi_b(\mathbf{r})$ and consequently decreases the overlap integral $\int \mathrm{d}\mathbf{r} |\phi_a(\mathbf{r})|^2 |\phi_b(\mathbf{r})|^2$. Thus, the three terms in Eq. 4.17 do not cancel and significant nonlinearity prevails, which is strong enough to be employed for entanglement generation [46].
In our setup, we follow a different approach [89] and tune the interspecies scattering length $a_{ab}$



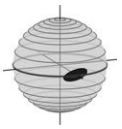

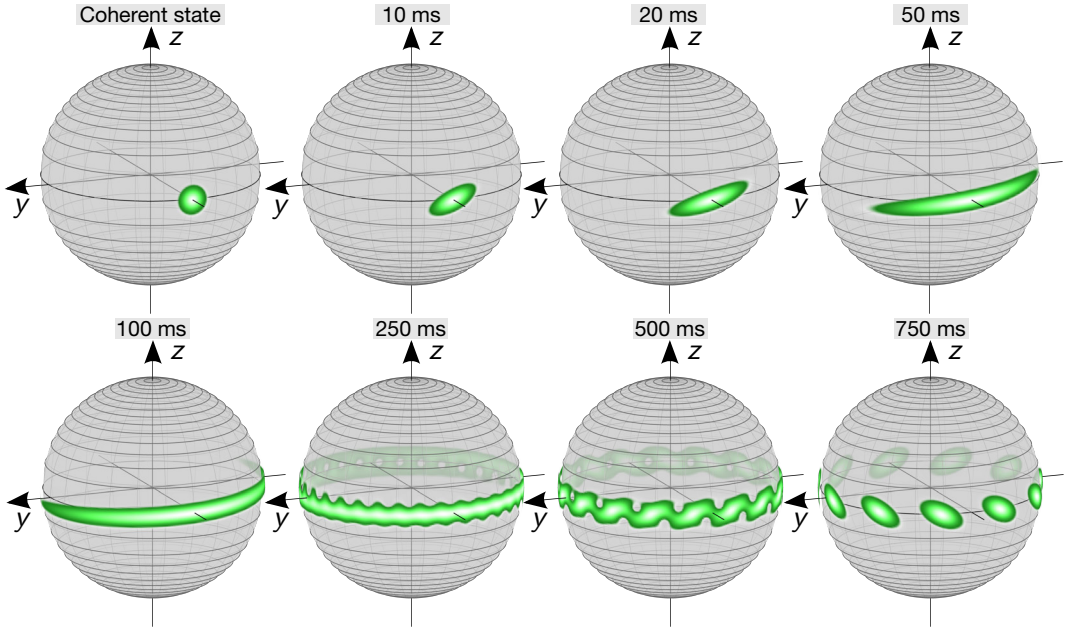


Figure 4.2.: **Ideal theoretical one-axis twisting evolution.** The initially isotropic quantum uncertainty of a coherent spin state (Husimi distribution in leftmost panel in upper row) gets redistributed due to the shearing which is caused by the nonlinearity. In the first stage of the evolution, an elongated squeezed state is generated (upper row). The aspect ratio of the state grows for longer evolution times as squeezing is enhanced. For even larger evolution times, the state evolves into a regime of non-trivial states with non-Gaussian uncertainty distribution, which are no longer squeezed (lower row). Eventually, this scenario theoretically allows the generation of maximally entangled states. The Husimi plots were obtained for 500 atoms and the experimentally obtained nonlinearity of $N\chi = 2\pi \times 30\,\mathrm{Hz}$ by diagonalizing the Hamiltonian 2.22. Loss and time-dependence of parameters, which strongly alter the evolution, are not included in these simulations.

by use of an interspecies Feshbach resonance at 9.1 G [85, 86], which is experimentally characterized in section 3.2. For our system, due to the similar scattering lengths we can assume $\phi_a(\mathbf{r}) \approx \phi_b(\mathbf{r}) = \phi(\mathbf{r})$. In this case, Eq. 4.17 simplifies to

$$\chi \propto \int \mathrm{d}\mathbf{r} |\phi(\mathbf{r})|^4 \left[a_{aa} + a_{bb} - 2a_{ab}\right]. \tag{4.18}$$

The nonlinearity in our system thus only depends on the shape of the spatial wave function and the distance of the magnetic field to the Feshbach resonance. As shown in the previous section, at the chosen magnetic field of 9.12 G – which is a trade-off between increased nonlinearity and strongly decreased lifetime due to Feshbach losses closer to the resonance – we find $N\chi \approx 2\pi \times 30\,\mathrm{Hz}$ for typical atom numbers of $N \approx 500$, and a 1/e lifetime of 110 ms.

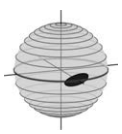

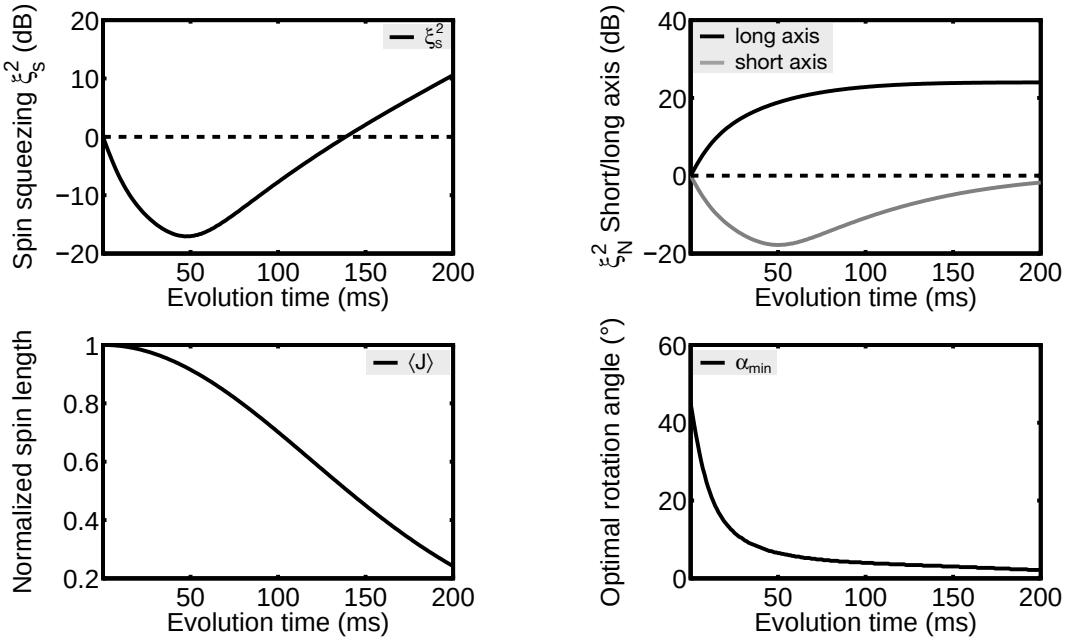


Figure 4.3.: **Spin squeezing generated by one-axis twisting vs time.** In the ideal theory, spin squeezing builds up in the early part of the time evolution and reaches its optimum after 47 ms (upper left panel). Subsequently, spin squeezing rapidly vanishes, which is mainly due to the reduction of the mean spin length $\langle J \rangle$ (lower left panel) due to the increasing extension of the long axis (solid black line, upper right panel), but also caused by reduced best number squeezing (solid gray line, upper right panel). The angle of optimal squeezing decreases with time, as the state gets stretched further and further by the nonlinear interaction (lower right panel).

### 4.2.2. Generating Spin Squeezing with One-Axis Twisting

The one-axis twisting Hamiltonian $\mathcal{H} = \chi \hat{J}_z^2 + \delta \hat{J}_z$ (see Eq. 2.22) thus can be realized by preparing atoms in an independent superposition of the two levels by use of a strong linear coupling pulse, and then evolving the state under the influence of the nonlinearity. As the Hamiltonian only consists of terms containing $\hat{J}_z$ and higher orders, no change in relative population is caused by the nonlinear evolution. In the Bloch sphere picture, the detuning term $\delta \hat{J}_z$ induces a rotation around the $z$ axis, leading to a time-dependent phase of the quantum state without changing its shape. In contrast, the nonlinear $\chi \hat{J}_z^2$ term causes a rotation around the $z$ axis whose speed depends on the population imbalance $z$. For a quantum state, which has a finite width in $z$ direction due to its intrinsic quantum uncertainty, this causes a shearing along the $z$ axis and thus redistributes the quantum uncertainty of the state. This generates squeezing in the early parts of the time evolution and is connected with the introduction of quantum correlations between the particles.

This scenario for the creation of spin squeezed states was proposed by *Kitagawa et al.* in



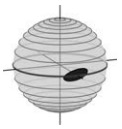

1993 [25] and experimentally realized in Bose-Einstein condensates in 2010 [45, 46]. Note that also some procedures which rely on atom-light interaction, such as the cavity feedback squeezing scheme realized with cold atomic clouds [39], are based on similar Hamiltonians.
A simulation of the idealized temporal evolution for an initial coherent state subjected to the one-axis twisting Hamiltonian is depicted in Fig. 4.2 on a generalized Bloch sphere. It was calculated using exact diagonalization of the one-axis twisting Hamiltonian Eq. 2.22. We find that the isotropic quantum uncertainty of the initial coherent spin state is redistributed, leading to an elongated state with reduced quantum uncertainty in the direction orthogonal to its longest extension, i.e. a spin squeezed state. The projection along the $z$ direction does not change and remains at the classical shot noise limit, which necessitates further rotations of the state before it can be read out or exploited for quantum-enhanced interferometry.
Longer squeezing times lead to a larger aspect ratio, until the state starts to stretch around the whole sphere. At this point, highly entangled quantum states with non-trivial structure are formed and spin squeezing is lost. The characterization and application of these states requires more advanced schemes which do not rely solely on variances [11, 61]. Note that in our experiment this regime is inaccessible due to the inherent atom loss, which happens on a timescale on the order of $100\,\mathrm{ms}$ and strongly modifies the dynamics for long evolution times. In the further course of this thesis, we will focus on the early part of the temporal evolution and characterize the corresponding spin squeezed states that are generated during this period.
We now turn to a quantitative analysis of the spin squeezing parameter $\xi_S^2$ versus evolution time. We first investigate the ideal case using realistic experimental conditions (500 atoms, $N\chi = 2\pi \times 30\,\mathrm{Hz}$), but neglect detunings and the effect of losses. These processes lead to a time dependence of the interaction strength $N\chi$ and the detuning $\delta$, and additionally deteriorate the squeezing due to the stochastic nature of the loss [28].
The theoretical analysis for this ideal system shows that optimal squeezing of $\xi_S^2 = -17.1\,\mathrm{dB}$ can be attained for an evolution time of 47 ms (Fig. 4.3). At this time, the state already extends over a large part of the sphere, meaning that the mean spin length $\langle \hat{J} \rangle$ has already strongly decreased. The angle of minimal quantum uncertainty, which is relevant for the readout rotation, also depends on the evolution time (right panel).

We now address the two most important imperfections of our system. The major source of complication is the effect of the inevitable losses, which strongly alters this idealized evolution. The presence of these losses, caused by spin relaxation from the excited state and the proximity of the Feshbach resonance, limits the 1/e lifetime of our system to $\tau \approx 110\,\mathrm{ms}$. As the parameters $\chi$ and $\delta$ both depend on the total atom number, this strongly modifies the subsequent dynamics.
The fundamental problem, however, is the stochastic nature of the loss process, which causes decoherence and limits the attainable best squeezing. Fig. 4.4 shows the influence of the decoherence caused by the different loss processes on the attainable spin squeezing, neglecting the effects of parameter changes at first. These results were obtained from Monte Carlo simulations of the time evolution following the approach of *Mølmer et al.* [106, 107] for an initial atom number of $N_0 = 500$ atoms, with $N\chi = 2\pi \times 30$ Hz and $\delta = 0$ constant in time. The corresponding loss parameters for two-body spin relaxation loss from the excited state $\Gamma_{bb}$

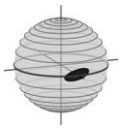

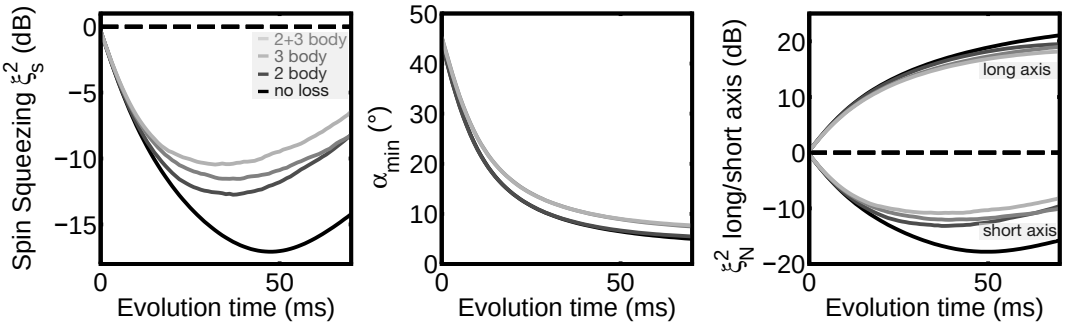


Figure 4.4.: **Decoherence due to atom loss and their effect on spin squeezing.** The results depicted in this figure are obtained from numerical Monte Carlo simulations of the one-axis twisting scheme in the presence of different loss processes, for constant parameters $N_0 = 500$, $N\chi = 2\pi \times 30\,\text{Hz}$ and $\delta = 0\,\text{Hz}$. The different colors depict the different loss scenarios: No loss (black), spin-relaxation two-body loss (dark gray), three-body Feshbach loss (medium gray) and both two-body and three-body loss (light gray). We find a strong degradation of the best attainable spin squeezing $\xi_S^2$ from both loss effects (left panel), accompanied with a shift of the optimal squeezing time from 47 ms to 32 ms. The optimal rotation angle $\alpha_{\text{min}}$ (middle panel) as well as the extension of the long axis (upper branch in right panel) change only slightly due to the losses, whereas the best number squeezing is strongly affected (lower branch in right panel).

and three-body loss from the Feshbach resonance $\Gamma_{abb} = \Gamma_{aab}$ were adjusted according to the experimentally determined lifetimes of $\tau_{\text{2body}} \approx 210\,\text{ms}$ and $\tau_{\text{3body}} \approx 110\,\text{ms}$, respectively.
The results of the Monte Carlo method show that both loss processes cause decoherence and modify the attainable squeezing even without parameter change. The isolated effect of the inevitable two-body spin relaxation limits spin squeezing to $\xi^2_{\text{S}_{\text{2body}}} = -12.7\,\text{dB}$ and lowers the optimal time to 37 ms. Similar effects are obtained for three-body loss from the Feshbach resonance, for which the optimal squeezing reduces to $\xi^2_{\text{S}_{\text{3body}}} = -11.5\,\text{dB}$. The combined effect of both loss sources is predicted to limit the spin squeezing parameter to $\xi^2_{\text{S}_{\text{loss}}} = -10.5\,\text{dB}$, which can be attained after an optimal time of 32 ms. Both the length along the long axis and the angle of minimal fluctuations $\alpha_{\text{min}}$ are only slightly affected by these processes.
The previously discussed calculations only take into account the fundamental limitations due to decoherence caused by the atomic loss. In a realistic experimental scenario, the dynamics will be further modified by the parameter change caused by the loss process. This is demonstrated in Fig. 4.5, where a parameter dependence of $\chi \propto 1/\sqrt{N}$ and $\delta \propto \sqrt{N}$ is assumed (see section 3.5), starting with $N\chi = 2\pi \times 30$ Hz and $\delta = 0$. Due to the reduced nonlinearity during the squeezing process, the speed of the squeezing generation is reduced. This leads to a smaller extension of the state and a larger optimal rotation angle $\alpha_{\text{min}}$. Additionally, we find a further deterioration in the best attainable spin squeezing, which is now given by $\xi_S^2 = -10\,\text{dB}$ after 28 ms evolution time.



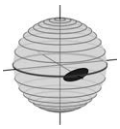

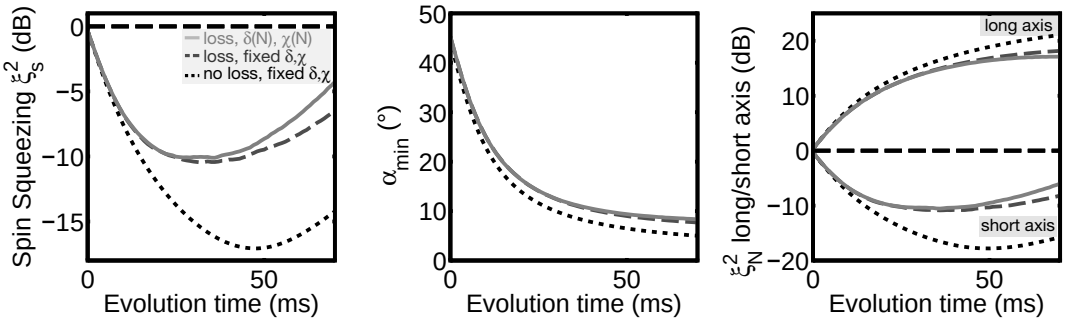


Figure 4.5.: **Influence of losses including the change of parameters.** During the one-axis twisting evolution, the parameters $\delta$ and $N\chi$ are time-dependent, as they change with the decaying number of atoms. This leads to a further degradation of the attainable spin squeezing (left panel, light gray solid line) in comparison to the case of time independent parameters, where only the effect of decoherence from two- and three-body loss are considered (dashed dark gray line), and the lossless case (dotted black line). Due to the reduced mean nonlinearity, both the optimal angle gets larger (middle panel) and the long axis is shortened (right panel). These results were obtained from Monte Carlo simulations assuming $N\chi \propto \sqrt{N}$ and $\delta \propto \sqrt{N}$.

Another important experimental imperfection is the presence of technical fluctuations of the experimental parameters, for example uncontrolled jitter of the detuning $\delta$. After an evolution time $\tau$, a fixed finite detuning $\delta$ does not degrade the generation of squeezed states in the one-axis twisting scheme, but leads to a phase shift $\varphi = 2\pi\delta\tau$ for the optimal readout rotation. Fluctuating detunings, however, which are experimentally inevitable due to the finite stability of the magnetic offset fields, lead to varying readout phases and thus affect the measured squeezing parameters. Experimentally, this necessitates the implementation of a spin-echo sequence, in which a $\pi$ rotation in the middle of the nonlinear evolution reduces the influence of the phase noise. A detailed analysis of these technical fluctuations and the performance of the $\pi$ pulse in the presence of nonlinearity will be given in section 6.3.

### 4.2.3. Experimental Implementation of the One-Axis Twisting Scenario in an Interacting BEC

The Feshbach-enhanced nonlinearity can be employed for the generation of spin squeezed states using the one-axis twisting scheme, as was demonstrated by *Gross et al.* with two-mode Bose-Einstein condensates [45]. In this section, we will show how the creation and characterization of these states is implemented in the experiment and focus on the dynamics of the individual condensates, ignoring the existence of the lattice at first.

The experimental procedure for the generation of squeezed states starts with all atoms in the state $|a\rangle$ at the homogeneous magnetic bias field of 9.12 G in close proximity to the Feshbach

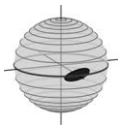

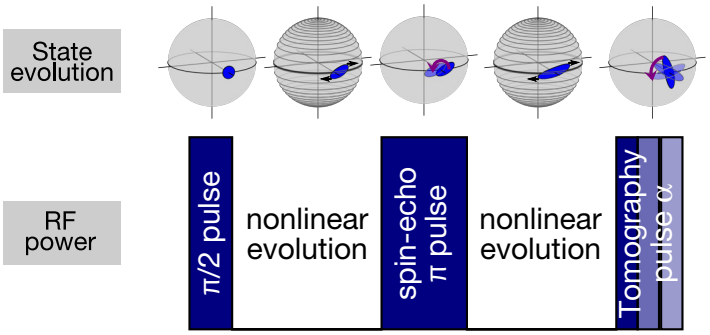


Figure 4.6.: **Experimental implementation of one-axis twisting scheme.** For the generation and characterization of spin squeezed states, we first prepare an equal superposition of both components by use of a two-photon $\pi/2$ pulse. This initial coherent spin state subsequently evolves under the influence of the nonlinear interaction, which is enhanced due to the proximity of the Feshbach resonance. After half of the evolution time, a spin-echo $\pi$ pulse (phase $\phi = 3\pi/2 + 3°$) is performed to reduce the influence of detuning fluctuations. After a second period of nonlinear evolution, a readout pulse with variable duration (phase $\phi = 3\pi/2 + 3°$ for $-180° < \alpha < 0°$ and $\phi = \pi/2 + 3°$ for $0° < \alpha < 180°$) rotates the final state by the angle $\alpha$ around itself.

resonance, yielding an interaction strength in the order of $2\pi \times 30$ Hz for 500 atoms. In the first step, we create an equal superposition of the two components $|a\rangle$ and $|b\rangle$ by applying a $\pi/2$ pulse of resonant two-photon microwave and RF radiation (see Fig. 4.6). The Rabi frequency for all pulses employed in this scenario is set to $\Omega = 2\pi \times 310$ Hz. Note that the nonlinearity is also present during the coupling pulses and shifts the initial phase of the created coherent spin state by $\approx 3°$. This phase shift is accounted for by adjusting the phases of the subsequent pulses accordingly.

After this pulse, the coupling is switched off, and the state evolves under the influence of the nonlinearity. This experimentally realizes the one-axis twisting Hamiltonian. To reduce the effects of detuning fluctuations resulting from the finite stability of the magnetic bias field, we apply a spin-echo $\pi$ pulse with two-photon coupling after half of the total evolution time, i.e. $t = t_{\text{evo}}/2$. This pulse has a phase of $\phi = 3\pi/2 + 3°$. Note that the rotation angle is effectively shortened by 5% due to the nonlinear interaction, which reduces the frequency of the $\pi$ oscillations. Section 6.3.2 will give a detailed analysis of the effects resulting from this imperfection, as this will be relevant for the scalability of number squeezing within the 1D array. Also, the shorter rotation slightly reduces the angle $\alpha_{\text{min}}$ of minimum quantum uncertainty after the pulse, which changes the dynamics in the second half of the time evolution and thus has to be accounted for in the simulations. Specifically, the smaller angle leads to a reduced spread of the quantum uncertainty in $z$ direction and thus reduces the squeezing rate for the second part of the evolution.

After the spin-echo pulse, we let the state evolve for another period of duration $t_{\text{evo}}/2$. Finally, tomographic characterization is implemented with a two-photon pulse that rotates the



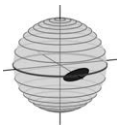

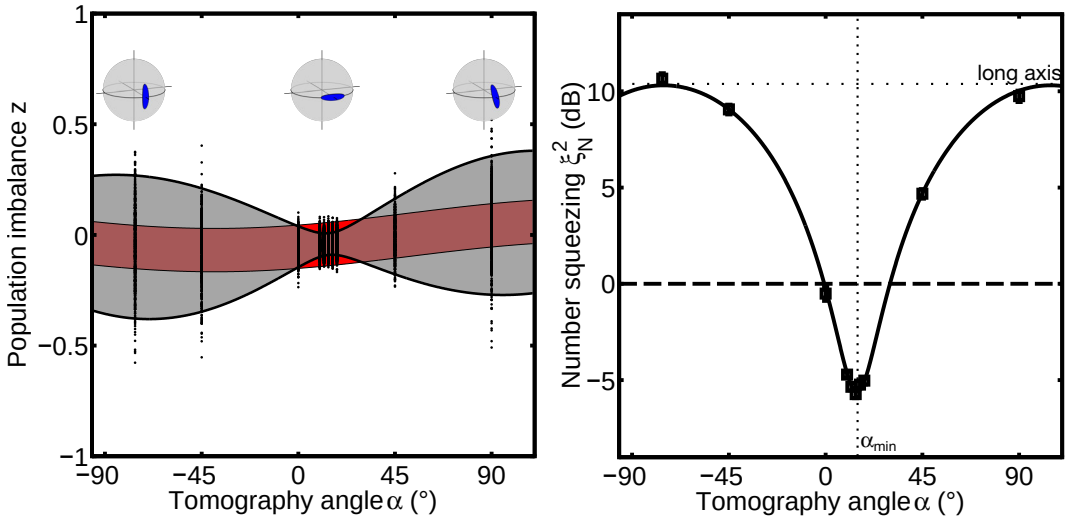


Figure 4.7.: **Tomographic squeezing evaluation after 20 ms of one-axis twisting evolution.** After the evolution, the final state is rotated around itself with a two-photon pulse of variable length. For a state with $N_0 = 500$ atoms, we observe a strong angular dependence of the fluctuations in the population imbalance $z$ for repeated measurements (left panel), and a slightly varying mean imbalance. This is caused by a small imbalance of the final state resulting from losses, and a slight phase mismatch of the final rotation pulse. The observed fluctuations (the gray shaded band denotes the 95% confidence interval obtained from a sinusoidal fit to the variance) along a certain axis are reduced below the expected values of a classical coherent spin state (red shaded band). This can be quantified in terms of the number squeezing parameter $\xi_N^2$ (right panel), which shows a distinct minimum at the tomography angle $\alpha_{\text{min}} = 14°$. Here, we find $\xi_N^2 = -6.2(3)$ dB below the classical limit. In orthogonal direction, along the long axis of the state, the fluctuations are increased by a factor of 10.

state around itself. To avoid long coupling times, the phase for this readout pulse is adjusted such that $\phi = 3\pi/2 + 3°$ for $-180° < \alpha < 0°$ and $\phi = \pi/2 + 3°$ for $0° < \alpha < 180°$. To avoid further spin relaxation loss after the experimental sequence, the atoms are transferred to the state $|c\rangle$ using a one-photon microwave pulse. Subsequently, the magnetic bias field is ramped down to 1 G, and after 300 ms the two components are imaged using resonant absorption imaging. This procedure is repeated several hundreds of times for each tomography angle, and the fluctuations of these measurements are employed for a tomographic characterization of the state.

The results of such a tomographic analysis are shown in Fig. 4.7 for a state generated after an evolution time of $t_{\text{evo}} = 20$ ms with the spin-echo sequence described above. The observed fluctuations of the population imbalance $z$ vary for different readout rotation angles $\alpha$ in a sinusoidal manner. As expected for a squeezed state, for a certain angular range the fluctuations are smaller than those expected for a coherent spin state, and enlarged in orthogonal direction.

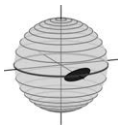

Note that also the mean value $\langle z \rangle$ after the readout rotation has a small sinusoidal dependence on the tomography angle $\alpha$. This is due to both a finite population imbalance before the readout pulse due to the asymmetric influence of spin-relaxation loss, and a slight phase mismatch of the readout rotation axis.
For a quantitative analysis, we calculate the number squeezing parameter $\xi_{\mathrm{N}}^2$ according to Eq. 4.7, which compares the measured fluctuations of $z$ to the quantum uncertainty of a classical coherent spin state with the same number of particles. For this particular realization, we find suppressed fluctuations by $\xi_{\mathrm{N}}^2 = -6.2(3)\,\mathrm{dB}$ for the optimal rotation angle $\alpha_{\mathrm{min}} = 14°$, and an increased uncertainty of more than 10 dB along the orthogonal direction.

### 4.2.4. Experimental Investigation of the Time Evolution

We now experimentally examine the temporal evolution of a state under the one-axis twisting Hamiltonian. Specifically, we want to find the optimal time for generating spin squeezed states with the spin-echo scheme described in the previous section. To do so, we implement this sequence for different evolution times $t_{\mathrm{evo}}$ and perform a tomographic squeezing analysis for each time. For our analysis, we postselect atom numbers according to the experimentally determined loss rate of $\tau = 110\,\mathrm{ms}$, starting with an atom number window of $N_0 = 500 \pm 20$ at $t_{\mathrm{evo}} = 0$.
The initial evolution in the obtained experimental data behaves qualitatively similar to the prediction of the ideal theory. We find that the spin squeezing parameter $\xi_{\mathrm{S}}$ decreases for longer evolution times, and observe a corresponding behavior of the optimal tomography angle $\alpha_{\mathrm{min}}$. Our results also show a continuously increasing extension of the long axis of the state for larger interaction times, as the state gets stretched around the sphere.
Quantitatively, however, we find that spin squeezing settles off in the range of $\xi_{\mathrm{S}}^2 \approx -6\,\mathrm{dB}$ for $t_{\mathrm{evo}} \geq 20\,\mathrm{ms}$, and no further decrease can be observed. As shown in the previous section, we can attribute this partly to the presence of losses, which cause decoherence at a rate that cancels the additional squeezing obtained from the nonlinear evolution, and increasing influence of technical fluctuations at longer times.
Both of these effects are included in a Monte Carlo simulation of the exact pulse sequence, assuming an initial nonlinearity of $N_0\chi = 2\pi \times 30\,\mathrm{Hz}$ and detuning fluctuations of $\sigma_{\mathrm{Det}} = 2\pi \times 0.45\,\mathrm{Hz}$, which corresponds to our long term stability of the magnetic field of 45 µG. The loss rates for three-body Feshbach loss and two-body spin relaxation loss were chosen to match the experimentally observed timescales of 110 and 210 ms, respectively, and the change of nonlinearity and detuning was modeled with a $\sqrt{N}$ dependence. These simulations yield perfect agreement with the experimental data for the long axis and the optimal rotation angle, but predict the optimal spin squeezing to be in the order of $\xi_{\mathrm{S}}^2 \approx -9\,\mathrm{dB}$ (solid black lines in Fig. 4.8).
If we include additional known sources of increased noise during the detection process, we find an optimal squeezing value on the order of $\xi_{\mathrm{S}}^2 \approx -7.5\,\mathrm{dB}$ and thus better agreement with the experimental observations (dashed gray line in Fig. 4.8). The noise sources included here are the effect of fringe noise of the detection scheme, which was not subtracted for this anal-



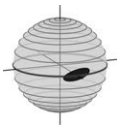

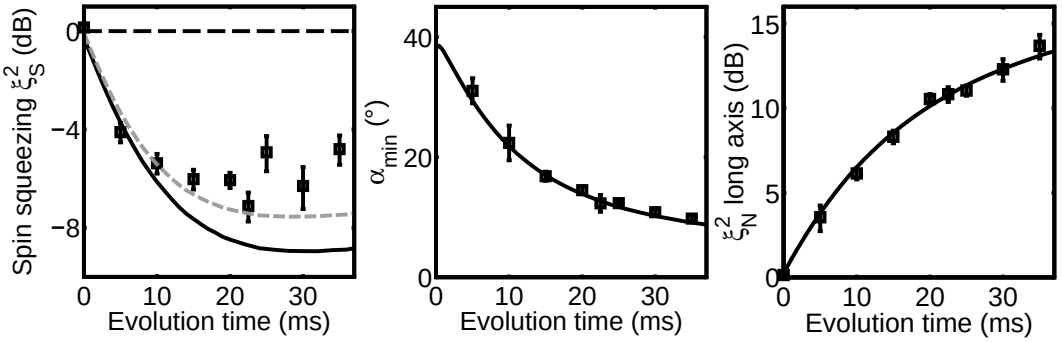


Figure 4.8.: **Experimental results for the temporal evolution of squeezing using one-axis twisting.** Starting with a coherent spin state, we implement the one-axis twisting Hamiltonian using the pulse sequence shown in Fig. 4.6 with varying evolution time. We find that the spin squeezing parameter quickly decreases in the initial evolution and then settles off in the range of $\xi_S^2 \approx -6\,\mathrm{dB}$ for $t_{\mathrm{evo}} \geq 20\,\mathrm{ms}$ (left panel). The corresponding optimal tomography angle $\alpha_{\mathrm{min}}$ decreases as expected (middle panel). The extension of the long axis grows monotonically also for longer evolution times, indicating that the state is twisted even further. Monte Carlo simulations including the spin-echo pulse, parameter changes and technical fluctuations yield perfect agreement for the optimal tomography angle and the long axis (solid lines). The simulated value for the spin squeezing parameter reaches its minimum around $\xi_S^2 = -9\,\mathrm{dB}$. Including an estimate of the additional noise caused by imperfections, i.e. loss during hold time and fringe noise on the image, during the detection process yields better agreement with the experimental data (dashed gray line).

ysis and is equivalent to a variance of approximately 10 atoms. We also take the loss due to background collisions or scattering of photons from the optical dipole traps during the hold time of 300 ms before the imaging sequence into account. These processes limit the lifetime of the BEC in the $F = 1$ manifold to approximately 15 seconds. Even though this only corresponds to the loss of around 8 atoms, this effect becomes an important contribution for the highly squeezed states.
Additional fluctuations that could explain the remaining difference between experiment and theory could be caused by the one-photon state transfer to the state $|c\rangle$ to stop spin relaxation loss before the imaging process. This transfer is on a two times Zeeman sensitive transition and thus could be affected by the fluctuations of the offset field.

### Atom number dependence

The exact shape and characteristics of the final state depend on the initial atom number $N_0$ at the beginning of the state generation. This is because the parameters $\chi$ and $\delta$ that govern the evolution in the one-axis twisting Hamiltonian both depend on atom number, as described in

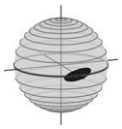

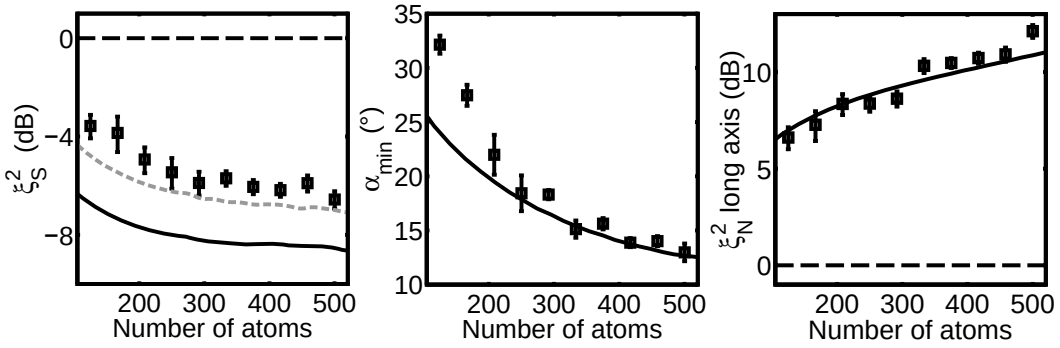


Figure 4.9.: **Dependence of the final state on atom number.** Due to the dependence of the parameters $\chi$ and $\delta$ on atom number (see section 3.5), the properties of the final state after $t_{\text{evo}} = 20\,\text{ms}$ of one-axis twisting evolution also vary with the number of atoms. The strongest variations take place for atom numbers below 300. Above this, both the spin squeezing parameter $\xi_S^2$ (left panel) and the optimal rotation angle $\alpha_{\text{min}}$ (middle panel) depend only weakly on $N$, even though the extension of the state along the long axis still increases (right panel). The solid lines are the results of Monte Carlo simulations assuming $N\chi \propto \sqrt{N}$ and $\delta \propto \sqrt{N}$. The dashed gray line in the left panel additionally includes known noise sources during the detection process.

section 3.5. The effects of this atom number dependence are shown in Fig. 4.9, which depicts the key parameters $\xi_S^2$, $\alpha_{\text{min}}$ and the extension $\xi_N^2$ along the long axis for the final states with different final atom numbers after 20 ms of nonlinear evolution.

We find that for small atom numbers, both the inferred spin squeezing parameter and the optimal rotation angle $\alpha_{\text{min}}$ strongly depend on atom number. A larger nonlinearity leads to stronger shearing of the uncertainty and thus results in better spin squeezing, a lower optimal rotation angle and a longer extension of the state. For atom numbers above 300, however, the dependence of the nonlinearity on $N$ is weaker and results only in small changes for both $\xi_S^2$ and $\alpha_{\text{min}}$. This is an important prerequisite for obtaining simultaneous squeezing in all lattice sites in the presence of an inhomogeneous atom number distribution, which enables the scaling of squeezing to large atom numbers. This will be discussed in chapter 6. The extension of the long axis, which does not have a strong influence on the scalability, increases with growing atom number even for $N > 300$.

These results are qualitatively reproduced with our Monte Carlo simulations, in which we include the spin-echo pulse, the atom number dependence of $\delta_{\text{MFS}} = -2\pi \times 0.63\sqrt{N}\,\text{Hz}$ and $N\chi = 2\pi \times 1.3\sqrt{N}\,\text{Hz}$ and a change of the loss rate with atom number to match the scaling found in the experiment. We find that this theoretical description yields good agreement for larger atom numbers, but deviates in the regime of small atom numbers. This could be caused by the fact that for the BECs with smaller atom numbers, the Thomas-Fermi description is no longer valid. This leads to the strong decrease of nonlinearity which is experimentally found below 300 atoms with an extraction based on plasma and $\pi$ oscillations, as shown in Fig. 3.6.

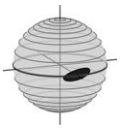

This lower nonlinearity leads to a steeper angle of the final state for small atom numbers. Even though technical fluctuations of $\sigma_{\mathrm{Det}} = 0.45\,\mathrm{Hz}$ are included in the simulation, the simulated spin squeezing is stronger than the experimentally obtained values and falls below $\xi_{\mathrm{S}}^2 = -9\,\mathrm{dB}$. In analogy to the study of squeezing for different evolution times, including known additional noise sources during the detection process, such as loss during hold time and fringe noise, yields better agreement.

For the further experiments in this thesis, we choose the earliest time for which the squeezing value has saturated, which is an evolution time of 20 ms. With this scheme, we can generate states of several hundred atoms with spin squeezing of more than 6 dB in the single lattice sites and only little dependence on the atom number in the relevant regime. This is an important prerequisite for the scalability to large atom numbers, which we will assess in chapter 6.

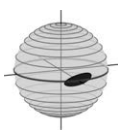

# 5. Instability and Squeezing Dynamics in a BEC

In this chapter, we will investigate the quantum dynamics on the unstable fixed point in the bifurcated regime of the Lipkin-Meshkov-Glick Hamiltonian, and study the dynamical generation of squeezing in this scenario. This system corresponds to an internal bosonic Josephson junction which is created in the spin degree of freedom, and is experimentally realized with an interacting binary Bose-Einstein condensate in the presence of weak interconverting coupling. It is predicted that the preparation of a quantum state onto this unstable fixed point gives access to a rich class of entangled states on a short time scale, ranging from spin squeezed to maximally entangled states [78, 82]. We will study the dynamics of this scenario, and analyze the resulting states in terms of spin squeezing. The results will show the generation of spin squeezed states and thus entanglement in the first part of the time evolution – we will term this dynamical generation scheme *bifurcation squeezing*. For later times, the evolution yields non-Gaussian spin states, where more advanced methods for detecting and exploiting the entanglement have to be employed. This has also been demonstrated experimentally and is summarized in a publication [61].

## 5.1. Quantum Evolution on a Classically Unstable Fixed Point

We will start this chapter by reviewing the quantum dynamics of an idealized system in the bifurcated regime, and investigate how this can be employed for entanglement generation.
In the previous chapter, we discussed the dynamics corresponding to the one-axis twisting Hamiltonian, which was experimentally realized with a binary BEC in the presence of nonlinear interaction. As shown in section 2.6, the topology of the corresponding classical phase space is strongly changed by the addition of linear interconversion. In the pseudospin picture of the quantum description, the Hamiltonian then takes on the form $\mathcal{H}_{\mathrm{LMG}} = \chi \hat{J}_z^2 - \Omega \hat{J}_x + \delta \hat{J}_z$ (Eq. 2.26), which is a special case of the Lipkin-Meshkov-Glick Hamiltonian. On resonance ($\delta = 0$), the corresponding classical phase space exhibits a bifurcation when coupling and interaction strength are equal, i.e. $\Lambda = N\chi/\Omega = 1$. In this situation, an unstable fixed point appears at the position $(\phi = \pi, z = 0)$, which is accompanied by the emergence of two stable fixed points above and below the equator.
The rich dynamics of such a bosonic Josephson junction has been extensively studied in theory [69, 68, 78, 82]. Previous work in our group demonstrated an experimental realization of such a system in the internal states and mapped out the classical phase space for varying values of

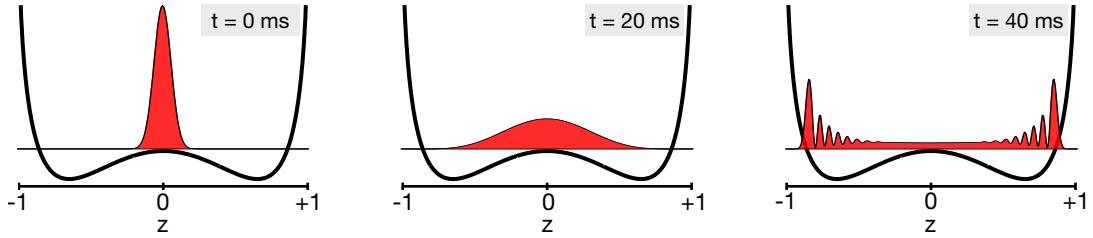


Figure 5.1.: **Evolution of a quantum state in a double well potential.** The quantum dynamics in the bifurcated situation can be captured by the evolution of a Gaussian wave packet which is prepared onto the unstable fixed point of the corresponding double well potential in Fock space, i.e. along the $z$ direction (left panel). Initially, the expulsive potential of the unstable fixed point leads to a fast spreading of the wave packet along the potential (middle panel). This increased uncertainty is accompanied with squeezing in a different direction, which we will analyze later in this chapter. The presence of the two stable fixed points manifests itself for longer evolution times, when peaked probability distributions around the classical turning points of the potential can be found (right panel). At this time, the corresponding quantum state is highly entangled and has a non-Gaussian structure. Thus, the full entanglement properties of the state can not be detected with a squeezing analysis.

$\Lambda$, confirming the occurrence of a bifurcation [70]. However, during these experiments the technical stability did not allow a reproducible preparation of the states close to the unstable classical fixed point, where the quantum dynamics are strongly modified by the finite quantum uncertainty of the state and an analysis solely of the mean values does not suffice.
In the following, we will investigate these quantum dynamics of a state prepared onto the unstable fixed point in the bifurcated scenario. This scheme is predicted to enable the dynamical generation of entangled states on fast timescales [78, 82] compared to the one-axis twisting Hamiltonian. Note that a similar situation is created in the case of spin-exchange dynamics in a three-mode BEC. Employing such a system, unstable quantum dynamics and *spin-nematic* squeezing have been observed in a two-dimensional subspace of the three-mode BEC [108, 52]. In our system, we realize this situation directly in two modes, where the generated quantum resources are accessible with standard techniques, e.g. for metrological applications using Ramsey spectroscopy.

We will start with a closer theoretical examination of the bifurcated system at an experimentally feasible $\Lambda = 1.6$ in the region around $\phi = \pi$, where the unstable fixed point appears in the classical phase space. The essential features of the quantum dynamics in such a system can be grasped in terms of a double well description in its configuration space, which is the corresponding classical potential along the $z$-axis in this situation (see Fig. 5.1).
If a classical particle – which has no extension in configuration space – is positioned close to the central maximum of such a double well potential, the subsequent dynamics of this particle

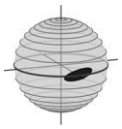

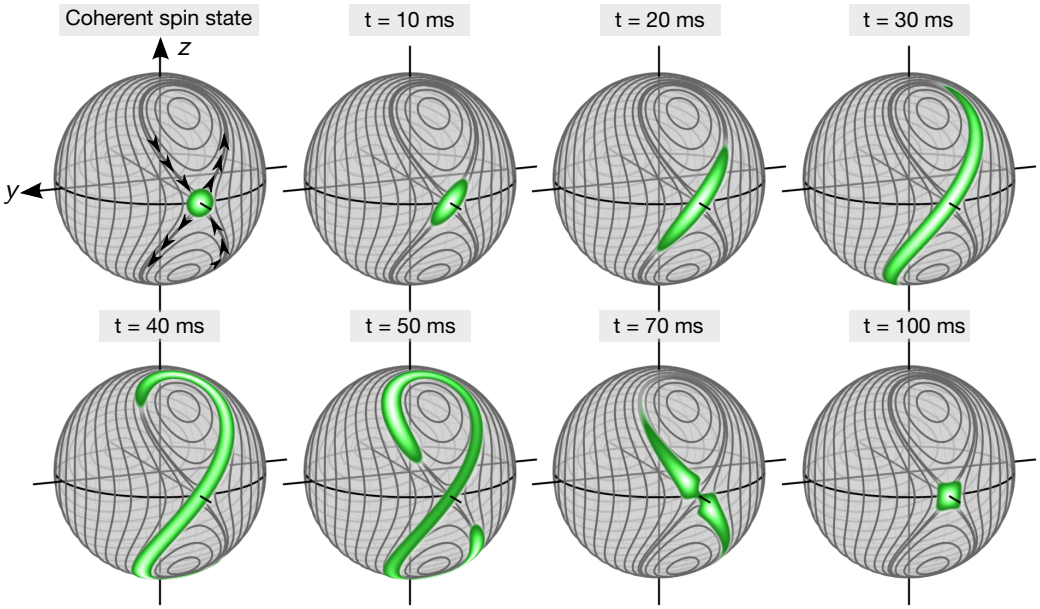


Figure 5.2.: **Quantum evolution on an unstable classical fixed point.** A coherent spin state (Husimi distribution on the leftmost sphere in the upper row) that is prepared on the unstable fixed point in the bifurcated case of the Lipkin-Meshkov-Glick Hamiltonian initially gets compressed along one direction and stretches out along the other axis of the eight shaped separatrix of the corresponding classical phase space. The quantum evolution is obtained by diagonalization of the Hamiltonian Eq. 2.26 with $N\chi = 2\pi \times 30\,\mathrm{Hz}$, $\Omega = 2\pi \times 18\,\mathrm{Hz}$ and $\delta = 0$. The black lines are the corresponding classical trajectories for these parameters. The dynamics leads to strong squeezing in the early part of the time evolution. Squeezing is lost when the state starts to bend around the two stable classical fixed points. The dynamics eventually creates a highly entangled question mark shaped state before it evolves back onto the unstable fixed point. Note that the timescale for the generation of non-Gaussian entangled states is much shorter than in the one-axis twisting case (Fig. 4.2).

is constrained to either the left or the right well of the potential.
The intrinsic quantum uncertainty of the particle drastically changes the situation in a quantum mechanical description, as the wave function of the quantum particle can spread over the maximum of the double well, and thus subsequently evolve into both wells of the potential at the same time. These quantum dynamics of our system, an internal bosonic Josephson junction with a mesoscopic number of particles, can be captured within a semiclassical *WKB approximation* [109]. Within this approximation, the many-particle quantum dynamics for the bifurcated scenario is well described by the quantum evolution of a single particle in a double well potential in Fock space (i.e. along the $z$ direction).
In this description, a coherent state is characterized by a Gaussian wave packet, where the



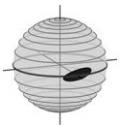

quantum uncertainty is captured by the width of the distribution $\hbar_{\text{eff}} = 1/\sqrt{\text{N}}$. The preparation of such a Gaussian wave packet on the maximum of the double well potential leads to a rapid expansion in Fock space, which is caused by the expulsive harmonic potential of the unstable fixed point. The wave packet spreads further until it reaches the minima of the double well potential, which correspond to the two stable fixed points in the classical phase space. The presence of these minima subsequently manifests itself in peaked probability distributions associated with the classical turning points. In the early part of the evolution, this rapid spreading of the wave packet in the $z$ direction leads to squeezing along a different axis [82].
For a more quantitative description of the dynamics in our experiment, we now turn to the Bloch sphere representation of the temporal quantum evolution for an initial coherent spin state that is prepared onto the unstable fixed point, which we obtain from exact diagonalization of the Hamiltonian. In the ideal (i.e. lossless and resonant) scenario, the state will initially get squeezed along one axes of the separatrix in the corresponding classical phase space (Fig. 5.2). This can be understood in terms of its finite quantum uncertainty that spreads over a large region of this phase space. The classical trajectories within this region compress the state along one of the axes of the eight shaped separatrix, and rip it apart along the other axis.
This initial strong squeezing is lost when the state starts to bend around the two stable fixed points, forming a complex question mark shaped state with non-Gaussian structure. This state is predicted to be highly entangled [78]. Eventually, it will evolve further and the quantum uncertainty will again accumulate in the region around the unstable fixed point.
These quantum dynamics are of great interest for the generation of highly entangled non-Gaussian states, as the timescale for the creation of such states is strongly reduced compared to the one-axis twisting scenario [78]. In this chapter, however, we will focus on the study of mean and variance properties and investigate the generation of squeezing in the early part of the time evolution.

### Detuning dependence of the dynamics

As shown in section 2.6, the presence of a finite detuning $\delta$ strongly alters the shape of the classical phase space, and thus distinctly changes the quantum dynamics of the system. This can be intuitively understood in terms of the classical double well potential in Fock space, which is tilted in the presence of a detuning. This tilt shifts the position of the unstable fixed point along the $z$ axis. Thus, in the detuned case a preparation of an equal superposition will not result in a symmetric preparation on the unstable fixed point, and the quantum state will move in the direction of the tilt (Fig. 5.3). In terms of the classical phase space, the quantum state will evolve around one of the stable fixed points above or below the unstable fixed point, leading to an oscillation of the mean population imbalance $\langle z \rangle$ and phase $\langle \phi \rangle$. In contrast, the situation is symmetric for the resonant case, in which the mean population imbalance and the phase remain $\langle z \rangle = \langle \phi \rangle = 0$ for all times.

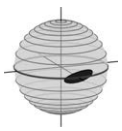

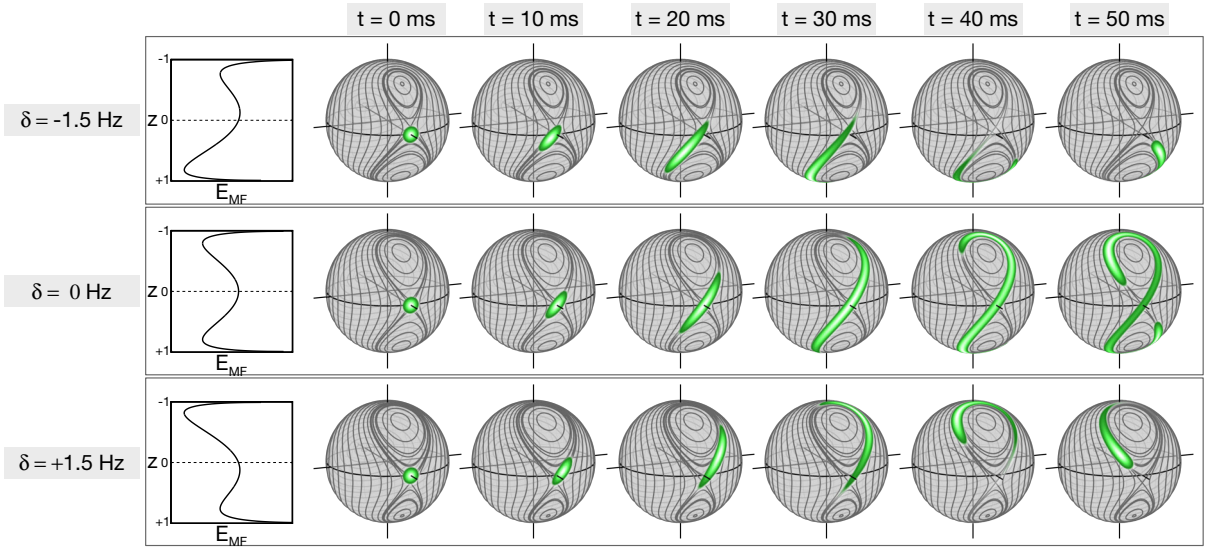


Figure 5.3.: **Detuning dependence of the quantum evolution.** The quantum evolution of the state strongly depends on the choice of the nonlinear interaction strength $\chi$, the Rabi coupling strength $\Omega$ and the detuning $\delta$. A change of the detuning $\delta$ can be understood in terms of a tilt on the corresponding double well potential in Fock space (cut along $z$ for $\phi = \pi$, left column). The upper row depicts the quantum evolution for $N\chi = 2\pi \times 30\,\mathrm{Hz}$, $\Omega = 2\pi \times 18\,\mathrm{Hz}$ and $\delta = -2\pi \times 1.5\,\mathrm{Hz}$, the central row depicts the corresponding resonant case ($\delta = 0$), and the lower row the evolution for $\delta = +2\pi \times 1.5\,\mathrm{Hz}$. Such a detuning difference corresponds to a difference in the initial atom number of $\Delta N_0 \approx 85$ atoms. The three cases show qualitatively very different behavior even for short evolution times, demonstrating the high sensitivity of the dynamics on detuning.

This criticality due to the presence of an instability manifests itself in the sensitivity on the chosen parameters. For realistic experimental parameters, assuming a nonlinear interaction strength of $N\chi = 2\pi \times 30\,\mathrm{Hz}$ and a Rabi frequency of $\Omega = 2\pi \times 18\,\mathrm{Hz}$, even a detuning on the order of $1\,\mathrm{Hz}$ strongly changes the quantum evolution. Fig. 5.3 depicts the simulated quantum evolution for three different detunings, $\delta = -1.5\,\mathrm{Hz}$, $\delta = 0\,\mathrm{Hz}$ and $\delta = +1.5\,\mathrm{Hz}$. Due to the dependence of the collisional shift on the number of atoms, which is experimentally determined to be $\delta_{\mathrm{MFS}} = -0.79(2)\sqrt{N_0}$, a shift of $1.5\,\mathrm{Hz}$ corresponds to a difference in initial atom number of $\Delta N_0 \approx 85$ for our typical range of atom numbers.

## 5.2. Experimental Implementation

We now turn to an experimental investigation of the quantum dynamics in this bifurcated system. To study this, we prepare an initial coherent spin state on the unstable fixed point using a two-photon $\pi/2$ pulse with high coupling strength ($\Omega = 2\pi \times 310\,\mathrm{Hz}$), and then switching



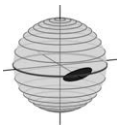

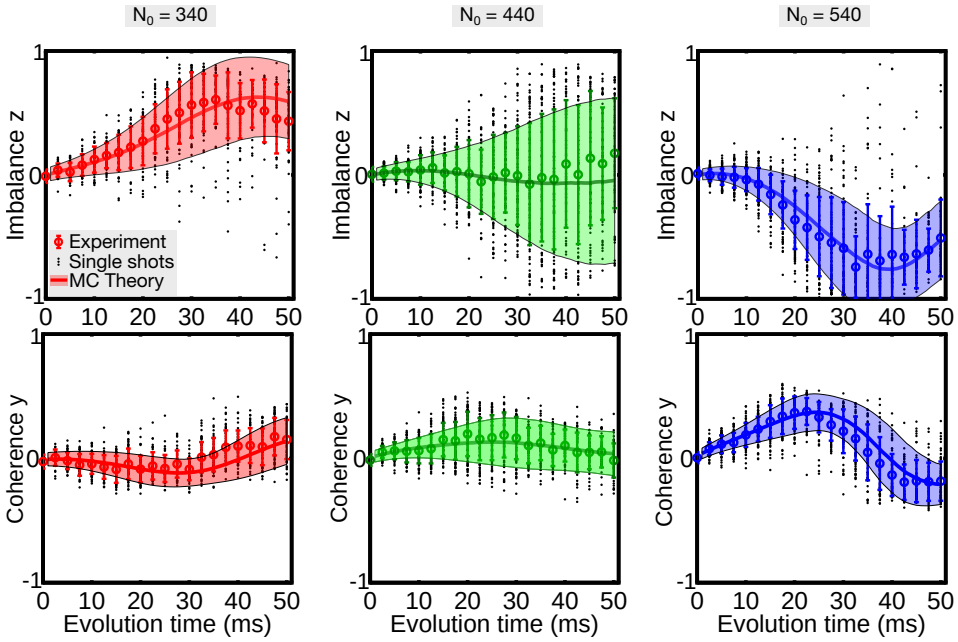


Figure 5.4.: **Quantum evolution on an unstable fixed point in the experiment.** The experimentally obtained time evolutions of $z$ (upper row) and the conjugate variable $y = \sin(\phi)$ (bottom) show a strong dependence on atom number due to the difference in collisional shift. This is shown with the single shots (black dots) as well as the mean and standard deviation of the distribution for each time step (colored circles and error bars). For an initial atom number $N_0 = 340$ (left panel), the state evolves around the upper stable fixed point, as $\delta > 0$. For the case of $N_0 = 440$ (center), which is on average 'resonant' during the evolution time, the mean population imbalance does not change, but the instability manifests itself in a fast spread of the quantum fluctuations. For even larger atom numbers ($N_0 = 540$, right panel), $\delta$ is negative and the state evolves around the lower fixed point. These experimental results are well reproduced by a Monte Carlo simulation using the experimental parameters (solid line and shaded uncertainty area). Note that in the experimental analysis, atom loss on the timescale of 110 ms was included in the postselection on atom number.

the phase of the Rabi coupling by $3\pi/2$ and attenuating the power by 24.8 dB to enter the bifurcated regime. Subsequently, we let quantum state evolve for different evolution times $t_{\text{evo}}$ and read out the complementary variables $z$ or $y = \sin(\phi)$, which is obtained from a final tomography rotation with angle $\alpha = 90°$. The frequency of the coupling radiation is carefully adjusted to resonance, canceling the light shifts and the collisional shifts for a certain atom number. Nevertheless, the parameter dependence of detuning and nonlinear interaction requires a postselection of the data on the total number of atoms.

The results of this procedure are depicted in Fig. 5.4 and show the strong atom number

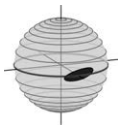

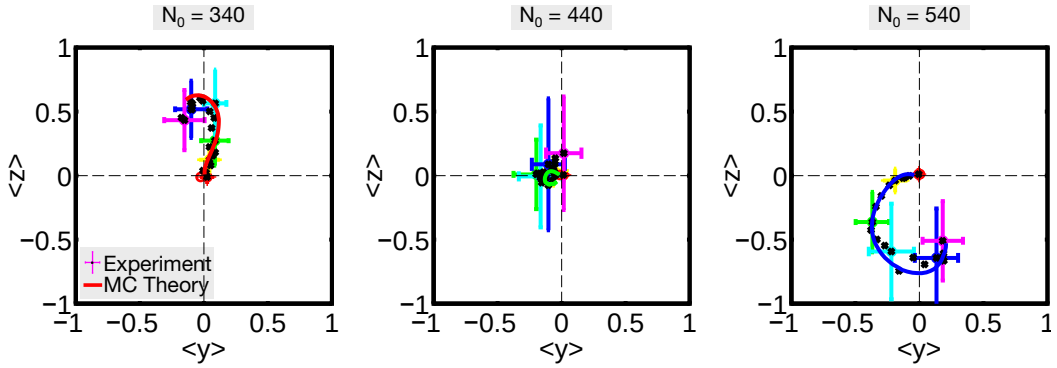


Figure 5.5.: **Expectation values for the temporal evolution on the unstable fixed point with different $N_0$.** The three panels depict the temporal evolution of the expectation values $\langle z \rangle$ and $\langle y \rangle$ for the evolution times $t_{\text{evo}} = 0, 2.5, ..., 50$ ms and initial atom numbers of $N_0 = 340$ atoms (left panel), $N_0 = 440$ (middle) and $N_0 = 540$ (right panel) observed in the experiment (black crosses). The postselection on atom number was adjusted with time according to the loss rate, corresponding to a fixed initial atom number $N_0$. The error bars depict the 1 s.d. width of the state after 0,10,...,50 ms, showing that the state eventually spreads over a large region in phase space. The temporal evolution of the expectation values closely resembles the trajectories of the classical mean-field description for $\delta > 0$ (left panel), $\delta \approx 0$ (middle) and $\delta < 0$ right panel. For the detuned cases, the state is not prepared exactly on the unstable fixed point and thus performs oscillations around the energetically lower lying stable fixed point. The results of Monte Carlo simulations using the experimental parameters show good agreement with the experimental data (solid colored lines).

dependence for the quantum evolution of the state. No change in the mean population is observed for an initial atom number of $N_0 = 440$ atoms, whereas the state oscillates around the upper stable fixed point for lower atom number (shown for $N_0 = 340$), and around the lower fixed point for larger numbers ($N_0 = 540$). We find the strong spreading of the fluctuations that is characteristic for the unstable fixed point. In the approximately resonant situation without temporal change in the mean population imbalance ($N_0 = 440$), we observe deviations from a Gaussian probability distribution for longer evolution times, where, as expected from the simple double well picture, the measurements of $z$ tend to accumulate near the classical turning points of the potential.

For a deeper understanding, we have to keep in mind that the atom number changes during the evolution due to the inherent loss processes. This is accounted for by changing the postselected atom number according to the independently determined loss rates (section 3.4). However, the consequential significant change of the parameters due to the altered atom number is visible in a slight variation of the phase even for the resonant case, which is only resonant on average during the observed time evolution.

These results are in good agreement with numerical simulations using the experimental pa-



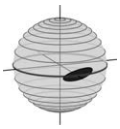

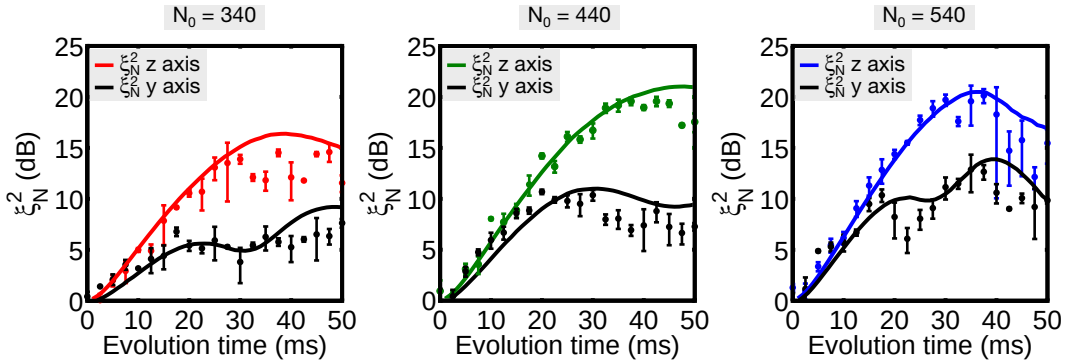


Figure 5.6.: **Variance in z and y direction for the quantum evolution on the unstable fixed point.** The variance in both conjugate variables $z$ and $y = \sin(\phi)$, quantified using the number squeezing parameter $\xi_N^2$, exhibits strong initial growth due to the preparation on the unstable fixed point. This is depicted for three different initial atom numbers with $\delta > 0$ (340 atoms, left panel), $\delta \approx 0$ (440 atoms, central panel), and $\delta < 0$ (540 atoms, right panel). As expected from the shape of the classical phase space, the spread in $z$ direction (color) grows faster than in the conjugate variable (black), as the trajectories of the separatrix are stretched towards the z direction. We find good agreement with a theoretical description based on Monte Carlo simulations using the experimental parameters (solid lines).

rameters and taking into account the loss processes, based on a Monte Carlo wave function approach [106, 107]. These simulations assume a square root dependence for the mean field detuning ($\delta_{\mathrm{MFS}} = -2\pi \times 0.63\sqrt{N}\,\mathrm{Hz}$) and the strength of the nonlinearity, which was modeled with $N\chi = 2\pi \times 30\,\mathrm{Hz}$ for 500 atoms. The coupling strength was assumed to be $\Omega = 2\pi \times 18\,\mathrm{Hz}$. In Fig. 5.4, the resulting mean and standard deviation of the calculated distribution functions in the population imbalance $z$ and the coherence $y$ are shown as a solid line and shaded area and yield a good description of the experimentally obtained values (error bars).

For the time evolution of the corresponding mean values $\langle z \rangle$ and $\langle y \rangle$ of the experimental data, we find that the quantum states indeed follow the familiar pattern known from the corresponding classical phase space, in good agreement with the results of the numerical simulations. For the detuned case with $\delta > 0\,(N_0 = 340\,\mathrm{atoms})$, we find that the expectation values of both variables oscillate around a fixed point above the equator, whereas a fixed point below the equator is enclosed in the case of $\delta < 0\,(N_0 = 540\,\mathrm{atoms})$.
A quantitative analysis of the variance in $z$ and $y$ direction shows an increase in both directions (Fig. 5.6). Initially, this is caused by the rapid expansion of the quantum uncertainty of the initial state on the unstable fixed point due to the corresponding expulsive potential. For the later part of the time evolution, the subsequent bending around the stable fixed points leads to an accumulation of the density beyond these fixed points, which further increases the variance. We find that the variance along the $z$ direction increases faster, as expected from the shape of the separatrix in the classical phase space, which is stretched in $z$ direction. This is also

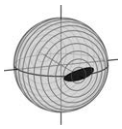

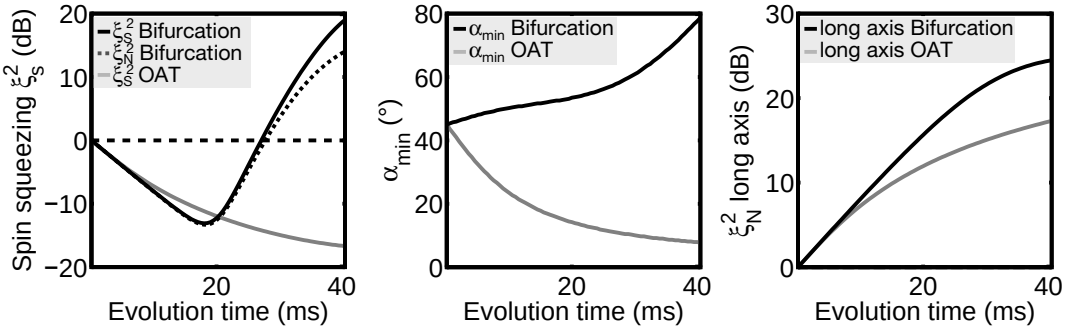


Figure 5.7.: **Squeezing in the ideal theoretical evolution on the unstable fixed point.** For the ideal temporal evolution of spin squeezing using the bifurcation squeezing scheme (solid black line, left panel) with typical experimental parameters ($N = 500$, $N\chi = 2\pi \times 30\,\mathrm{Hz}$, $\Omega = 2\pi \times 18\,\mathrm{Hz}$, $\delta = 0\,\mathrm{Hz}$), we find faster initial squeezing compared to the corresponding evolution in the one-axis twisting scenario (gray solid line). Optimal squeezing in the bifurcation scheme yields $\xi_S^2 = -13.1\,\mathrm{dB}$ after 18 ms. Both minimal number squeezing (dotted black line) and spin squeezing subsequently vanish due to the bending of the state around the stable fixed points. We expect to find both a larger optimal rotation angle $\alpha_{\mathrm{min}}$ (middle panel) and stronger elongation of the long axis (right panel) in comparison to the one-axis twisting scheme.

reproduced by the Monte Carlo simulations of the system, where detuning fluctuations due to technical noise are also included. To attain quantitative agreement with the experimental data, detuning fluctuations on the order of $\sigma_\delta = 2\pi \times 0.45\,\mathrm{Hz}$ are assumed, which is the typical amplitude of the fluctuations over the course of several days.
The fast initial spreading of the quantum uncertainty points at a squeezed axis of reduced fluctuations at an intermediate angle. To investigate these squeezing properties, we thus have to perform a tomographic analysis in order to find the axis of minimal fluctuations.

## 5.3. Bifurcation Squeezing: Generating Squeezed States on an Instability

For the previously measured corresponding conjugate variables $z$ and $y$, we could observe an increase of fluctuations with evolution time. We now have to find the axis of minimal uncertainty with a tomographic analysis.

We first investigate the spin squeezing that can be theoretically obtained in the idealized time evolution, assuming a resonant evolution with our typical experimental parameters (atom number $N = 500$, nonlinearity $N\chi = 2\pi \times 30\,\mathrm{Hz}$, coupling strength of $\Omega = 2\pi \times 18\,\mathrm{Hz}$) and neglecting loss and technical noise contributions. Compared to the one-axis twisting scheme, we find a faster squeezing rate in the early stages of the time evolution. An optimal value of



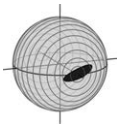

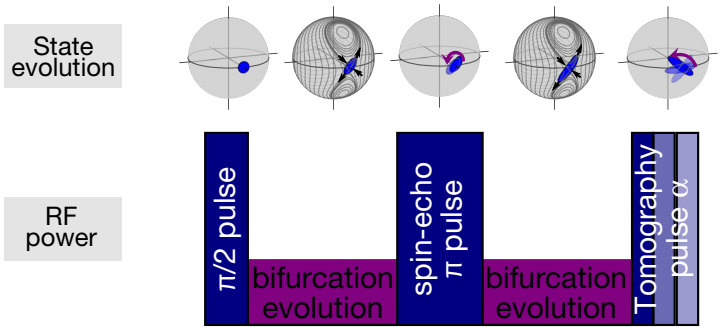


Figure 5.8.: **Experimental pulse sequence for bifurcation squeezing.** For the implementation of a squeezing scheme on the unstable fixed point in the bifurcated regime, we first prepare an equal superposition of both components by use of a two-photon $\pi/2$ pulse, as in the one-axis twisting scenario. We subsequently attenuate the radio frequency as well as the microwave coupling by a combined 24.8 dB to reach $\Omega = 2\pi \times 18\,\mathrm{Hz}$ and switch the coupling phase to $\phi = 3\pi/2$. With this, we enter the bifurcated regime and prepare our initial state on the unstable fixed point of the corresponding classical phase space. After half of the evolution time, we perform a high-power spin-echo $\pi$ pulse around $\phi = 3\pi/2$ to reduce the influence of detuning fluctuations. We then again attenuate the two-photon coupling to perform a second period of bifurcated evolution, and finally rotate the state around itself with readout pulse ($\phi = 3\pi/2$ for $-180° < \alpha < 0°$ and $\phi = \pi/2$ for $0 < \alpha < 180°$).

$\xi_S^2 = -13.1\,\mathrm{dB}$ should ideally be attainable after 18 ms, as shown in Fig. 5.7. Afterwards, squeezing rapidly vanishes and the optimal tomography angle increases due to the bending of the state around the stable fixed point.

Experimentally, we implement the tomographic analysis by use of a variable readout pulse in analogy to the one-axis twisting sequence described in section 4.2.3. We also add an analogous spin-echo scheme to reduce the susceptibility of the dynamics to technical detuning fluctuations. This is necessary due to the observed strong sensitivity of the dynamics on detuning, which was shown in the previous section. Recall that the detuning jitter caused by the finite magnetic field stability corresponds to fluctuations on the order of hundreds of millihertz, whereas for the experimentally required Rabi frequency below 20 Hz the dynamics show a distinct change already for detunings on the order of 1 Hz (Fig. 5.3).
The experimental implementation of the bifurcation squeezing scheme thus follows the same route as the previously shown measurements of the temporal evolution of $z$ and $y$, with the addition of the spin-echo pulse with $\Omega = 2\pi \times 310\,\mathrm{Hz}$ at half the evolution time with a phase of $\phi = 3\pi/2$, and a variable tomography pulse around $\phi = 3\pi/2$ for $-180° < \alpha < 0$ and $\phi = \pi/2$ for $0 < \alpha < 180°$. The corresponding experimental pulse sequence is depicted in Fig. 5.8.
The resulting temporal evolution of the squeezing parameter $\xi_S^2$ for an initial state with atom

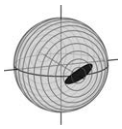

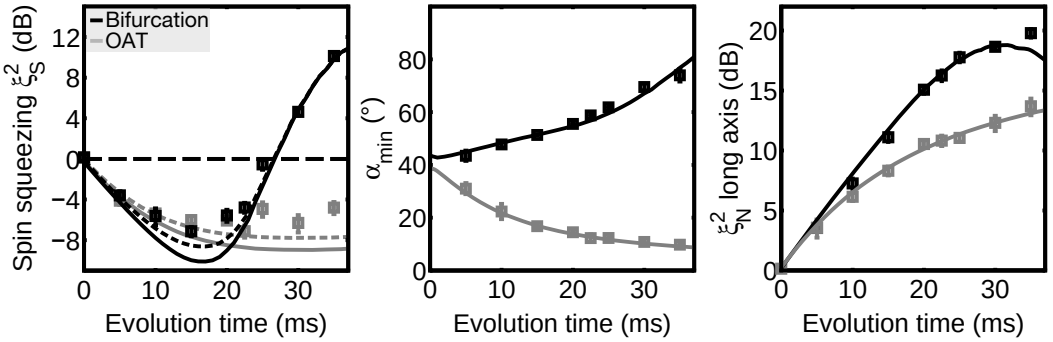


Figure 5.9.: **Temporal evolution of bifurcation squeezing for $\mathbf{N_0 = 500}$ atoms.** The resulting states of the bifurcation squeezing scenario (black error bars) with different evolution times are characterized via the obtained spin squeezing parameter $\xi_S^2$ (left panel), the optimal tomography angle $\alpha_{\text{min}}$ (middle panel) and the extension of the long axis (right panel). The corresponding data for the one-axis twisting scheme is shown for comparison (gray error bars). We experimentally find that with the bifurcation scheme, spin squeezing quickly builds up in the initial evolution, and reaches $\xi_S^2 = -7.1(3)\,\text{dB}$ after $t_{\text{evo}} = 15\,\text{ms}$. After this optimal time, the effects of the bending around the stable fixed points become visible both in the loss of spin squeezing and the increase in optimal rotation angle. The strong increase in the size along the long axis emphasizes the instability that drives this process. The results show good agreement with a Monte Carlo simulation for the experimental parameters (black solid lines for bifurcation, gray solid lines for one-axis twisting). The dashed lines in the left panel indicate the theoretical squeezing values including additional noise sources during the detection process.

number $N_0 = 500 \pm 15$ atoms is shown in Fig. 5.9. In analogy to the evaluation of the one-axis twisting evolution, the decay time of $\tau \approx 110\,\text{ms}$ is taken into account in the postselection process. We find, as expected, strong initial spin squeezing, quantified by a fast decrease of the spin squeezing parameter $\xi_S^2$. After an evolution time of $t_{\text{evo}} \approx 15\,\text{ms}$, the best squeezing of $\xi_S^2 = -7.1(5)\,\text{dB}$ is found for an optimal tomography angle of $\alpha_{\text{min}} = 55°$. Without subtraction of detection noise, this corresponds to a bare spin squeezing value of $\xi_S^2 = -4.5(2)\,\text{dB}$. As theoretically predicted, the squeezing rate of the bifurcation squeezing scenario is slightly faster than in the one-axis twisting case. This can also be seen from the stronger growth of the state's extension along its long axis.

After this optimal time, spin squeezing rapidly vanishes, which is caused by the fact that the variance of the state grows in all directions as it bends around the stable fixed points of the classical phase space. This also results in the build-up of higher order moments in the corresponding experimental probability distributions which are not detected in the squeezing parameters. The absence of spin squeezing does not mean that these states are not entangled, as a variance analysis can not fully characterize such non-Gaussian states. Indeed, an experimental extraction of the Fisher information for these states, which builds on the full distribution



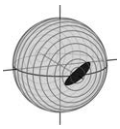

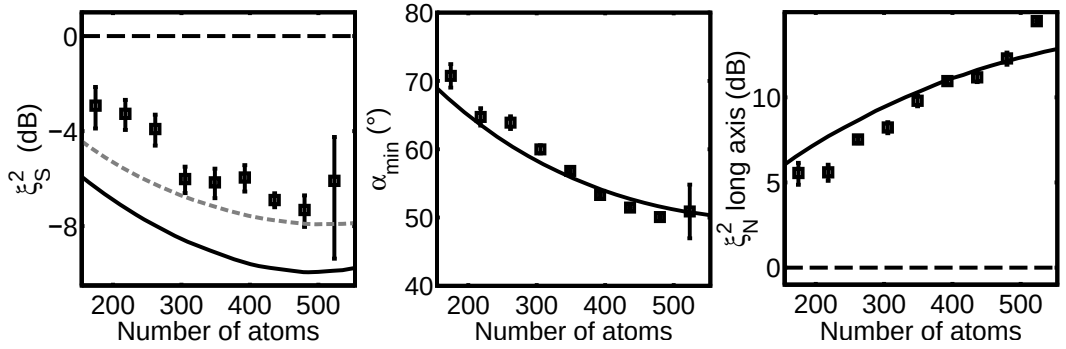


Figure 5.10.: **Atom number dependence of states generated after 15 ms of bifurcation squeezing.** Due to the dependence of both interaction strength $\chi$ and detuning $\delta$ on atom number, the properties of the generated states strongly depend on $N$. We find that spin squeezing, parametrized by $\xi_S^2$, improves for larger atom number (left panel) and shows a stronger dependence than the corresponding states generated by one-axis twisting. The decrease of the optimal angle $\alpha_{\text{min}}$ for larger $N$ (middle panel) can be understood from the fact that the separatrix gets less steep for larger values of $\Lambda$ (see e.g. Fig. 2.3). The long axis of the state grows with increasing atom number, as the nonlinearity increases and the process becomes more resonant (right panel). The solid black lines are the results of Monte Carlo simulations of the applied spin-echo sequence employing the experimental parameters and assuming $N\chi \propto \sqrt{N}$ and $\delta_{\text{MFS}} \propto \sqrt{N}$, the dashed gray line in the left panel also takes into account known additional noise sources during the detection process.

functions and thus also takes the higher moments into account, shows that entanglement also exists at the time when squeezing has vanished [61].

Comparing the generated squeezed states in the early time evolution of the bifurcation squeezing scheme with the ones obtained from the one-axis twisting scenario, we observe larger optimal tomography angles $\alpha_{\text{min}}$, and thus the generation of states which are closer to the phase squeezed situation. The angle of optimal squeezing $\alpha_{\text{min}}$ increases with time, which can be attributed to the bending of the state around the fixed points.
The experimental results are in good agreement with Monte Carlo simulations of the full sequence including the spin-echo pulse and the time dependence of the parameters (solid lines in Fig. 5.9), which were obtained for the corresponding experimental values for nonlinearity and coupling strength, including the atom number dependence of $\chi$ and $\delta$ and detuning fluctuations of $\sigma_\delta = 2\pi \times 0.45\,\text{Hz}$. As in the one-axis twisting scenario, the squeezing values that are predicted from the simulation are significantly lower than what is experimentally observed. The inclusion of known additional noise sources during the detection process as described in section 4.2.3 yields better agreement (dashed lines in Fig. 5.9).

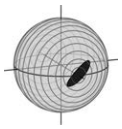

We now turn to a detailed analysis of the resulting squeezed states created by our spin-echo scheme for the optimal evolution time of $t_{\text{evo}} = 15\,\text{ms}$, and study the atom number dependence of these states. The experimental results show that spin squeezing $\xi_S^2$ improves for larger atom number, but has a stronger dependence over the whole range of atom numbers compared to the corresponding states generated by one-axis twisting (Fig. 5.10). The improvement at larger numbers is caused by the stronger nonlinearity, which leads to a larger expulsion in the early time evolution. Also, for these measurements, the resonance condition was shifted to higher initial atom numbers, which results in better squeezing for states with larger $N$.
Similarly, a stronger dependence is found for the optimal tomography angle $\alpha_{\text{min}}$, which decreases with increasing atom number. This angle is determined by the steepness of the separatrix, which decreases for larger values of $\Lambda$ when the stable fixed points are moving further apart (see Fig. 2.3). The long axis of the state also shows a strong dependence on $N$. Similarly to the spin squeezing parameter, the growth with increasing atom number is caused by the larger nonlinearity and the fact that the process becomes more resonant for higher atom numbers.

In conclusion, these results demonstrate that spin squeezed states can be generated in the early stages of the quantum dynamics in such a bifurcated system. The criticality of the dynamics on the employed parameters manifests itself in a stronger dependence of the final states on atom number in comparison to the one-axis twisting scenario. Still, due to the large amount of attainable squeezing, also with this new dynamical scheme the creation of simultaneous squeezing in all lattice sites seems feasible. We will investigate the scalability for these states in the following chapter.



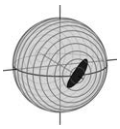

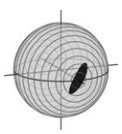

# 6. Scaling Squeezed States to Large Atom Numbers

The best attainable sensitivity for phase estimation in an interferometer employing a spin squeezed input state of $N$ particles is given by $\Delta\theta = \xi_{\mathrm{R}}/\sqrt{N}$ [101], where $\xi_{\mathrm{R}}$ is the metrological spin squeezing parameter. In principle, this opens two possible pathways for improving the measurement precision. One option would be further reducing the squeezing parameter. Given the inherent loss during the generation of the quantum correlations, this route seems improbable, as these processes limit the attainable spin squeezing above the values that can be obtained in principle. Thus, for high-performance interferometry, input states with large atom number are required. In Bose-Einstein condensates, however, the production of squeezed ensembles has been limited to small particle numbers below 2500 atoms. In this chapter, we will explain the obstacles which have limited the attainable atom numbers so far. Subsequently, a scalable method for the creation of macroscopic squeezed states will be presented, which builds on an array of individually squeezed small condensates and thus circumvents these issues. We will analyze the characteristic scaling behavior, the influence of classical noise sources, and implement the differential analysis method explained in section 4.1.4. This analysis is insensitive to the technical fluctuations and thus gives direct access to the quantum uncertainties of the generated states. The results presented in this chapter are also summarized in a publication [60].

## 6.1. Squeezing with Large Atom Numbers in BECs

In interferometry, the attainable precision is directly connected to the distinguishability of two different phase settings in a measurement. For Gaussian states, this distinguishability can be quantified in terms of the uncertainty of a phase measurement, which is given by $\Delta\theta = \xi_{\mathrm{R}}/\sqrt{N}$ (see section 7.1). Thus, for constant $\xi_{\mathrm{R}}$, the phase uncertainty can always be reduced by increasing the atom number of the input state. This in turn means that in practice, it is only reasonable to generate squeezing if the number of usable particles is limited.
Such limitations can be given from the requirement of high spatial resolution and a simultaneous upper bound on density [48], low temperatures, or by other technical constraints that limit the attainable particle number (e.g. three-body loss as an upper limit for the condensate size [110]). To enable a sensitivity improvement in high-precision measurements, it is thus desirable to generate squeezed states whose atom numbers reach this obtainable size of the classical sources.
Bose-Einstein condensates have particularly attractive properties for interferometric measurements, such as their long coherence times and the ultralow temperatures. These are prereq-

uisites for some of the most intriguing applications in atom interferometry, such as high-precision measurements of the gravitational constants, gravitational wave detection and tests of the weak equivalence principle [111, 112]. Interrogation times on the order of one second have been achieved in microgravity [43], necessitating temperatures in the range of hundreds of picokelvin to limit the spread of the cloud at the end of the interferometric sequence. Similar situations are found in atomic fountains, where interrogation times of up to $2.3\,\mathrm{s}$ have been achieved [113]. Additionally, applications that require high spatial resolution, such as magnetic field microscopy [114], favor ultracold samples, for which the timescale of diffusion is longer than in thermal clouds.

For thermal atomic clouds, efficient production of large spin squeezed ensembles has been performed based on atom-light-interaction. Conditional spin squeezing of up to $-10\,\mathrm{dB}$ has been attained for atom numbers ranging up to $10^6$ atoms by use of quantum-non-demolition measurement techniques [34, 35, 36, 37, 38]. A cavity squeezing technique also allowed for the generation of unconditional spin squeezed states with a metrologically relevant noise reduction of $\xi_\mathrm{R}^2 = 5.6(6)\,\mathrm{dB}$ for $5 \times 10^4$ cold thermal atoms [39].

In contrast to these experiments with thermal atoms, in Bose-Einstein condensates those schemes relying on atom-light interaction have not been successfully implemented so far. However, it has been theoretically proposed [44] and experimentally demonstrated that spin squeezed states can be generated with schemes that are based on interatomic interaction [5, 46, 45, 47]. In terms of scalability with atom number, all techniques that rely on atomic scattering suffer from similar difficulties, as the obtainable nonlinearities are small compared to the interactions between atoms and light fields. The typical size of the attainable interatomic nonlinearities is on the order of tens of Hertz. This implies that the generation times for entangled states are in the range of tens of milliseconds, which is on the same order as the typical timescales for loss or external dynamics of the atomic clouds. Raising the atom number means either increasing the density or the trap volume, or both. Due to the emerging spurious effects of spatial dynamics or atomic loss, this implicates that both routes lead to severe constraints on the accessible atom numbers and squeezing factors.

In the case of higher densities, loss will not only eventually limit the total atom number, but also destroy the coherence that is a prerequisite for high-performance measurements. Note that for spin squeezing of internal states, the requirement of magnetic insensitivity during state generation implicates the use of a system with an excited state that is subject to spin relaxation loss. This implies that loss is present even in the absence of a Feshbach resonance (see section 3.4).

In the absence of losses, the best squeezing is shown to scale as $\xi_\mathrm{opt}^2 \propto N^{-2/5}$ [25, 28]. This is strongly modified if atomic loss processes take place during state generation. Such processes typically have a strong dependence on the number of particles in the cloud. In the Thomas-Fermi approximation, the chemical potential scales as $\mu \propto N^{2/5}$, and the corresponding wave function is given by $\phi(\mathbf{r}) \propto \sqrt{\mu - V(\mathbf{r})}$. Thus, for harmonic traps, the strength of the nonlinear interaction has a proportionality of $\chi \propto N^{-3/5}$, leading to a scaling of the combined nonlinearity of $N\chi \propto N^{2/5}$. The loss rate for two-body processes is expected to have a similar proportionality $\Gamma_2 \propto N^{2/5}$ in the Thomas-Fermi regime, but the three-body loss rate scales as $\Gamma_3 \propto N^{4/5}$ and thus increases faster than the nonlinear interaction [28]. With a combined loss

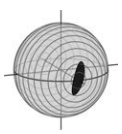

rate $\Gamma = \sum_m m\Gamma_m$, with $m$ indicating the number of particles lost in each process, it can be shown analytically [28] that the presence of atom loss alters the time evolution of squeezing as

$$\xi^2(t) = \xi_0^2(t)\left[1 + \frac{\Gamma t}{3\xi_0^2(t)}\right], \tag{6.1}$$

where $\xi_0^2(t)$ is the squeezing in the no-loss case. This demonstrates the sensitivity of the obtainable squeezing on the losses, which can lead to significant degradation depending on the loss rate and the amount of squeezing. For three-body loss, which appears to be the dominant loss process in our system (see section 3.4), it can be shown that spin squeezing degrades for large atom number even without additional noise sources [28].

If the trap sizes is increased by lowering the trap frequencies, higher spatial modes of the condensate will eventually be populated. Such a multi-mode situation completely alters the behavior in comparison to a two-mode system. It puts lower bounds on the best achievable squeezing due to random dephasing introduced by the non-condensed quasi-particles, as shown by *Sinatra et al.* [58, 115]. These theoretical works suggest that squeezing for large systems should still be attainable, but is distinctly degraded compared to the two-mode scenario.

Additional problems occur due to the varying squeezing rates of the different modes and complex nonlinear coupling between the spatial modes of the trapped condensates. This can disturb mode-matching and mix fields with different phase evolution, which can lead to rapid loss of squeezing [59]. Additionally, the degraded mode-matching during the final readout pulse leads to a deteriorated conversion of quadrature squeezing into number squeezing. *Johnsson et al.* [59] state that these effects could be minimized for extremely weak trapping, which is experimentally challenging. Generally, from an experimental perspective, ensuring the reproducibility of a system with multiple external modes is a hard task and requires a high level of control over the technical parameters of the system. In our setup, attempts to generate squeezing in a multi-mode BEC of $10^4$ atoms were only able to show that fluctuations along one spin direction increased, but suppression of fluctuations below the classical limit could not be detected.

In this chapter, we examine an alternative approach for scaling up the number of particles that evades these limitations. The basic idea is to use an optical lattice to generate many identical copies of the well-controlled situation in the single lattice sites. We tune the potential height of the lattice such that tunneling is negligible on the timescale of the experiments and thus realize a system of many independent replica. Combining all the individually squeezed ensembles realizes a controlled multi-mode scenario where nevertheless coupling to higher spatial modes does not take place, and allows increasing the particle number without changing the mean density of the cloud. Under the assumption that the parameters of the system are homogeneous over the extension of the array, this should allow the generation of squeezed states with macroscopic particle numbers. In the following sections, we will examine experimental results following this route and show that this provides a viable pathway for the well-controlled generation of squeezed states with large particle numbers.



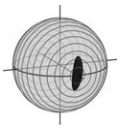

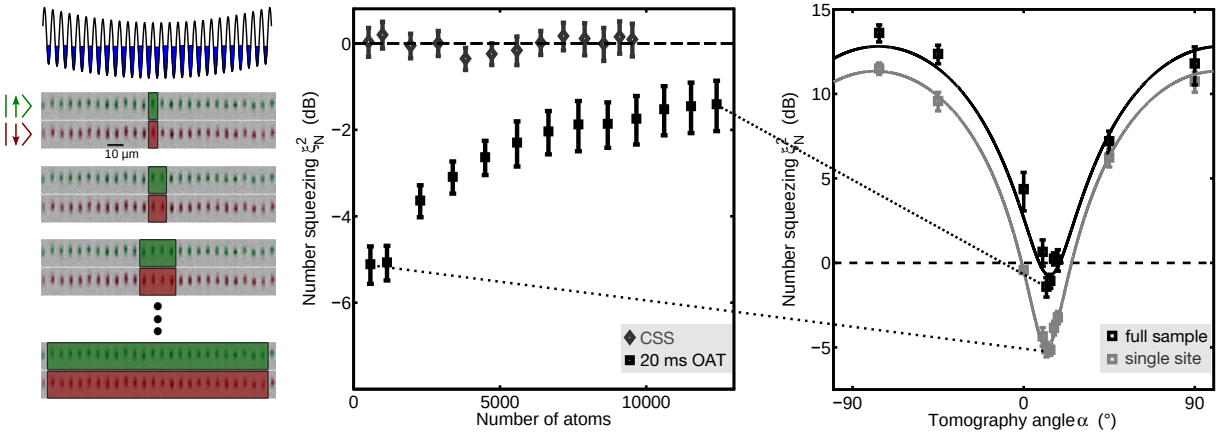


Figure 6.1.: **Scalability of number squeezing obtained from one-axis twisting.** We investigate the scalability of number squeezing to large particle numbers by summing up more and more adjacent lattice sites of our 1D lattice (left panel). For the state generated after 20 ms of one-axis twisting evolution using a spin-echo sequence, we still observe number squeezing for 12 300 particles at the optimal rotation angle, but degradation with growing atom number (middle panel). We do not observe such effects for the classical reference (coherent spin state, open gray diamonds), indicating that technical phase fluctuations during the state generation cause the deterioration. A tomographic analysis reveals that the fluctuations of the squeezed state are increased for all tomography angles (right panel, black squares for 12 300 particles) compared to the ones for single lattice sites (gray squares). The solid lines are sinusoidal fits to the experimental data, the dashed lines indicate the classical limit.

## 6.2. Scalability of Squeezing: A Direct Analysis

To investigate if the squeezing obtained with the single lattice sites also translates into suppressed fluctuations of the sum over the full array, we first perform a direct analysis of $\xi^2_{\mathrm{N}}$, which is done by quantifying the fluctuations of repeated measurements.

We can gain knowledge on the scaling behavior by evaluating the number squeezing $\xi^2_{\mathrm{N}}$ for growing sample size. We implement this starting with a single lattice site that contains $N_i^a$ atoms in state $|a\rangle$ and $N_i^b$ atoms in state $|b\rangle$. For this site, we calculate the number squeezing from the observed fluctuations of $z_1 = \left(N_i^b - N_i^a\right) / \left(N_i^b + N_i^a\right)$. Subsequently, we sum the atom numbers of more and more adjacent sites. For the sum over $n$ sites, we obtain $z_n = \left(\sum_{j=1}^n N_j^b - \sum_{j=1}^n N_j^a\right) / \left(\sum_{j=1}^n N_j^b + \sum_{j=1}^n N_j^a\right)$ and analyze the corresponding squeezing factor for each sample size.

We first examine the data obtained after 20 ms of one-axis twisting with a spin-echo pulse in the middle of the time evolution, as this scenario yields optimal performance for the single lattice sites. We carry out the analysis procedure as described above, starting with a single lattice site in the center of the cloud, then adding more and more adjacent sites, and even-

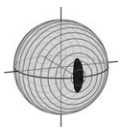

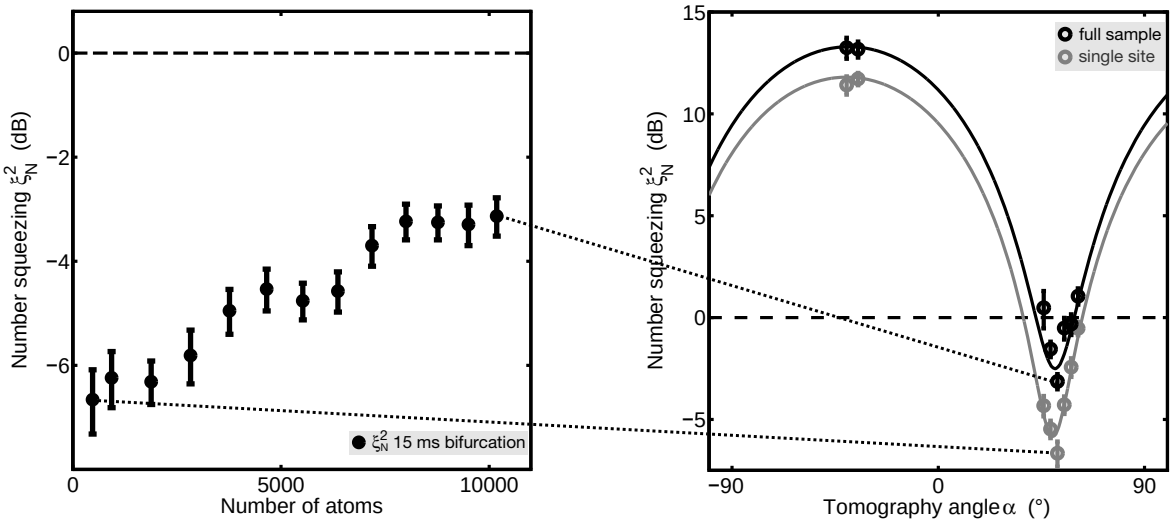


Figure 6.2.: **Scalability of number squeezing in the bifurcation squeezing scenario.** Similarly to the states generated by one-axis twisting, we observe decreasing number squeezing $\xi^2_{\mathrm{N}}$ with growing atom number for the state generated after 15 ms of bifurcation squeezing (left panel). However, the scaling is more favorable and still yields $\xi^2_{\mathrm{N}} = -3.3(4)$ dB for 10 200 atoms. Similarly to the one-axis twisting scheme, the tomographic analysis shows growing fluctuations in all directions (right panel, gray points for single wells and black data for the sum over all sites).

tually summing up to 24 lattice sites. Analyzing the corresponding number squeezing $\xi^2_{\mathrm{N}}$ (Eq. 4.7), we find a significantly degraded suppression of fluctuations with growing sample size. Figure 6.1 depicts this scaling behavior for a final tomography rotation of $\alpha = 12°$, which corresponds to the angle of best squeezing both for the single lattice sites and the full ensemble. Tomographic comparison between the squeezing in single lattice sites and the full summed ensemble (12 300 atoms) shows that the observed fluctuations grow for all investigated tomography angles. However, for a classical coherent spin state, which is obtained by implementing a resonant $\pi/2$ pulse using two-photon coupling, we do not observe additional fluctuations. This points at the presence of common mode fluctuations during the nonlinear evolution that mask the quantum uncertainty of the squeezed state for larger particle numbers. We will show in section 6.3 that this is indeed the case.
Even with these additional fluctuations, we still observe a reduced variance of the population imbalance for 12 300 atoms, which is suppressed by $\xi^2_{\mathrm{N}} = -1.5(6)$ dB. It has to be noted that the photon shot noise contribution from the imaging process, which in these measurements corresponds to approximately $10\%$ of the projection noise of a corresponding coherent spin state, has been subtracted for all squeezing results presented in this chapter.

We find qualitatively similar behavior for the scalability of states generated by the bifurcation squeezing scheme. Figure 6.2 shows the results obtained after an evolution time of 15 ms with a spin-echo sequence. Compared to the one-axis twisting scenario, we find a more favorable scaling at the optimal tomography angle (52°), leading to number squeezing



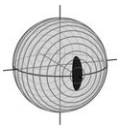

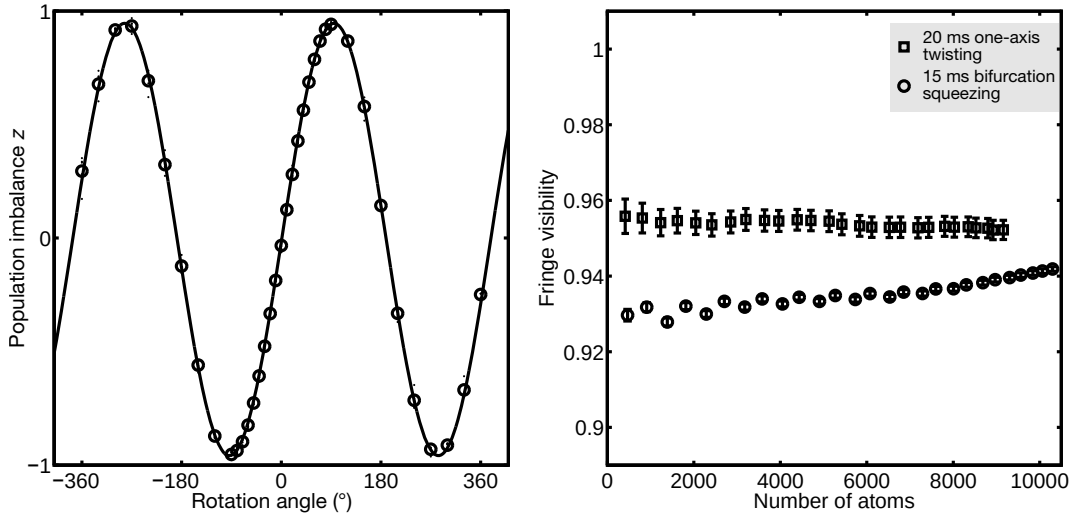


Figure 6.3.: **Scaling of the visibility $\mathcal{V}$ with ensemble size.** Rabi flopping with the squeezed state of the full ensemble of $10^4$ particles still yields high visibility (left panel). We find $\mathcal{V} = 0.952(3)$ after 20 ms of one-axis twisting and $\mathcal{V} = 0.942(1)$ after 15 ms of bifurcation squeezing and almost constant values for all ensemble sizes (right panel). The slight tendency to increasing $\mathcal{V}$ for the bifurcation scenario (circles) is due to the atom number inhomogeneity. For the central lattice sites, the larger mean atom number leads to a shorter mean spin length compared to the lower numbers at the edge of the cloud, which causes an effective increase in $\mathcal{V}$ when summing also over lattice sites far from the center. This is not visible for the one-axis twisting scenario (squares), where the squeezing dynamics and the extension of the long axis are less critical on atom number.

of $\xi_{\mathrm{N}}^2 = -3.3(4)$ dB for the full sample of 10 200 atoms. As in the one-axis twisting case, a tomographic comparison between the single lattice sites and the full sample shows that fluctuations increase in all directions. The better scaling at the optimal rotation angle can be explained by a more favorable geometry of the technical fluctuations, as will be shown in section 6.3.

The corresponding spin squeezing parameter for the summed ensemble can be obtained using the Wineland criterion (Eq. 4.10). To do so, we perform resonant Rabi flopping with the final state and deduce the visibility $\mathcal{V}$ from a fit of the oscillation amplitude. Here, the resonance condition is ensured using Ramsey spectroscopy on the same transition.
To analyze the scaling of the visibility with growing sample size, we sum more and more adjacent sites in analogy to the number squeezing analysis. We find almost constant visibility for all ensemble sizes, yielding $\mathcal{V} = 0.952(3)$ after 20 ms of one-axis twisting and $\mathcal{V} = 0.942(1)$ after 15 ms of bifurcation squeezing for the full ensemble (Fig. 6.3). This yields a combined spin squeezing of $\xi_{\mathrm{s}}^2 = -1.0(5)$ dB for 12 300 atoms in the one-axis twisting case, and $\xi_{\mathrm{s}}^2 = -2.8(4)$ dB for 10 200 atoms using bifurcation squeezing. An interesting aspect in

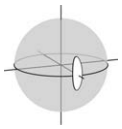

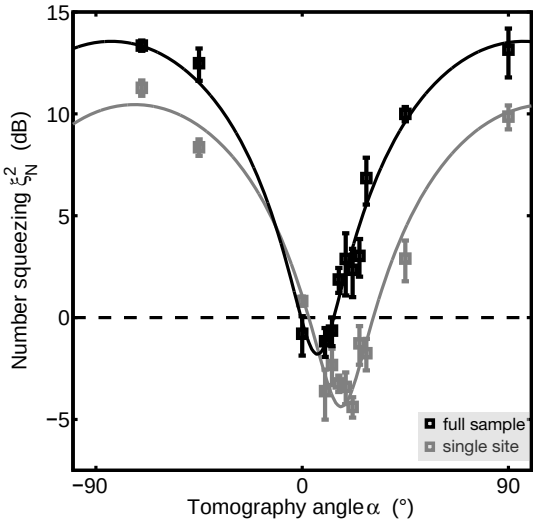


Figure 6.4.: **Squeezing at large atom number without spin-echo sequence.** After 15 ms of one-axis twisting without spin-echo pulse, the technical fluctuations dominate over the quantum uncertainty. This is showcased by a squeezing analysis of $\xi^2_{\mathrm{N}}$ versus tomography angle for a single lattice site (gray) and the full ensemble of $10^4$ particles (black). The strong influence of classical fluctuations becomes apparent in a shift of the axis with minimal fluctuations towards smaller tomography angles $\alpha$, as it is expected for strong phase fluctuations.

the calculation of the spin squeezing parameter is the fact that it cannot be obtained using $\langle\cos(\phi)\rangle$ as in the two-mode model. This is because in the summed ensemble, the atoms are no longer indistinguishable due to their spatial separation by the 1D lattice. Thus, we have realized a controlled multi-mode situation, and the system cannot be treated as being solely in two modes. Effectively, this leads to a reduced spin length, as the overall spin length is given by the sum of the spin vectors from the individual lattice sites – which are reduced from the elongation of the state during the squeezing process – and not by the sum of all individual spin-1/2 particles in the full ensemble.

For a deeper understanding of the scalability, we have to investigate the source and the impact of the additional fluctuations that limit the number squeezing at larger atom numbers. The importance of such fluctuations is demonstrated in Fig. 6.5, which depicts the upscaled number squeezing for a one-axis twisting sequence without spin-echo pulse. Here, classical fluctuations start to dominate over the quantum uncertainties, which becomes apparent in a shift of the optimal angle $\alpha_{\mathrm{min}}$ of the squeezing tomography for larger atom numbers. In the following section, we will analyze this behavior and its causes in detail.



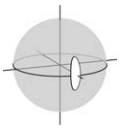

## 6.3. Assessing and Reducing Classical Noise During State Generation

In the previous section, we have examined the scalability of number squeezing with system size and found substantial deterioration of the performance with growing atom number. In this section, we will show that this is mainly caused by classical technical fluctuations that mask the quantum resources of the states at large atom numbers. We will examine the origin and the geometry of these classical fluctuations and investigate how they can be suppressed by use of a spin-echo technique. Understanding these mechanisms, we will find that an optimized spin-echo sequence can further reduce the sensitivity of the generation procedure to technical fluctuations.

### 6.3.1. Magnetic Field Stability: The Source for Classical Fluctuations

The finite stability of our magnetic bias field, which varies by $\sigma_B = 30\,\mu$G from shot to shot, induces classical fluctuations in our system. Specifically, the field fluctuations $\sigma_B$ enter in the one-axis twisting Hamiltonian Eq. 2.22 via the detuning $\delta$, which changes as

$$\sigma_\delta = 2\pi \mathcal{S}_{ab} \sigma_B, \tag{6.2}$$

where $\mathcal{S}_{ab}$ is the magnetic field sensitivity of the two-photon transition. Both levels $|a\rangle$ and $|b\rangle$ have the same linear Zeeman dependence, but the quadratic shift of 72 Hz/G$^2$ of the two levels is in opposite direction, leading to a linearized sensitivity of $\mathcal{S}_{2\gamma} \approx 10\,$kHz/G at the operating field of 9.12 G (see Appendix A ).
After a finite evolution time $t_{\text{evo}}$ with a detuning $\delta$, the state acquires a phase of $\phi = \delta t_{\text{evo}}$. Thus, the fluctuations of the magnetic offset field translate into a phase uncertainty

$$\sigma_\phi = 2\pi \mathcal{S}_{ab} t_{\text{evo}} \sigma_B. \tag{6.3}$$

For a $\pi/2$ pulse and subsequent nonlinear evolution, we consequently expect dephasing with an amplitude that is proportional to the evolution time. Specifically, for our long-term stability of $\sigma_B = 45\,\mu$G, which also includes slow drifts over the course of a weekend, we expect a classical phase uncertainty of $\sigma_\phi \approx 0.04$ radians for a typical nonlinear evolution time of 15 ms. This is equivalent to the quantum fluctuations of a coherent spin state with 550 atoms, and the dominant noise source for larger atom numbers, as the quantum noise scales as $1/\sqrt{N}$. Figure 6.5 shows that we indeed observe increased classical technical noise along the phase direction for a nonlinear evolution of 15 ms in a tomographic analysis. In the following, we will explain how these technical fluctuations can be quantified in the experiment.

The classical technical noise contribution can be characterized by taking advantage of our lattice system [62, 45]. For this analysis, we add up the atom numbers of the two components over more and more adjacent lattice sites and calculate the corresponding variance in the atom

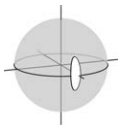

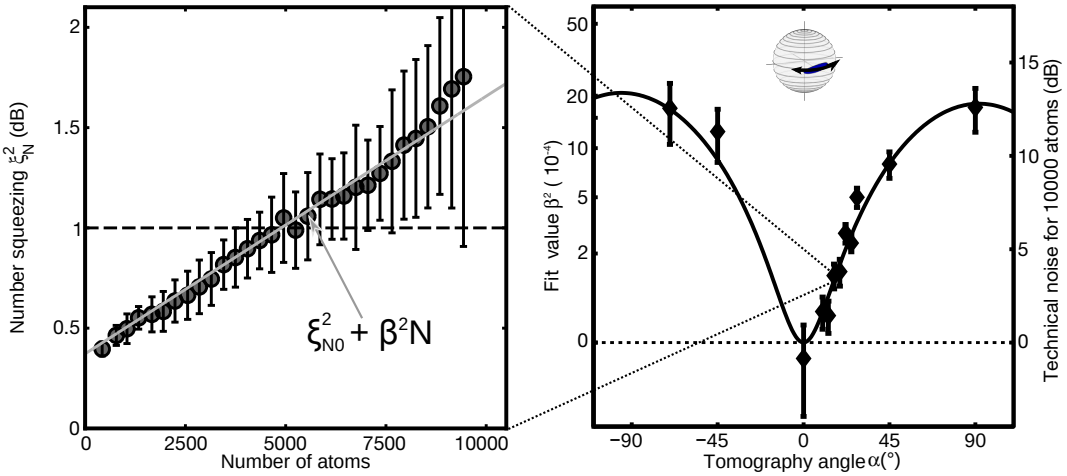


Figure 6.5.: **Classical fluctuations in the one-axis twisting scenario.** The strength of classical fluctuations for a specific tomography rotation can be quantified from a linear fit $f = \xi_{\mathrm{N}_0}^2 + \beta^2 N_{\mathrm{tot}}$ to the scaling of the averaged number squeezing $\xi_N^2$ with the total atom number $N_{\mathrm{tot}}$ (left panel). We obtain this by summing more and more adjacent lattice sites and averaging the results over the whole sample, which cancels atom number dependent effects due to different populations in the individual sites. A tomographic analysis after 15 ms of one-axis twisting evolution without spin-echo pulse shows that the classical fluctuations are directional and have a distinct maximum in phase direction (right panel, black diamonds). Assuming detuning fluctuations of $\sigma_\delta = 2\pi \times 0.45\,\mathrm{Hz}$, corresponding to the independently measured field stability of $\sigma_B = 45\,\mu\mathrm{G}$, a numerical analysis considering the fluctuations of the expectation values yields perfect agreement with the experimental data points (solid line).

number difference $\mathrm{Var}(N_\mathrm{b} - N_\mathrm{a})$, similar to the analysis of number squeezing in the previous section. To extract solely the classical noise contribution and get rid of atom number dependent effects of the single sites, we average all possible combinations of adjacent sites and calculate their mean fluctuations. A system without classical fluctuations should show a linear dependence $\mathrm{Var}(N_\mathrm{b} - N_\mathrm{a}) = \mathrm{Var}_\mathrm{Det} + \alpha N_{\mathrm{tot}}$ versus total atom number $N_{\mathrm{tot}} = N_\mathrm{a} + N_\mathrm{b}$, where $\mathrm{Var}_\mathrm{Det}$ is given by the detection noise of the experimental system. In contrast, classical noise sources show up as a quadratic contribution $\beta^2 N_{\mathrm{tot}}^2$. Intuitively, this can be understood from the fact that classical fluctuations lead to an angular variation on the Bloch sphere which is independent of atom number, whereas the normalized quantum fluctuations decrease with $1/\sqrt{N}$ in standard deviation [62]. We experimentally extract $\beta^2$ from a linear fit $f = \alpha + \beta^2 N_{\mathrm{tot}}$ to the squeezing factor $\xi_N^2 = \mathrm{Var}(N_\mathrm{b} - N_\mathrm{a})/(4p(1-p) \cdot N_{\mathrm{tot}})$, as depicted in the left panel of Fig. 6.5.

For the one-axis twisting scenario without spin-echo pulse, the dependence of the classical noise on tomography angle in Fig. 6.5 confirms that during the nonlinear evolution, technical fluctuations occur only in phase direction (fringe with maximum 90°), whereas no classical



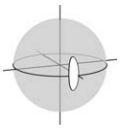

fluctuations can be found for the unrotated state. This shows that the generation of squeezed states is mainly affected by phase fluctuations originating from jitter of the magnetic field as described above, and that amplitude fluctuations in the coupling power of the initial $\pi/2$ pulse, which would result in technical noise for the unrotated state, are negligible. The solid black line in Fig. 6.5 shows the results obtained from a numerical simulation of the squeezing sequence taking into account magnetic field fluctuations of $\sigma_B = 45\,\mu\text{G}$ (as independently characterized from the scatter of repeated Ramsey measurements on a first-order Zeeman sensitive transition). The analysis of the fluctuations in the corresponding expectation values of the final states yields excellent agreement with the experimental results.

### 6.3.2. Reduction of Technical Noise: Spin-Echo Pulse in the One-Axis Twisting Scenario

The phase fluctuations induced by the magnetic field fluctuation can be strongly reduced with the implementation of a spin-echo $\pi$ pulse in the middle of the nonlinear evolution. For a homogeneous offset field, the phase acquired in the second part of an ideal spin-echo sequence exactly cancels the phase that was accumulated in the first half (see Fig. 6.6 a).

#### Pulse imperfections and how they affect the noise cancellation

In our experiment, however, things are complicated by the presence of the nonlinear interaction $\chi \hat{J}_z^2$, which is also present during the coupling pulses of the spin-echo sequence. Even though during these strong pulses, the system is deep in the Rabi regime of dominating coupling ($\lambda = N\chi/\Omega \approx 0.1$), the presence of interaction significantly alters the resulting dynamics during the pulse. In our sequence, the spin-echo pulse is performed as a rotation with pulse length $\tau = \pi/\Omega$ and a phase of $\phi = 3\pi/2$, at which the nonlinearity counteracts the effect of the rotation. This results in $\pi$ oscillations [69, 70], which have a reduced rotational frequency of $\omega_\pi = \Omega\sqrt{1-\lambda}$ (see Eq. 2.45). For $\lambda = 0.1$, the corresponding frequency is $\omega_\pi \approx 0.95\Omega$. Thus, after a pulse length of $\tau$, the state is rotated by only 171°. It is important to note that this also leads to a finite population imbalance $z$ after the pulse, which is proportional to the accumulated phase and thus to the detuning of the sequence.

In the case of a linear evolution in the second part of the sequence, phase noise is still canceled to a level of $\approx 1\%$, and about 15% of the noise is transferred to the $z$ direction. This can be seen in Fig. 6.6b, which depicts the resulting expectation values $\langle z_\delta \rangle$ vs. $\langle \phi_\delta \rangle$ for different detunings $\delta$ after 7.5 ms of linear evolution time with $\mathcal{H} = \delta \hat{J}_z$, a subsequent $\pi$ pulse in the presence of nonlinearity, and a second period with 7.5 ms of linear evolution. The resulting angular dependence of the technical noise has a strongly suppressed amplitude with a maximum in $z$ direction (blue line in right panel). This can be explained by the fact that the phase noise compensation of the spin-echo pulse is still almost perfect (cosine dependence on errors in rotation angle of the pulse), whereas the fraction of the fluctuations that is transferred into the imbalance direction cannot be canceled during the second period of linear evolution.

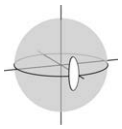

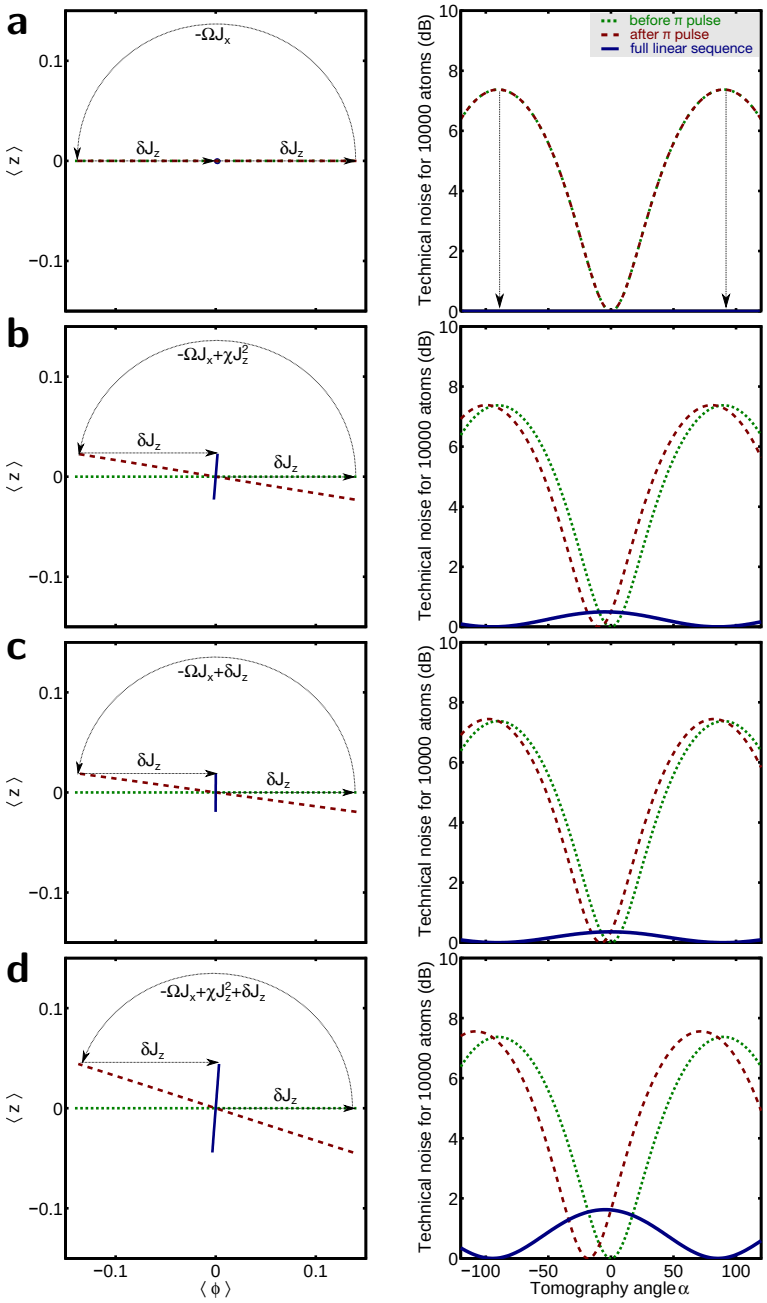


Figure 6.6.: **Spin-echo $\pi$ pulse and imperfections with linear evolution.** We numerically simulate 15 ms of quantum evolution with $\mathcal{H} = \delta \hat{J}_z$ for initial states with $N_0 = 500$ atoms at $\langle z_0 \rangle = \langle \phi_0 \rangle = 0$ and varying detuning $\delta = 2\pi \times [-3... + 3]$ Hz. A spin-echo pulse (phase $3\pi/2$) is applied in the middle of the time evolution. The left panels show the expectation values $\langle z \rangle$ vs. $\langle \phi \rangle$ before the spin-echo pulse (dotted green line), after the pulse (dashed red line) and after the full sequence (solid blue line). The right panels show the resulting variance in the expectation value for tomographic readout, assuming Gaussian detuning fluctuations of $\sigma_\delta = 2\pi \times 0.45$ Hz (units of a coherent state with $10^4$ particles). While an unperturbed $\pi$-pulse perfectly cancels all fluctuations (a), this is not the case if the pulse is performed in the presence of nonlinearity [(b) for $\Lambda = 0.1$], as this effectively shortens the rotation. A similar effect is observed if the detuning fluctuations $\sigma_\delta$ are included in the pulse without interaction [(c)]. For a pulse phase of $3\pi/2$, the effects add up [(d)]. In the case of linear evolution, this leads to maximal technical fluctuations in $z$ direction (solid lines on right panel). The presence of nonlinear interaction during the second half of the evolution strongly alters this result (see Fig. 6.7).

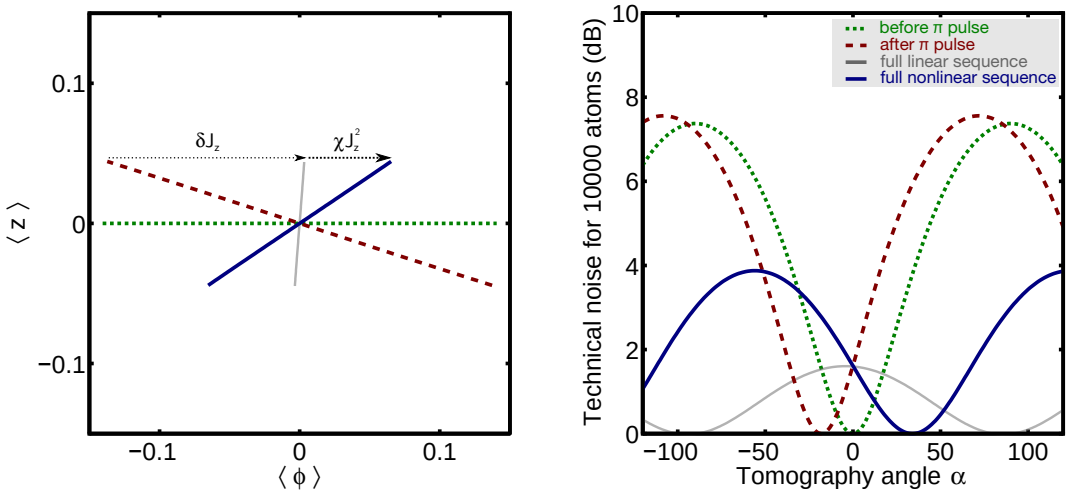


Figure 6.7.: **Technical noise amplification by one-axis twisting evolution.** The technical fluctuations are amplified by the presence of the nonlinearity $\chi \hat{J}_z^2$ during the second part of the sequence. Again, this can be visualized by plotting the expectation values $\langle z \rangle$ vs. $\langle \phi \rangle$ obtained from numerical simulations for $\delta = 2\pi \times [-3...+3]$ Hz, and the corresponding technical noise amplitudes obtained for $\sigma_\delta = 2\pi \times 0.45$ Hz after tomographic readout. As in the linear scenario, after the spin-echo pulse a part of the phase noise is transferred into fluctuations of the population imbalance (the dotted green line shows fluctuations before, the dashed red line after the $\pi$ pulse). The nonlinearity during the second part of the evolution leads to a $z$ dependent rotation frequency. Thus, the rotation frequency at finite $z$ is increased. This inhibits the cancellation in phase direction and amplifies the amplitude of the fluctuations (solid blue lines vs. solid gray line, which depicts the result for a linear sequence as in Fig. 6.6).

A second imperfection which has similar consequences is the fact that the varying detuning which is caused by the jitter of the offset field is also present during the spin-echo $\pi$ pulse. This leads to an effective tilt of the rotation axis by $\theta_r = \arcsin\left(\delta/(\sqrt{\Omega^2 + \delta^2})\right)$, which is correlated with the phase that is acquired during the first evolution period (i.e. $\delta < 0$ leads to $\theta_r < 0$ and vice versa). Even though these variations in the rotation axis are very small for our parameters – a field offset of 45 µG translates into a tilt of just $\theta_r \approx 0.1°$ – this becomes important due to the correlation with the acquired phase. This is because the tilt of the rotation axis also redistributes a fraction of the classical fluctuations into fluctuations of the population imbalance after the $\pi$ pulse. Surprisingly, for our parameter regime, this effect is of comparable size with the influence of the nonlinearity during the pulse (see Fig. 6.6 b,c).
The above analysis is done for a linear phase evolution with $\mathcal{H} = \delta \hat{J}_z$. For the generation of squeezed states, however, the resulting classical noise along the $z$ direction is significantly modified by the presence of a $\hat{J}_z^2$ term that acts on the detuning dependent imbalance. This strongly increases the fluctuation amplitude in phase direction and thus changes the angular dependence and the amplitude of the technical fluctuations. This effect can be seen in Fig. 6.7,

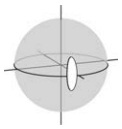

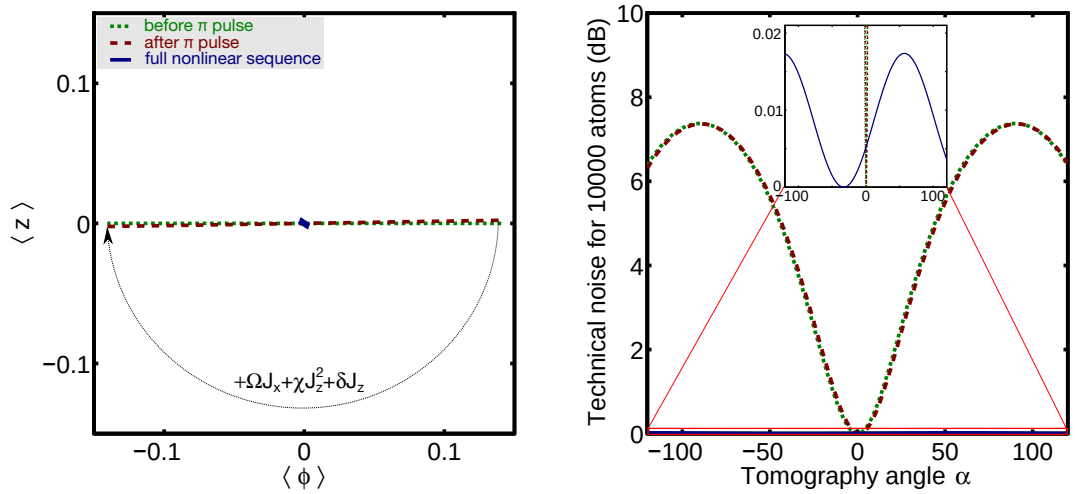


Figure 6.8.: **Technical noise reduction with optimized pulse.** Changing the phase of the spin-echo rotation to $\phi = \pi/2$ allows to almost perfectly cancel the technical fluctuations even for a nonlinear evolution. The dotted green line represents the expectation values before the pulse, the dashed red line directly after the pulse, and the solid blue line is the result after the second period of nonlinear evolution. With this opposite rotation phase, the effects from nonlinearity and detuning during the spin-echo pulse cancel each other, allowing to suppress the resulting classical noise by more than an order of magnitude (detail in inset of right panel) compared to a pulse with $\phi = 3\pi/2$.

which shows that for the typical experimental parameters, a significant increase in fluctuations is caused even for a short total evolution time of $t_{\mathrm{int}} = 15\,\mathrm{ms}$, and the angular dependence is distinctly changed.

### A route for improvement: Changing the pulse phase

Both imperfections can be taken care of by implementing an optimized spin-echo pulse. For our parameter regime, almost perfect cancellation can be achieved by either increasing the duration of the spin-echo pulse to $1.1\pi$, or by simply changing the phase of the coupling radiation to $\pi/2$. Here, nonlinear effects are effectively canceled by the effect of the tilted rotation axis due to the detuning fluctuations (Fig. 6.8). With these small modifications of the pulse sequence, the number squeezing parameter should be unaffected by the technical instabilities even for large ensemble sizes (inset of right panel in Fig. 6.8), rendering a differential analysis unnecessary.



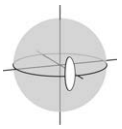

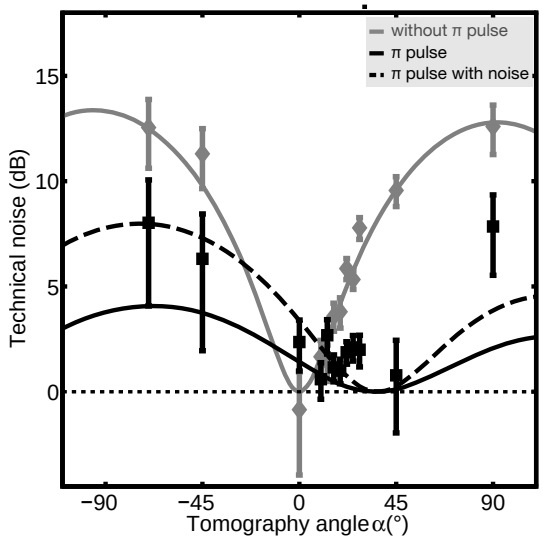


Figure 6.9.: **Technical noise for one-axis twisting evolution.** The implementation of a spin-echo pulse reduces the noise amplitude by almost 5 dB (black squares) compared to an evolution without $\pi$-pulse (gray diamonds). However, from our classical noise modeling, we expect a stronger suppression for a detuning variation of $\sigma_\delta = 2\pi \times 0.45\,\mathrm{Hz}$ (solid black line), which fits excellent in the case of no spin-echo pulse. This difference could be explained by additional detuning variations during the $\pi$ pulse (dashed black line), potentially caused by fluctuation of the AC Zeeman shifts from our microwave source or spurious feedback of the radiation on the magnetic field stabilization.

### Experimental results

As shown in the previous paragraphs, for our experimental settings we expect classical noise also in a spin-echo sequence. In Fig. 6.9, we compare the classical noise model with the experimental results which were obtained after 15 ms of evolution time with a $\pi$ pulse around $\phi = 3\pi/2$. We find good qualitative agreement with the theory, assuming detuning fluctuations of $\sigma_\delta = 2\pi \times 0.45\,\mathrm{Hz}$, but experimentally observe stronger fluctuations that are inconsistent with the data obtained without spin-echo pulse. Thus, these fluctuations have to be related to the spin-echo pulse itself. We find that additional random detuning fluctuations of $\sigma_{\delta\mathrm{Pulse}} = 2\pi \times 1.3\,\mathrm{Hz}$ can capture this increased variance. These fluctuations might be caused by fluctuating light shifts during the strong two-photon pulse ($\delta_{\mathrm{LS}} \approx 200\,\mathrm{Hz}$) or a perturbation of the magnetic field stabilization from the high-power radio frequency radiation during the pulse, and cannot be reduced by a simple change of the coupling phase.

## 6.3.3. Technical Noise for Bifurcation Squeezing

The effect of fluctuations of the magnetic bias field becomes even more subtle in the bifurcation squeezing scenario due to the presence of coupling during the nonlinear evolution time. In

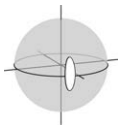

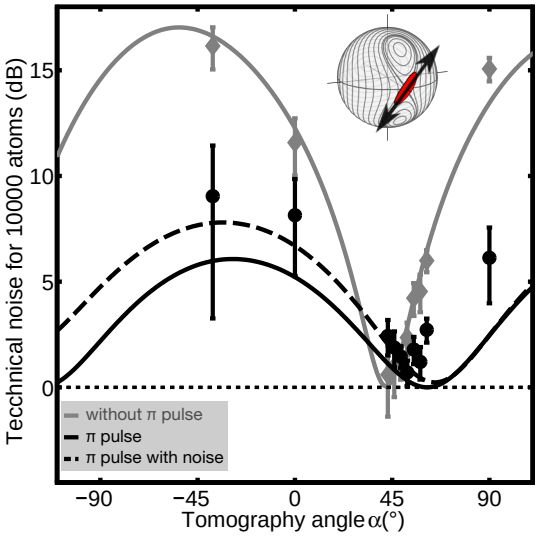


Figure 6.10.: **Technical noise for bifurcation squeezing.** In the bifurcation squeezing scenario, detuning fluctuations manifest themselves not only in the phase, but also in the population imbalance. The preparation on the unstable fixed point makes the system critical on small fluctuations, which can be seen from the fact that after 15 ms of evolution without a spin-echo pulse, the fluctuations in the bifurcation scenario (gray diamonds) are a factor of 1.6 larger than for one-axis twisting. These fluctuations in the bifurcation scenario can be reproduced by numerical simulations with $\sigma_\delta = 2\pi \times 0.45\,\mathrm{Hz}$ (solid gray line). Similar to the one-axis twisting scenario, a spin-echo pulse can be employed to reduce the fluctuations (black circles). As in the one-axis twisting case, additional fluctuations of the $\pi$ pulse detuning have to be assumed to reproduce the amplitude of the observed fluctuations (dashed black line, solid black line without additional noise).

this case, the dynamics also in $z$ direction strongly depends on the value of $\delta$ (see section 2.6). A numerical analysis for the evolution of the expectation values $\langle z_\delta \rangle$ vs. $\langle \phi_\delta \rangle$ for different detunings shows that, using the parameters employed in the experiment, the resulting classical variation is $\approx 1.6$ times larger than in the one-axis twisting scheme. This amplification can be understood from the fact that the classical fluctuations are enhanced by the presence of unstable fixed point dynamics, which are very sensitive on tilts of the corresponding double well potential.

For an evolution time of 15 ms without a spin-echo pulse and our experimental parameters ($N\chi = 2\pi \times 30\,\mathrm{Hz}$, $\Omega = 2\pi \times 18\,\mathrm{Hz}$), experimental data and numerical simulation yield perfect agreement assuming classical detuning fluctuations of $\sigma_\delta = 2\pi \times 0.45\,\mathrm{Hz}$, which were also well suited to model the technical fluctuations in the one-axis twisting scenario without spin-echo.



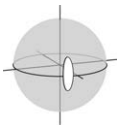

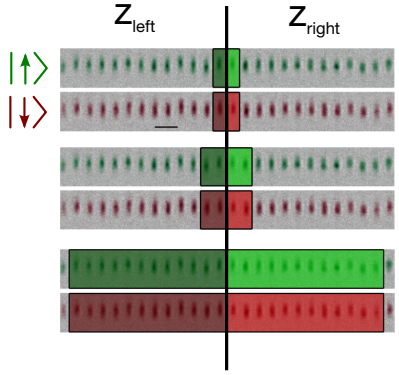


Figure 6.11.: **Evaluation of relative squeezing in a 1D lattice.** For our relative squeezing evaluation, we split our lattice in two equal halves. The scaling with system size is observed by symmetrically summing more and more sites in both halves and evaluating the fluctuations of the difference between the respective population imbalances $z_{\text{left}}$ and $z_{\text{right}}$.

Even the implementation of a perfect spin-echo pulse does not lead to a complete cancellation of detuning fluctuations in the bifurcation scenario, as the phase space in the presence of a detuning is no longer symmetric. Despite not yielding a perfect compensation, we still find a reduction of the final state's susceptibility to classical fluctuations (see Fig. 6.10). As in the one-axis twisting case, including the known imperfections due to nonlinearity and detuning into the spin-echo sequence is not sufficient to explain the full classical variation observed in the experiment (solid line): The amplitude of the fluctuations suggests additional fluctuations in the pulse detuning ($\sigma_{\delta\text{Pulse}} = 2\pi \times 1.3\,\text{Hz}$ in Fig. 6.10 [dashed line]).
The fact that we obtain better number squeezing using the bifurcation scenario is due to the fact that for our experimental parameters, the angle $\alpha_{\text{min}}$ of minimal squeezing and the one with minimized technical fluctuations $\alpha_{0\text{tech}}$ almost coincide. The scaling in the one-axis twisting scenario with the imperfect spin-echo pulse is worse due to the fact that $\delta\alpha = \alpha_{0\text{tech}} - \alpha_{\text{min}}$ is larger. Recall that for the extreme case of the one-axis twisting scenario without spin-echo pulse, the strong classical fluctuations start to dominate for large atom numbers and the angle of best observed number squeezing approaches $\alpha_{0\text{tech}} = 0°$ (see Fig. 6.4).

## 6.4. Relative Squeezing: Directly Assessing the Quantum Uncertainty of the State

In the previous section, we have characterized the nature and origin of the classical fluctuations in our system, which limit $\xi_N^2$ for large atom numbers. As shown in section 4.1.4, a differential analysis between two independent samples that are created in the same experimental shot allows to directly assess the true quantum resources of the state, as this approach is insensitive to such classical fluctuations of homogeneous fields. In addition, the relative squeezing

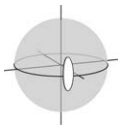

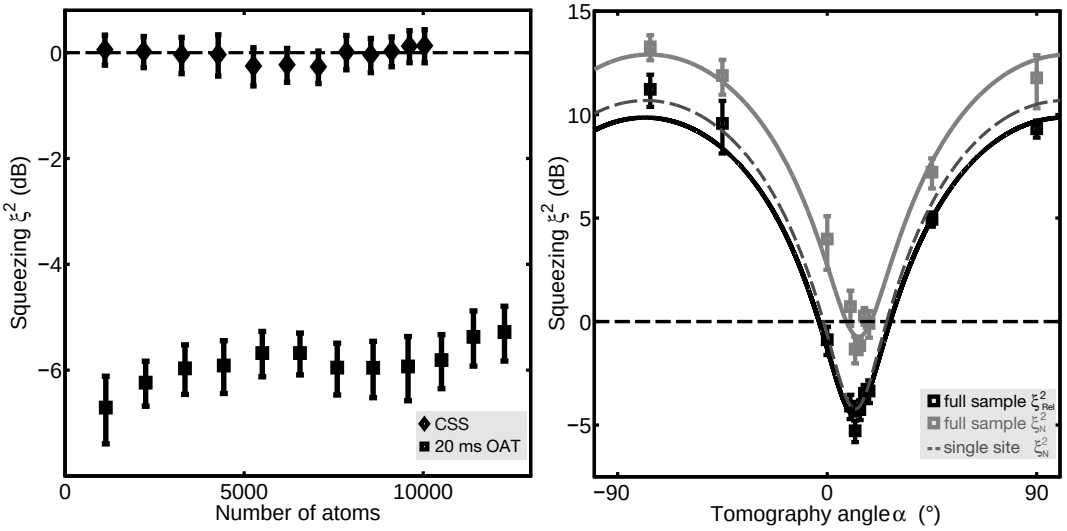


Figure 6.12.: **Relative squeezing in the one-axis twisting scenario.** Evaluating the relative squeezing parameter $\xi^2_{\mathrm{Rel}}$ for different system sizes, we find comparable values for all system sizes after 20 ms of one-axis twisting with spin-echo pulse (black squares in the left panel). For the full sample of 12 300 atoms and the optimal tomography angle, this yields $\xi^2_{\mathrm{rel}} = -5.3(5)$ dB. The corresponding classical reference remains unchanged (CSS, black diamonds in left panel). A tomographic analysis shows that the obtained values for the relative squeezing surpass the direct number squeezing $\xi^2_{\mathrm{N}}$ evaluated for the same data set (gray squares) along all directions and correspond to the values of $\xi^2_{\mathrm{N}}$ for the single lattice sites (sinusoidal fit to the data as dashed gray line).

parameter $\xi^2_{\mathrm{Rel}}$ is directly connected to the attainable quantum enhancement for gradiometric measurements.

We now investigate the scaling of $\xi_{\mathrm{rel}}$ with system size. To do this, we proceed in a similar fashion as in the number squeezing evaluation. We divide our sample in two equal halves and start with two single adjacent lattice sites in the center, for which we calculate $\delta z = z_{\mathrm{left}} - z_{\mathrm{right}}$ from the respective population imbalances. With this and the respective atom numbers $N_{\mathrm{left}}$ and $N_{\mathrm{right}}$, we obtain the relative squeezing parameter according to Eq. 4.13. We then symmetrically add more and more sites to both parts, recalculate $\delta z$ and extract the corresponding relative squeezing factor.

The results for the state obtained after 20 ms of one-axis twisting are shown in Figure 6.11. As the analysis is insensitive to the detuning fluctuations, we find that squeezing remains on an almost constant level, only slightly altered for large numbers where the atom number inhomogeneity of the lattice becomes relevant. For 12 300 atoms, we still find a suppression of fluctuations by $\xi^2_{\mathrm{rel}} = -5.3(5)$ dB. For all tomography angles, we find less fluctuations compared to the direct number squeezing evaluation of the same data.

Taking into account the visibility of $\mathcal{V} = 0.952(3)$, this yields an effective spin squeezing parameter of $\xi^2_{\mathrm{S}} = -4.9(5)$ dB. Recall that this value is inferred by subtraction of detection noise.



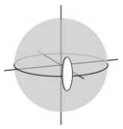

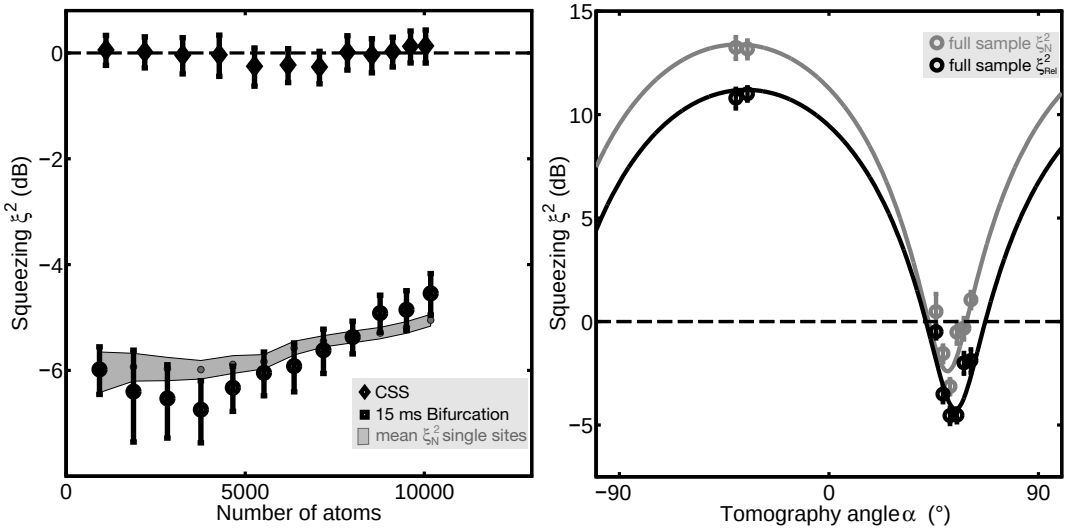


Figure 6.13.: **Relative squeezing using the bifurcation scheme.** The relative analysis also shows reduced fluctuations for the state produced by 15 ms of bifurcation squeezing (left panel: circles for the best tomography angle, black diamonds for $\xi^2_{\mathrm{Rel}}$ of a CSS), yielding $\xi^2_{\mathrm{rel}} = -4.5(4)$ dB for 10 100 atoms. However, the dependence of the obtained relative squeezing $\xi^2_{\mathrm{Rel}}$ on the atom number inhomogeneities is stronger than in the one-axis twisting case. A comparison with the weighted mean of the number squeezing parameters obtained from the single lattice sites (gray points with gray uncertainty area) shows that this decreasing suppression factor is due to the fact that the outer lattice sites are less squeezed, leading to a reduced mean squeezing. The right panel compares the squeezing tomographies for $\xi^2_{\mathrm{N}}$ (gray) and $\xi^2_{\mathrm{rel}}$ (black), showing a larger suppression for the differential analysis along all directions.

For an interferometric measurement with our setup, the bare value without detection noise subtraction determines the sensitivity. Without this subtraction, we find $\xi^2_{\mathrm{S}} = -3.8(5)$ dB of spin squeezing with 12 300 particles, directly applicable for quantum-enhanced interferometry.

The relative analysis works similarly well for the bifurcation squeezing scenario, where classical fluctuations are also suppressed in all directions (Fig. 6.13). Here, we find the best relative squeezing for the full sample to be $\xi^2_{\mathrm{rel}} = -4.5(4)$ dB, equivalent to $\xi^2_{\mathrm{S}} = -4.0(4)$ dB, but a stronger dependence on the ensemble size. This is because the parameters that define the unstable fixed point dynamics critically depend on atom number, leading to even qualitatively different final states for different particle numbers (see Chapter 5). Thus, for our system the effects of an inhomogeneous atom number distribution over the different sites are more important and lead to inferior scaling behavior at large numbers. This can be seen from a comparison of the weighted mean of the number squeezing parameters obtained from the single lattice sites that takes these inhomogeneities into account and is in good agreement with the relative squeezing factor obtained for different sample sizes.

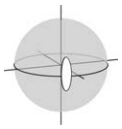

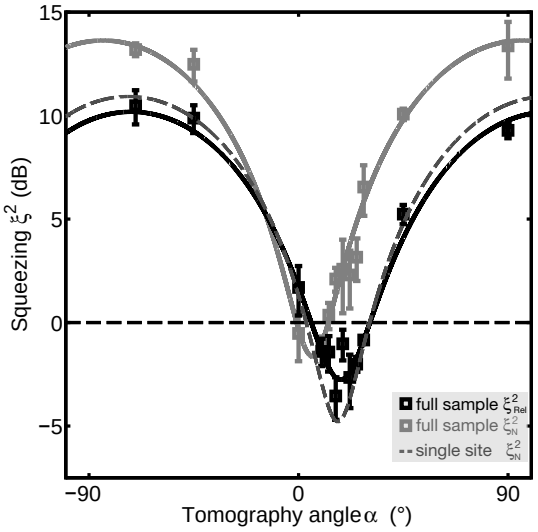


Figure 6.14.: **Relative squeezing after 15 ms of one-axis twisting without spin-echo.** In contrast to the number squeezing analysis (solid gray), the tomographic evaluation of relative squeezing (solid black) of the full ensemble remains almost at the single lattice site level (dashed gray line) and shows no significant shift in the optimal tomography angle. For this optimal rotation angle, the relative analysis yields a reduction of fluctuations by more than 5 dB since it is insensitive to the classical noise that dominates the number squeezing analysis at this point.

Even for the one-axis twisting sequence without spin-echo pulse, we still find more than $\xi^2_{\mathrm{rel}} = -3\,\mathrm{dB}$ of relative squeezing for the full sample. The tomographic evaluation of the full ensemble does not show the characteristic shift in the optimal tomography angle that is found in the number squeezing analysis (see Fig. 6.14), showing that our analysis is insensitive even in the case of stronger classical noise contributions.

In this chapter, we have shown that the only limitation for the scaling of squeezing to large atom numbers are the atom number inhomogeneities of the lattice, which especially in the one-axis twisting scheme only lead to slight deterioration of the attainable resource. The maximum number of atoms for the squeezed states generated in our 1D lattice is currently only limited by the trapping geometry of the experiment, which allows the reproducible generation of up to 30 independent BECs. To attain larger numbers, the same approach can in principle be extended to a three-dimensional lattice, increasing the atom number by a factor of up to $10^3$. This can be achieved using three pairs of beams, each crossed under a small angle, in analogy to the 1D lattice setup. Note that both the generation procedure and the readout do not rely on the ability to spatially resolve the single lattice sites, which would be a difficult task for a three-dimensional system. Hyperfine–state-resolved imaging of the two components suffices in this situation. For $^{87}$Rb, this is experimentally feasible due to the large hyperfine splitting of 6.8 GHz between the two states.



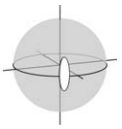

This scalable generation procedure for squeezed states thus opens the route for the creation of large quantum-enhanced resources in Bose-Einstein condensates that can readily be employed for precision measurements in atom interferometry [116]. In the next chapter, we will show how such an interferometric measurement scheme can be implemented, and experimentally demonstrate quantum-enhanced magnetometry with our upscaled resource.

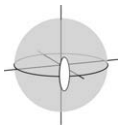

# 7. Quantum-Enhanced Magnetometry with Bose-Einstein Condensates

A multitude of today's precision measurements builds on atom interferometry [116], which enables the precise determination of phase shifts induced by the measured quantity. Using this technique, state-of-the-art measurements of quantities like frequencies [57], accelerations [53, 54], rotations [55] and electromagnetic fields [48] have been performed. Many of these atom interferometers operate at or near the classical limit for measurement precision [7, 8, 9], which is given by the atomic projection noise [100] in the employed two modes. It has been shown that this limit can be surpassed by employing entangled states at the input of the interferometer [12].

In this chapter, we will present a scheme for the entanglement-enhanced measurement of static magnetic fields. Our input states are spin squeezed states in two internal modes of a Bose-Einstein condensate, for which the generation and characterization procedure was discussed in the previous chapters.

In the first section of this chapter, we will review how squeezed states can be employed to improve the precision of a Ramsey interferometer, and how such an interferometer can be implemented in the experiment. In the following section, we will discuss the effects caused by nonlinear evolution during the measurement time, and show how we can swap the squeezed state to different internal levels to strongly reduce the strength of the nonlinearity and improve the sensitivity on a desired quantity. In the third section, we will show that this can be used to perform quantum-enhanced magnetometry, discuss the limitations of our system and compare the obtained sensitivity to those achieved with other state-of-the-art techniques. Lastly, we will present gradiometric measurements of static magnetic fields in our experiment, and analyze the corresponding sensitivities of our device. The results shown in this chapter are summarized in a publication [60].

## 7.1. Ramsey Interferometry with Squeezed States

Ramsey's method of separated oscillatory fields [117] has nowadays become a standard tool for the precise determination of phase shifts in atomic systems. It consists of two $\pi/2$ pulses separated by a phase evolution time, and is the atomic equivalent to an optical Mach-Zehnder interferometer [118]: The first $\pi/2$ pulse creates an equal superposition of two atomic states $|\uparrow\rangle$ and $|\downarrow\rangle$, which accumulate a relative phase $\theta$ during the subsequent phase evolution. The second $\pi/2$ pulse maps this phase $\theta$ into a population imbalance $z = (N_\uparrow - N_\downarrow)/(N_\uparrow + N_\downarrow)$ between the two states. Thus, the acquired phase can be extracted by detecting the populations of the two states after the Ramsey sequence.

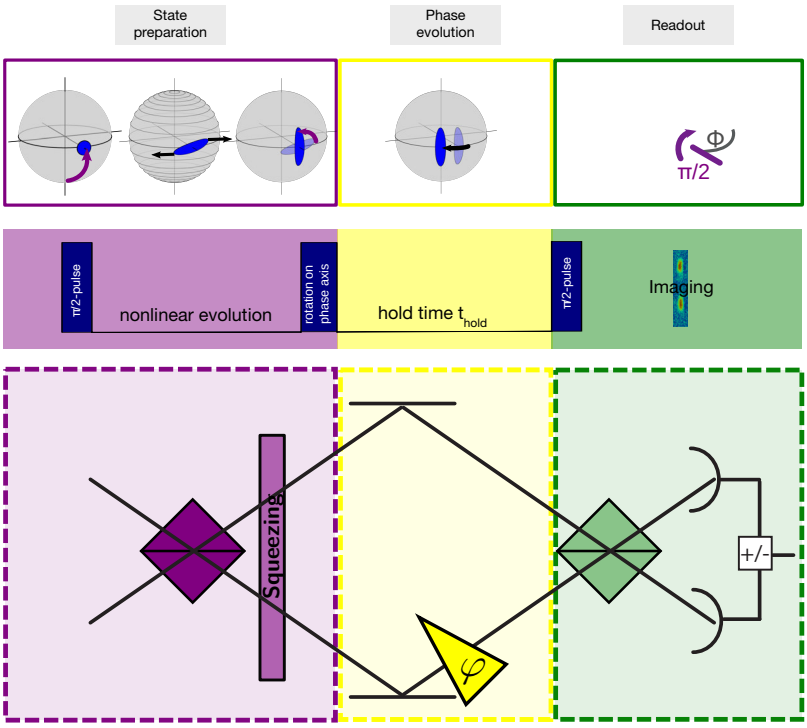


Figure 7.1.: **Ramsey interferometer with a squeezed input state.** The implementation of a squeezed Ramsey sequence starts with the generation of a spin squeezed state using a $\pi/2$ pulse and subsequent nonlinear one-axis twisting (Bloch spheres in upper left panel). To obtain increased phase sensitivity, the state is rotated onto the phase squeezed axis. Subsequent phase evolution is followed by a final $\pi/2$ pulse, which maps the differential phase into a population imbalance. This population imbalance is determined from the detected atom numbers in the two components. The experimental pulse sequence is depicted in the middle panel. Such a sequence is formally equivalent to a Mach-Zehnder interferometer in which the two modes are entangled after the first beam splitter (lower panel).

By varying the readout phase $\Phi$ of the second $\pi/2$ pulse with respect to the atomic phase, the output of a Ramsey sequence yields a sinusoidal fringe in the population imbalance

$$z(\Phi) = \mathcal{V}\cos(\Phi + \theta) \tag{7.1}$$

with the fringe visibility $\mathcal{V} \leq 1$.
The relative phase $\theta$ can thus be estimated by inverting Eq. 7.1, yielding

$$\theta = \arccos\left(\frac{z}{\mathcal{V}}\right) - \Phi, \tag{7.2}$$

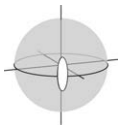

and by error propagation we find

$$\mathrm{Var}(\theta) = \frac{\mathrm{Var}(z)}{\mathcal{V}^2 - z^2}. \tag{7.3}$$

The sensitivity of such a Ramsey sequence with uncorrelated particles is bounded by the classical limit for phase precision, the so-called *standard quantum limit* (SQL). This limit is imposed by the intrinsically isotropic quantum uncertainty of the classical input state, which translates into finite fluctuations of $\mathrm{Var}(z) = (1 - \langle z \rangle^2)/N$ for a mean output imbalance of $\langle z \rangle$ and the total number of atoms $N$ (Eq. 4.5). For a perfect classical interferometer [$\mathcal{V} = 1$ and $\mathrm{Var}(z) = (1 - \langle z \rangle^2)/N$], this yields the standard quantum limit

$$\Delta\theta_{\mathrm{SQL}} = \frac{1}{\sqrt{N}}. \tag{7.4}$$

However, this is not the fundamental limit and only valid for uncorrelated 'classical' particles. Employing entangled input states, the phase uncertainty can be reduced down to the fundamental Heisenberg limit $\Delta\theta_{\mathrm{HL}} = 1/N$ [12, 119] imposed by quantum mechanics.
Among the most promising classes of entangled states for applications in quantum metrology are spin squeezed states [25, 101], which are comparatively robust against environmental noise and losses [26, 27, 28, 29]. In an interferometric sequence, spin squeezed states can outperform the standard quantum limit at a level quantified by the metrological spin squeezing parameter $\xi_{\mathrm{R}} = \xi_{\mathrm{N}}/\mathcal{V}$ (see Chapter 4.1.3), yielding a phase sensitivity of [101, 12]

$$\Delta\theta_{\mathrm{sq}} = \xi_{\mathrm{R}} \cdot \Delta\theta_{\mathrm{SQL}} = \frac{\xi_{\mathrm{R}}}{\sqrt{N}}. \tag{7.5}$$

Using Eq. 7.3, this can be straight-forwardly seen from the fact that the fluctuations in the population imbalance $z$ are suppressed by $\mathrm{Var}(z) = \xi_{\mathrm{N}}^2(1 - \langle z \rangle^2)/N$, while the amplitude of the Ramsey fringe is reduced to $\mathcal{V}$.
In the photonic case, squeezed states are already routinely employed to enhance the sensitivity of optical gravitational wave detectors [14]. In the atomic realm, proof-of-principle experiments have shown various methods for creating spin squeezed states in systems ranging from high-temperature vapors to ultracold Bose-Einstein condensates (BEC) [31, 5, 34, 45, 46, 39, 35, 36, 37, 47, 38]. The feasibility for applications has been shown in demonstrations of quantum enhancement in atom interferometry [45, 48], atomic magnetometers [37, 42], and atomic clocks [40, 41].

The experimental implementation of a spin squeezed Ramsey sequence in a two-level system was demonstrated in [45, 48, 40, 41] and is schematically depicted in Fig. 7.1. It starts with a $\pi/2$ pulse, followed by nonlinear evolution for the creation of a spin squeezed state. To attain maximum phase sensitivity, the state is subsequently rotated around itself such that the axis of minimum fluctuations is along the phase direction. After the subsequent phase evolution time, a final $\pi/2$ rotation converts the accumulated phase into a population imbalance and thus rotates the axis of minimal fluctuations in readout direction (i.e., converts the phase



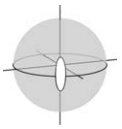

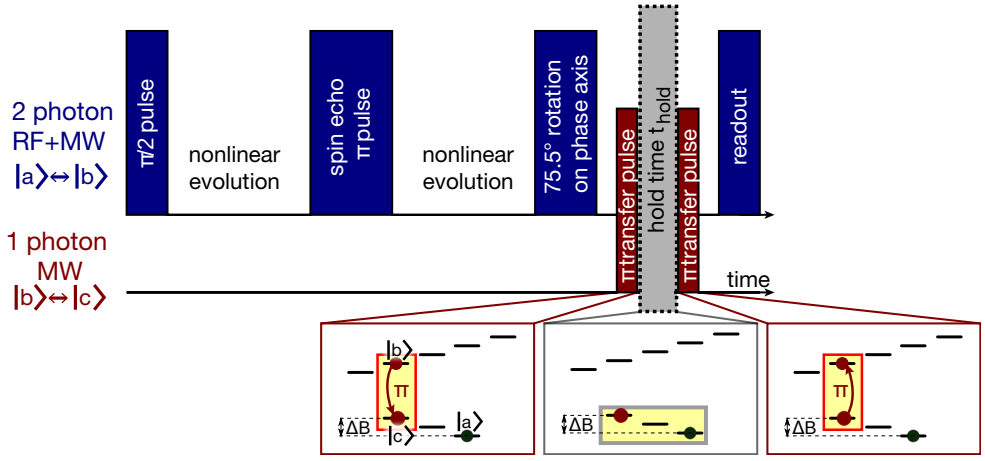


Figure 7.2.: **Pulse sequence for Ramsey interferometry with state swapping.** In addition to the 'standard' squeezed Ramsey sequence, which is depicted in Fig. 7.1, in this sequence the internal states are swapped at the beginning of the interrogation time. To do this, a one-photon microwave $\pi$ pulse transfers the population of the level $|b\rangle = |2,-1\rangle$ to the hyperfine state $|c\rangle = |1,-1\rangle$. The states $|a\rangle$ and $|c\rangle$ feature a large magnetic field sensitivity, while their nonlinear interaction strength is negligible. After a hold time $t_{\mathrm{hold}}$ for phase evolution, the atoms are transferred back to $|b\rangle$ for the final readout rotation.

squeezed state into a number squeezed state). Using cold atom systems, implementations of atomic clocks building on such a squeezed Ramsey sequence have been shown in the groups of Vladan Vuletić and Eugene Polzik. In the Polzik group, an entanglement-assisted clock using conditional squeezed states at the input demonstrated 1.1 dB improvement for interrogation times of 10 µs [40], whereas for longer interrogation times quantum enhancement was lost due to the dominant classical noise sources. An improvement in the variance of 4.5 dB over the standard quantum limit was reached for interrogation times of 200 µs in the group of Vladan Vuletić group using unconditional cavity squeezing [41].
In Bose-Einstein condensates, a first proof-of-principle demonstration of squeezed atom interferometry showed a quantum enhancement of 1.4 dB for an interrogation time of just 2 µs [45]. Recently, a spin squeezed BEC demonstrated quantum-enhanced sensing of near-field microwave radiation at a level of $\xi_{\mathrm{R}}^2 \approx -4$ dB below the standard quantum limit with interrogation times in the range of milliseconds, and demonstrated quantum enhancement in a scanning probe interferometer configuration.

## 7.2. State Swapping for Interaction Switching

In principle, if spin squeezed states have been successfully generated in the experiment, a Ramsey sequence with these squeezed input states as described in the previous section can be straight-forwardly implemented [41, 40, 45, 48]. However, for many metrological applica-

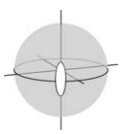

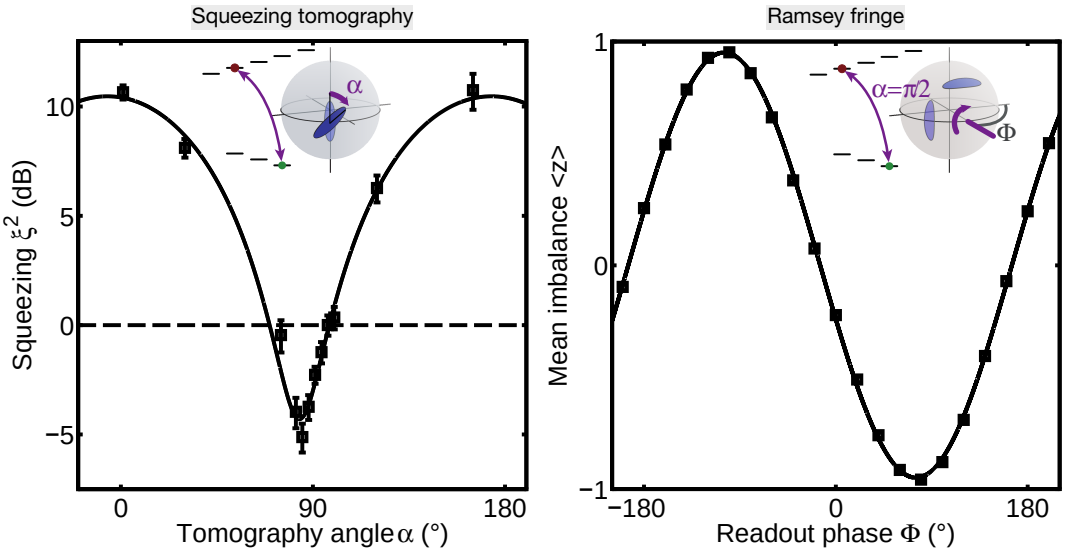


Figure 7.3.: **Squeezing after state swapping.** A squeezing tomography after the full interferometric sequence, consisting of state swapping, a hold time of 1 µs, and swapping back, verifies that relative squeezing between left and right part of the full array of $\xi^2_{\mathrm{rel}} = -5.1^{+0.6}_{-0.7}$ dB is present (left panel). For a Ramsey fringe obtained after the same hold time of 1 µs and a $\pi/2$-pulse with varying readout phase, we find a visibility $\mathcal{V} = 0.950(5)$ (right panel). Combined, using the Wineland criterion [101], this yields metrologically relevant spin squeezing of $\xi^2_{\mathrm{R}} = -4.7(6)$ dB after subtraction of detection noise and directly applicable squeezing of $\xi^2_{\mathrm{R}} = -3.4(5)$ dB without noise subtraction.

tions with Bose condensed clouds, two major problems remain to be solved:

The first issue is the fact that spin squeezing is generated on two particular internal states of the Bose-Einstein condensates. However, this set of states might be insensitive to the quantity which we want to measure. For example, in our experiment, the squeezed states are generated on the two hyperfine states $|a\rangle = |1, 1\rangle$ and $|b\rangle = |2, -1\rangle$, which are only quadratically sensitive on magnetic fields and thus optimal for reproducibility of the generation procedure. However, if we want to measure magnetic fields, this low magnetic sensitivity consequentially renders the system impractical.
Secondly, in our setup, the nonlinear interaction cannot easily be switched off, as it is generated by a Feshbach resonance. Controlled ramping away from the resonance is experimentally challenging and suffers from shot-to-shot fluctuations during the ramps, which translate into increased phase noise and deteriorate the quantum resource.

Both of these problems can be resolved by swapping the squeezed state to different hyperfine levels during the interrogation time. This makes the nonlinear interaction negligible and enhances the sensitivity, e.g. for magnetic fields, by orders of magnitude. In the following,



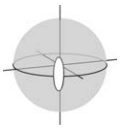

we implement this technique to perform quantum-enhanced magnetometry after swapping the condensate atoms from hyperfine state $|b\rangle = |2, -1\rangle$ to the state $|c\rangle = |1, -1\rangle$ in the electronic ground state manifold of $^{87}$Rb.

For an interferometry sequence with state swapping, we first generate a squeezed state in the levels $|a\rangle$ and $|b\rangle$ using nonlinear one-axis twisting with an evolution time of 20 ms, as shown in chapter 6. A subsequent two-photon pulse ($\phi = 3\pi/2 + 3°$, $\alpha = -75°$) rotates the state onto the phase squeezed axis, where the sensitivity of the interferometer is maximal (see Fig. 7.2). Afterwards, state swapping is implemented by applying a one-photon microwave pulse resonant to the transition between $|b\rangle$ and $|c\rangle$. This transfers the atoms from $|b\rangle$ to $|c\rangle$ with an efficiency of at least 99%, leading to a squeezed atomic state between the internal states $|a\rangle$ and $|c\rangle$. After a hold time $t_{\text{hold}}$ for phase evolution, the population is transferred back to the original levels, where the phase-controlled readout pulse is performed on the magnetically insensitive two-photon transition. It is important to note that the phase interrogation time $t_{\text{int}} = t_{\text{hold}} + 2t_\pi$ of the Ramsey sequence includes both the hold time $t_{\text{hold}}$ and the duration of the two microwave $\pi$ pulses $t_\pi$ during state transfer, which have the same magnetic sensitivity as the evolution in the states $|a\rangle$ and $|c\rangle$. Another interesting aspect of this state swapping is the fact that it inhibits spin-relaxation loss during the hold time in $|a\rangle$ and $|c\rangle$, as both species are in the $F = 1$ manifold of the ground state.

To confirm the applicability for quantum-enhanced measurements, we show that the level of squeezing is maintained during state swapping. For this, we perform an interferometric sequence with $t_{\text{hold}} = 1\,\mu\text{s}$ followed by a tomographic squeezing analysis, summing over the full array of condensates (Fig. 7.3). In the relative analysis, we find the expected sinusoidal shape and $\xi^2_{\text{rel}} = -5.1^{+0.6}_{-0.7}\,\text{dB}$ at the optimum tomography angle, revealing no significant reduction of the squeezing that was obtained before the state swapping sequence. Note that the optimum tomography rotation has an angle that is shorter than the value of $\alpha_{\text{min}_{\text{PS}}} = 90°$ that would be expected for a phase squeezed state, as we experimentally find $\alpha_{\text{min}} = 85°$. This reduction is caused by the nonlinear interaction that is present during the two-photon pulse time of 750 µs, which effectively increases the rotation angle by 5 degrees due to the larger *plasma oscillation* frequency. Also note that for observing squeezing in this scenario, the relative analysis is essential. The shot-to-shot variation of the homogeneous bias field at 9.1 G induces classical phase fluctuations during the state transfer that are much larger than the quantum fluctuations of the squeezed states even for the single lattice sites. Thus, they mask the squeezing in a direct analysis of the system.

A Ramsey fringe is obtained by replacing the readout tomography rotation with a final $\pi/2$ pulse with variable pulse phase $\phi$. We observe a Ramsey fringe visibility of $\mathcal{V} = 0.950(5)$ [Fig. 7.3b)]. Employing the Wineland criterion, we thus find spin squeezing of $\xi^2_{\text{R}} = -4.7(6)\,\text{dB}$ after the state transfer. Without subtraction of detection noise, the relative squeezing reduces to $\xi^2_{\text{rel}} = -3.8(5)\,\text{dB}$, which corresponds to applicable spin squeezing of $\xi^2_{\text{R}} = -3.4(5)\,\text{dB}$. This resource can be directly exploited in a quantum-enhanced magnetometer, as shown in the next section.

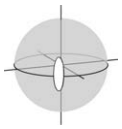

## 7.3. Quantum-Enhanced Magnetometry with Bose-Einstein Condensates

The state transfer described in the previous section enhances the magnetic field sensitivity from $\mathcal{S}_{ab} \approx 1\,\text{Hz/}\mu\text{T}$ (second order Zeeman shift at the operating field of $B_0 = 9.12\,\text{G}$) to $\mathcal{S} \approx 140\,\text{Hz/}\mu\text{T}$ (first order Zeeman shift) – a detailed calculation of these magnetic sensitivities can be found in Appendix A. Additionally, the state swapping strongly reduces the nonlinearity, as there is no Feshbach enhancement of the interaction strength on the final levels $|a\rangle$ and $|c\rangle$ at this field.

With the implementation of a Ramsey sequence, the array of Bose-Einstein condensates can thus be employed as a sensitive detector for magnetic fields. However, in our setup the sensitivity for measuring homogeneous magnetic fields is limited by the shot-to-shot fluctuations of the Feshbach field at 9.1 G, which are on the order of 30 µG. This is much larger than the sensitivity that can be obtained with our detector, which is in principle better than 10 µG for interrogation times in the range of hundreds of microseconds. Thus, the magnetic field sensitivity of the detector cannot be properly characterized from repeated measurements of the homogeneous field, as such a measurement would rather provide a measure for the field stability than for the actual sensitivity of the device.

A different route for extracting the single shot sensitivity is a differential measurement between two independent parts of the BEC array. Such a measurement is sensitive to field gradients, which are comparably stable in our setup, and rejects the fluctuations of the homogeneous bias field. In the previous section, we have shown the feasibility of this approach by demonstrating relative squeezing after the full state transfer sequence, which is the relevant parameter for such a procedure.

For characterizing the sensitivity of our device, we divide our array of BECs into two equal halves. At the output of a Ramsey sequence, a field difference of magnitude $\delta B$ translates into a differential phase $\delta\varphi$ of the Ramsey fringes obtained in the two distinct parts of the array. If the readout is performed with a fixed phase for the final $\pi/2$ pulse, this yields a difference of the two corresponding population imbalances of $\delta z = z_{\text{left}} - z_{\text{right}}$. Assuming equal visibilities $\mathcal{V}$ of the two fringes, we find that $\delta z$ is related to the phase difference $\delta\phi = \phi_{\text{right}} - \phi_{\text{left}}$ between left and right part of the array by

$$\delta z = \mathcal{V}\left[\sin\left(\phi_{\text{left}}\right) - \sin\left(\phi_{\text{left}} + \delta\phi\right)\right] \tag{7.6}$$

$$= -2\mathcal{V}\sin\left(\frac{\delta\phi}{2}\right)\cos\left(\frac{\delta\phi}{2} + \phi_{\text{left}}\right) \tag{7.7}$$

$$= -2\mathcal{V}\sin\left(\phi_{\text{diff}}\right)\cos\left(\phi_{\text{mean}}\right), \tag{7.8}$$

with the mean phase $\phi_{\text{mean}} = (\phi_{\text{left}} + \phi_{\text{right}})/2$ and the deviation of the individual phases $\phi_{\text{diff}} = \delta\phi/2$. The value of $\delta z$ thus depends on the readout phase and is, in the case of small phase shifts, maximal around the zero crossings of the single fringes.

The corresponding difference in the magnetic field is directly connected to the fringe amplitude $\delta z_{\text{max}} = 2\mathcal{V}\sin\left(\frac{\delta\phi}{2}\right)$. Using $\delta\phi = 2\pi\mathcal{S}t_{\text{int}}\cdot\delta B$ with the magnetic field sensitivity $\mathcal{S}$ of the



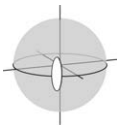

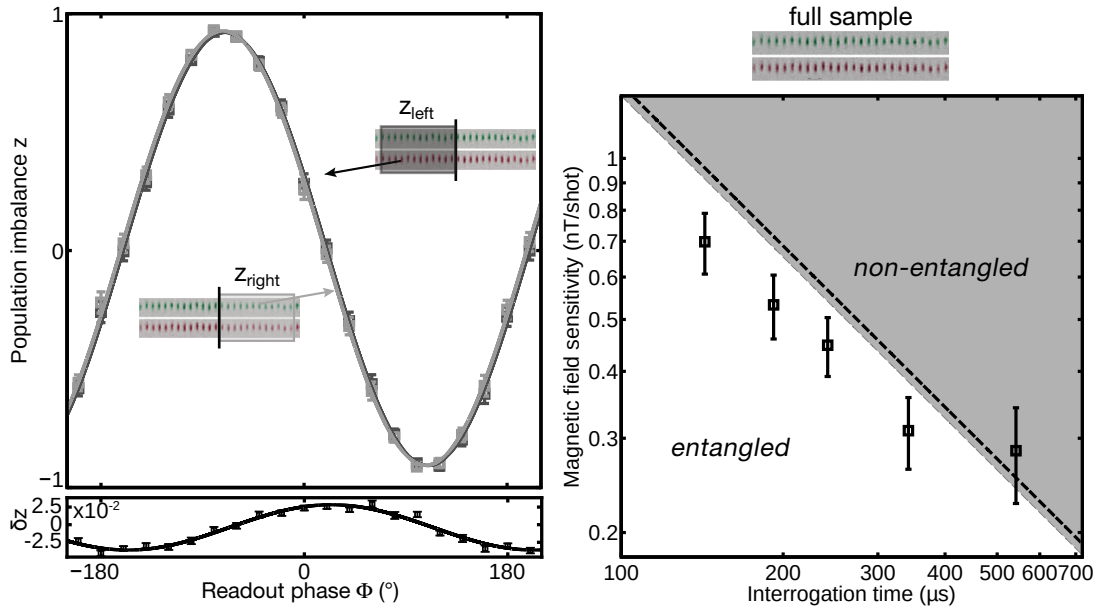


Figure 7.4.: **Ramsey magnetometry beyond the standard quantum limit.** The presence of a magnetic field gradient induces a phase shift between the Ramsey fringes obtained in the left and the right half of the BEC array, as shown for an interrogation time of 342 µs (left panel). The difference of the population imbalances $\delta z = z_{\text{left}} - z_{\text{right}}$ shows a sinusoidal dependence on the readout phase (lower panel). The amplitude $\delta z_{\text{max}}$ of this fringe is proportional to the difference $\delta B$ between the magnetic fields. The magnetic field sensitivity of the sensor (right panel, see Eq. 7.10) can be estimated from the experimentally measured variance of $\delta z$ around the optimal working point, which is at $z_i \approx 0$. Employing the full array, we find quantum enhancement up to interrogation times of 342 µs with a single-shot magnetic field sensitivity of 310(47) pT for this interrogation time. In comparison, the classical limit at this interrogation time for a perfect classical device is 382 pT. The gray shaded area depicts the region which can be reached with classical states, and the dashed black line indicates the best classically obtainable sensitivity including the effect of the detection noise from the absorption imaging procedure.

employed states and the interrogation time $t_{\text{int}}$, we find

$$\delta B = \frac{2 \arcsin\left(\frac{\delta z_{\text{max}}}{2\mathcal{V}}\right)}{2\pi \mathcal{S} t_{\text{int}}}. \tag{7.9}$$

For small fringe amplitudes, we can linearly approximate $\delta z_{\text{max}}$, i.e. $\arcsin\left(\frac{\delta z_{\text{max}}}{2\mathcal{V}}\right) \approx \frac{\delta z_{\text{max}}}{2\mathcal{V}}$ (for the complete expression, see Appendix B). The magnetic field sensitivity $\sigma_B$ around the working point, where the amplitude of the difference fringe is maximal, can then be extracted

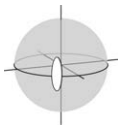

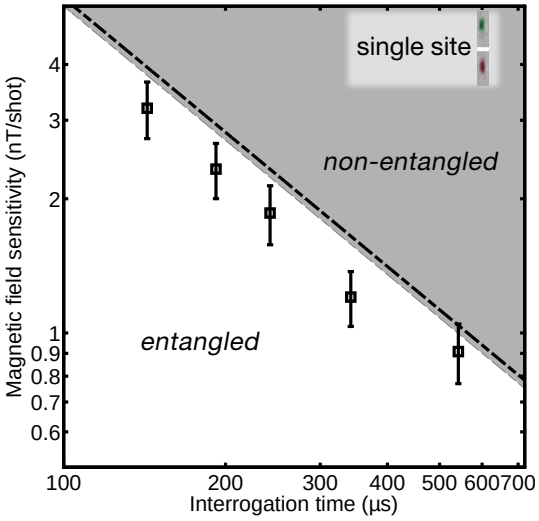


Figure 7.5.: **Field sensitivities for a single lattice site.** We deduce the magnetic field sensitivity for a single lattice site from the differential analysis of the two central wells, and observe quantum enhancement for all interrogation times. After $t_{\text{int}} = 342\,\mu\text{s}$, we find a single-shot sensitivity of 1.20(17) nT, corresponding to 7.2 nT/$\sqrt{\text{Hz}}$.

by error propagation of Eq. 7.9, yielding

$$\sigma_B = \frac{\sigma_{(\delta z_{\max})}}{2\pi \mathcal{V} \mathcal{S} t_{\text{int}}}. \tag{7.10}$$

Using this relation, the gradiometric field sensitivity can be deduced from the experimentally observed variance of $\delta z_{\max}$. The sensitivity for the measurement of magnetic fields in gradiometric operation is determined by the summed noise from the two detectors. Assuming that the corresponding sensitivity can also be attained in combined operation, we can estimate the single-shot magnetic field sensitivity of the full array from these measurements.
In Fig. 7.4, we employ this gradiometric evaluation to analyze the magnetic field sensitivity of the full sample for Ramsey sequences with different interrogation times. The corresponding classical limit attainable with the same atom number is calculated assuming $\text{Var}(z) = 1/\sqrt{N}$ and $\mathcal{V} = 1$, yielding a sensitivity limit of

$$\sigma_{B(SQL)} = \frac{1}{2\pi \mathcal{S} t_{\text{int}} \sqrt{N}}. \tag{7.11}$$

We experimentally find quantum enhancement for interrogation times up to $342\,\mu\text{s}$, with a reduction in variance of up to 41%. For $t_{\text{int}} = 342\,\mu\text{s}$, we find a single-shot sensitivity of $310(47)$ pT compared to the shot noise limit of 382 pT obtained from Eq. 7.11. For longer interrogation times, our method based on the difference $\delta z$ of the two Ramsey fringes no longer yields quantum enhancement, as the fluctuations of the homogeneous offset field translate into a significant reduction of the mean Ramsey contrast (see Fig. 7.6). This decrease is solely due



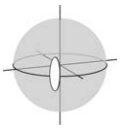

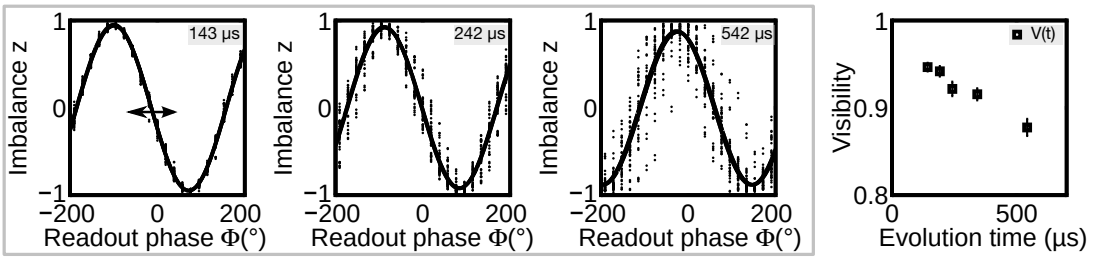


Figure 7.6.: **Visibility reduction due to dephasing.** The fluctuations of the homogeneous bias field translate into shifts of the offset phase $\phi_{\text{mean}}$ that are growing with time. This becomes apparent by the growing spread of the single experimental realizations in the Ramsey fringes after different interrogation times (left panels). As a result, the mean visibility $\mathcal{V}$ of the fringes decreases with interrogation time (right panel).

to shifts of the offset phase $\phi_{\text{mean}}$, and we find that the single shot contrast does not decrease with interrogation time, showing that no significant loss of coherence takes place on the experimental timescales. With a more stable offset field, it would be possible to harness the quantum resources of the input state also at longer interrogation times with the same evaluation method.

The single-shot sensitivity of $310(47)$ pT attained after $342\,\mu$s of phase evolution, combined with our experimental cycle time of 36 s for creating and detecting the BEC array, translates into a sub-shot noise sensitivity of $1.86(28)$ nT/$\sqrt{\text{Hz}}$ for the detection of static magnetic fields with our device. Currently, the sensitivity of the magnetometer is limited by the technical stability of our experiment, which limits the maximum interrogation time. The ultimate physical limitation of this system is the residual nonlinearity between the two levels $|a\rangle$ and $|c\rangle$, which becomes important only on much longer timescales. This can be estimated from the values of the different corresponding scattering lengths, as the strength of this nonlinear interaction is determined by $\chi_{|a\rangle|c\rangle} \propto a_{aa} + a_{cc} - 2a_{ac}$ (see Chapter 2.2.2). According to literature, $a_{aa} = a_{cc} \approx 100.4\,a_B$ [86, 120, 121], where $a_B$ is the Bohr radius. In the $F = 1$ manifold, two atoms can couple to a total spin of either $F = 0$ or $F = 2$. These scattering lengths are calculated to be $a_{F=0} = 101.8(2)\,a_B$ and $a_{F=2} = 100.4(1)\,a_B$. The difference between those scattering lengths is thus theoretically predicted to be $\Delta a_{\text{th}} = -1.38\,a_B$ [122], and was experimentally determined as $\Delta a = -1.07(8)\,a_B$ by analyzing spin-exchange dynamics [123]. In the absence of a Feshbach resonance, all scattering lengths in the $F = 1$ manifold are linear combinations of $a_{ij} = c_1 a_{F=0} + c_2 a_{F=2}$ with the Clebsch-Gordon coefficients $c_1 + c_2 = 1$. This constrains the relevant difference of scattering lengths for the nonlinear interaction to $|a_{aa} + a_{cc} - 2a_{ac}| \leq 2.2\,a_B$.

We can compare this upper bound to the corresponding value on the two-photon transition between $|a\rangle$ and $|b\rangle$. Assuming the parameters of the Feshbach resonance from [89], we find $a_{ab} \approx 91 a_B$ at 9.12 G, and consequently $|a_{aa} + a_{bb} - 2a_{ab}| \approx 14\,a_B$ for the two-photon transition. This corresponds to a nonlinearity of $N\chi_{|a\rangle|b\rangle} \approx 2\pi \times 30$ Hz, and thus the upper bound for the nonlinearity between $|a\rangle$ and $|c\rangle$ can be given as $N\chi_{|a\rangle|c\rangle} \lessapprox 2\pi \times 4$ Hz. Experimentally, it has been shown that interrogation times of 250 ms can be realized with the same set of

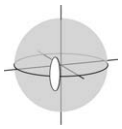

hyperfine states in a similar magnetometry scheme [124], pointing at a nonlinear interaction strength significantly below this upper limit.
The sensitivity of this Ramsey magnetometer can thus be further improved by increasing the interrogation time as well as decreasing the cycle time for the generation of the BEC array. We can project the sensitivity that should be attainable with this technique, assuming the experimentally established interrogation time of 250 ms and a realistic cycle time of 5 s for an all-optical BEC apparatus. With these parameters, a sensitivity of $\sim 1\,\mathrm{pT}/\sqrt{\mathrm{Hz}}$ is feasible, using the current atom number and a probe volume of only $90\,\mu\mathrm{m}^3$.

### 7.3.1. Comparison to Other Magnetometry Techniques

To benchmark the performance of our BEC array magnetometer, we now compare the attained sensitivity to the corresponding values obtained with comparable state-of-the-art devices.
There are numerous different magnetometry techniques, covering a wide range of sensitivities, spatial resolution and frequencies at which the fields are measured. Fig. 7.7 shows the sensitivities and probe volumes for a number of state-of-the-art devices employing different measurement techniques, along with the frequency at which they operate. In the following, we will give a short overview over these different techniques which are employed in precision magnetometry.

Nanometer scale resolution can be achieved with sensors building on nitrogen vacancy centers (*NV centers*) in diamond. In these diamond defects, a nitrogen atom substitutes a carbon atom, leading to a lattice vacancy. The ground state of this system constitutes a spin-1 manifold. Due to the Zeeman splitting of the different spin states, this can be used as an effective two-level system, which can be employed for Ramsey sequences. The relative population of the two levels can be read out via the spin-dependent fluorescence strength of an optical transition to an excited state. For static fields, the sensitivity of NV centers is limited by the dephasing caused by other defects and the presence of $^{13}$C impurities in the diamond crystal. The dephasing time is typically on the order of milliseconds, limiting the DC sensitivity on the $\mu\mathrm{T}/\sqrt{\mathrm{Hz}}$ level [56]. It can be extended by applying spin-echo sequences, which allow the detection of AC fields with sensitivities down to $2.5\,\mathrm{nT}/\sqrt{\mathrm{Hz}}$ [130].
Optical magnetometers based on vapor cells allow to reach sensitivities down to $160\,\mathrm{aT}/\sqrt{\mathrm{Hz}}$ [134], but employ much larger probing volumes (typically $\approx$ cm$^3$). These magnetometers use optical pumping to create a long-lived spin orientation in a vapor typically consisting of alkali atoms. In the presence of a magnetic field, the atoms undergo Larmor precession, which modifies their optical absorption and dispersion properties. This can be used for the precise determination of the magnetic field inside the vapor cell.
The precision of such magnetometers is ultimately limited by collisions with the walls of the glass cell, which destroy the coherence. Even though this favors larger cell sizes, sensitivities of down to $70\,\mathrm{fT}/\sqrt{\mathrm{Hz}}$ have been attained for a microfabricated vapor cell with a volume of just 6 mm$^3$ [132].
One important aspect for both NV centers and optical vapor cell magnetometers is that they allow the detection of magnetic fields at ambient temperatures. This is technologically im-



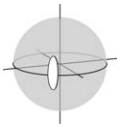

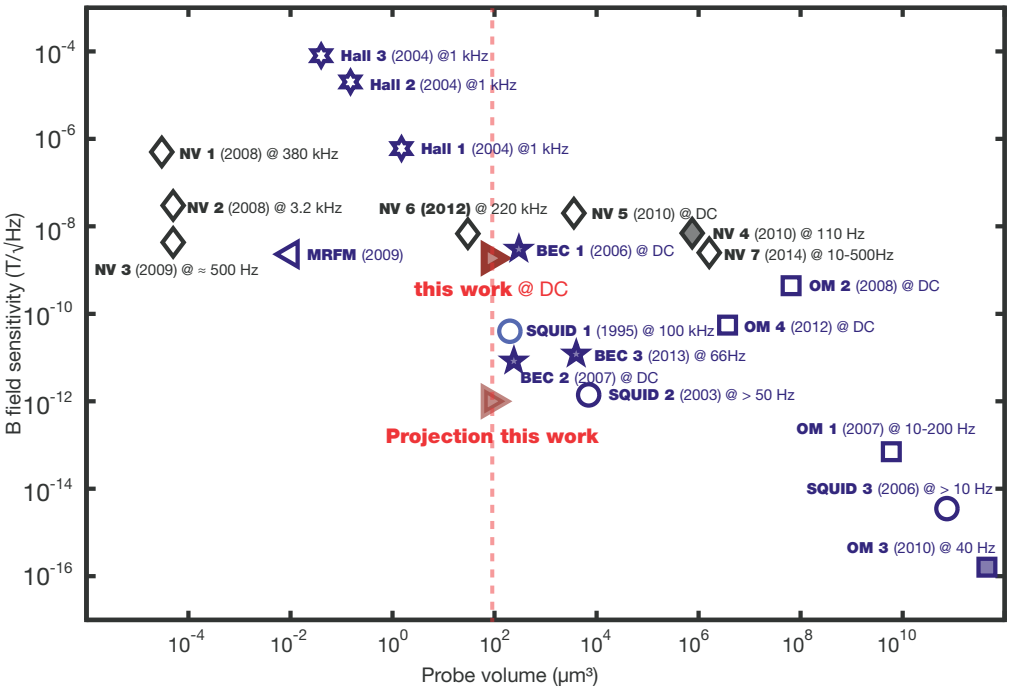


Figure 7.7.: **Sensitivity for different types of state-of-the-art magnetometers vs. probe volume.** Different magnetometry techniques cover a wide range of sensitivities, field frequencies and offer a large variety in spatial resolution. NV centers can achieve nanoscale spatial resolution and sensitivities down to a few nT/$\sqrt{\text{Hz}}$ [125] (NV1,2) and [126, 127, 128, 129, 130] (NV 3-7), which is also the case for magnetic resonance force microscopy (MRFM) [131]. Best overall sensitivities at the cost of lower spatial resolution are attained with optical vapor cell and cold atom magnetometers (OM 1-4) [132, 133, 134, 37] and large SQUIDs (SQUID 2,3) [135, 136]. In the intermediate regime, Bose-Einstein condensates (BEC1, 2 and 3) [137, 124, 138], Hall probes 1-3 [139] and micro-SQUIDs (SQUID 1 [140]) operate at spatial resolutions of a few up to tens of micrometers. The magnetometer discussed in this thesis (red triangles) is competitive with other state-of-the-art devices using similar probe volume, and the projected performance would surpass the sensitivities of these devices. Filled symbols indicate that the given sensitivity was obtained using differential field analysis, which suppresses common mode field fluctuations.

portant and advantageous e.g. for the detection of magnetic fields in living cells [141], which requires short distances between probe and detector.
Similar detection schemes can also be employed using cold and ultracold atomic systems, which have the advantage of larger coherence times and slow diffusion and thus an increased spatial resolution in the micrometer range. In this context, a sensitivity of down to 8.3 pT/$\sqrt{\text{Hz}}$ has been shown with a Bose-condensed Rubidium cloud by monitoring the Larmor precession

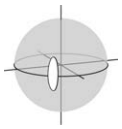

with non-destructive phase contrast imaging [124]. A spin squeezed magnetometer with cold thermal atoms in an optical trap achieved a sensitivity of 55 pT/$\sqrt{\text{Hz}}$ with a millimeter sized probe volume [37]. Microwave magnetic fields have been detected with a quantum-enhanced sensitivity of 77 pT/$\sqrt{\text{Hz}}$ in a probe volume of just 20 µm$^3$ with a Bose-condensed scanning probe interferometer [48].
Ultracold atomic systems on atom chips have been employed for ultracold atom magnetic field microscopy [137]. Here, the modification of the trapping potential for magnetically trapped atoms which is imposed by spatially inhomogeneous offset fields imprints the structure of the field onto the atomic density. Such a technique can be used to study the shape and transport properties of wires with a spatial resolution of 3 µm and sensitivities down to a few nT/$\sqrt{\text{Hz}}$ [114]. This technique relies on changes of the absolute value of the field, and the magnetic trapping makes operation in vector mode unfeasible, as this would require a tunable orientation of the trapping fields.
Superconducting quantum interference devices (SQUIDs) also operate at cold temperatures and require cryogenic cooling. These detectors are based on superconducting loops containing Josephson junctions and build on the magnetic flux quantization inside the loop. The sensitivity of these devices depends on the area enclosed by the loop. They are built from micro- and nanoscale to centimeter sizes and can reach sensitivities on the order of fT/$\sqrt{\text{Hz}}$ for the large scale devices [136] and in the range of pT/$\sqrt{\text{Hz}}$ for devices with tens of microns in diameter [140]. In contrast to optical magnetometry techniques, SQUIDs only measure relative fields, but are not limited to small absolute values.

In comparison to these state-of-the-art devices, the spin squeezed ultracold atomic magnetometer presented in this thesis offers a sensitivity on a competitive level for devices operating on the micrometer scale. The projected sensitivity of 1 pT/$\sqrt{\text{Hz}}$ shows that it is feasible to outperform all current state-of-the-art devices by increasing the interrogation time and decreasing the experimental cycle time. This offers inter alia prospects for increasing the sensitivity in high-resolution magnetic field microscopy, where squeezing allows to enhance the performance on small scales. Also, the optical trapping allows for vector operation of our device by changing the direction of the bias field. This could be straight-forwardly implemented in our setup with two additional sets of coils perpendicular to our current bias field configuration.

## 7.4. Gradiometric Measurements with a Bose-Condensed Sensor

In the previous section, we have employed a differential analysis of two independent parts of the lattice as a tool to characterize the magnetic field sensitivity of the full BEC array. We will now discuss the sensitivity of this device for measurements in a gradiometric configuration, and present a precise measurement of the magnetic field gradient along the atomic cloud. Finally, we will discuss a gradiometric evaluation method based on ellipse fitting and its applicability to our measurements.



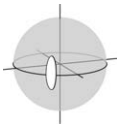

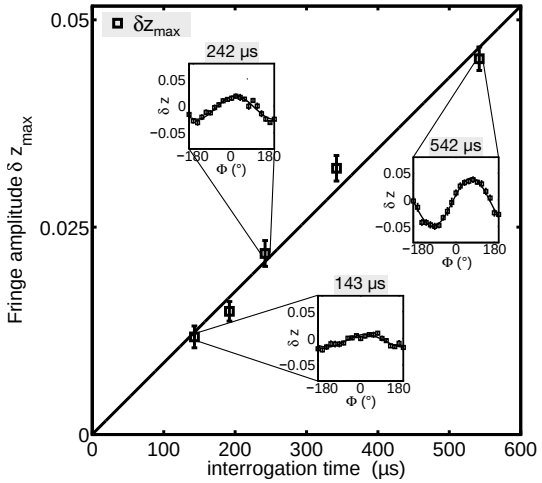


Figure 7.8.: **Fringes in $\delta$z for different Ramsey interrogation times.** The difference in the population imbalances $\delta z$ between the left and right part of the lattice shows a sinusoidal dependence on the readout phase, with an amplitude which grows linearly with interrogation time (black squares in main plot). This is expected for a time-independent field gradient, which translates into linear growth of the accumulated differential phase $\delta\phi = 2\pi\mathcal{S}\delta B \cdot t_{\text{int}}$. The insets show three exemplary fringes of $\delta z$ for different interrogation times. The phase $\phi_{\text{mean}}$ of the fringes shifts for the different evolution times due to an homogeneous overall detuning of the one-photon coupling for the given bias field.

### 7.4.1. Gradiometric Sensitivities

As shown in Eq. 7.9, in a Ramsey sequence a difference in the total magnetic field of $\delta B$ shows up as a sinusoidal oscillation in the difference of the population imbalances $\delta z(\phi)$. As the amplitude of this oscillation is related to the value of the field difference, and the distance between the detectors is known, we can hence precisely determine the magnetic field gradients in our experimental system.

Fig. 7.8 shows exemplary fringes of $\delta z(\phi)$ for different interrogation times, employing the full BEC array divided into two parts of equal size. The fringe amplitude $\delta z_{\text{max}}$, which is proportional to the phase difference accumulated between left and right part of the BEC array, grows linearly with interrogation time, as expected for a time-independent field gradient. Note that the phase of the fringes in $\delta z(\phi)$ shifts for the different evolution times due to a homogeneous detuning, which leads to a temporal evolution of the mean phase $\phi_{\text{mean}}$ of the individual Ramsey fringes.

The gradiometric sensitivity depends not only on the magnetic field sensitivity of the two sensors, but also on the baseline length $d$ between them. The magnetic field gradient can be deduced from the fringe amplitude $\delta z_{\text{max}}$ (in analogy to Eq. 7.9) and the baseline length,

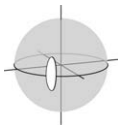

yielding

$$\frac{\partial B}{\partial x} = \frac{2\arcsin\left(\frac{\delta z_{\text{max}}}{2\mathcal{V}}\right)}{2\pi\mathcal{S}t_{\text{int}}d}. \tag{7.12}$$

Analogous to section 7.3, this results in a gradiometric sensitivity around the optimal working point of

$$\sigma_{\text{grad}} = \frac{\sigma_{(\delta z_{\text{max}})}}{2\pi\mathcal{V}\mathcal{S}t_{\text{int}}d}. \tag{7.13}$$

For a spatially homogeneous gradient field, the gradiometric sensitivity increases linearly with the baseline length $d$. However, in the case of spatial inhomogeneities, this increased sensitivity comes at the price of decreased spatial resolution.
If we use single lattice sites as the magnetic field detectors for the evaluation of the gradient, the relevant baseline length $d$ is simply given by the distance between the individual lattice sites, i.e. $d = n \cdot 5.5\,\mu\text{m}$ for a separation of $n$ sites. The situation is more complicated in the case of summed ensembles containing several lattice sites, which can have spatially inhomogeneous atom number distributions. Here, for spatially homogeneous gradients (which is the case in our setup, see Fig. 7.10), the relevant baseline length is given by the distance between the centers of gravity of the two clouds. Taking into account the individual atom numbers $N_{i,j}$ of the different sites, this yields

$$d = \left(\frac{\sum_{\text{left wells}} n_i \cdot N_i}{\sum_{\text{left wells}} N_i} - \frac{\sum_{\text{right wells}} n_j \cdot N_j}{\sum_{\text{right wells}} N_j}\right) \cdot 5.5\,\mu\text{m}. \tag{7.14}$$

We analyze the the gradiometric field sensitivity for these two different approaches. At first, we examine the sensitivity using single lattice sites with increasing distance, starting with adjacent wells in the center of the array and ending with the maximum separation given by the size of the cloud. The results are shown in Fig. 7.9 for an evolution time of 342 µs, analyzed around the optimal working point of the Ramsey fringe (i.e. around $z_{\text{max}}$). We find that the sensitivity increases for larger distances between the employed lattice sites and is below the standard quantum limit (two detectors with $N/2$ atoms, $\mathcal{V} = 1$) for all distances. The deviation from the expected linear increase is due to the decreasing atom number at the edges of the cloud, which leads to larger fluctuations in $\delta z_{\text{max}}$ corresponding to $\sigma_{z_{\text{max}}} \propto 1/N_{\text{left}} + 1/N_{\text{right}}$ and thus reduces the differential field sensitivity.
We can increase the magnetic field sensitivity of the two detectors by summing the atom numbers of several lattice sites. The baseline length $d$, calculated using Eq. 7.14, increases with the number of summed sites, and so does the gradiometric sensitivity. One has to keep in mind that the maximum attainable baseline length $d$ for the summed ensemble is smaller than in the case of single lattice sites. Still, the gain in magnetic field sensitivity overcompensates this and yields a better sensitivity for the sum of many BECs in comparison to the analysis of two single lattice sites at the edges of the array, as can be seen in Fig. 7.9.
As the squeezing is scalable up to the full ensemble size, we find a performance beyond the standard quantum limit for all summing sizes. Optimal sensitivity is attained if we divide the array in two parts and sum over all the sites in both halves, yielding $\sigma_{\text{grad}} = 12(2)\,\text{pT/µm}$ with a resolution of 50 µm for a single experimental run. Operating at the best attainable spa-



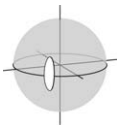

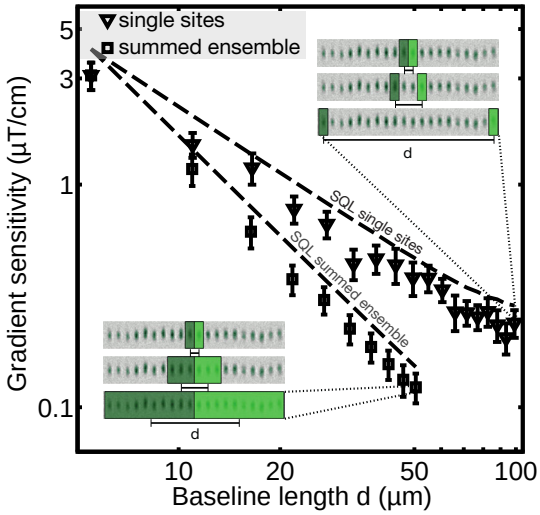


Figure 7.9.: **Gradiometric sensitivity for $t_{int} = 342\,\mu s$.** In the relative analysis of single lattice sites (triangles), the sensitivity for magnetic field gradients increases with baseline length $d$, and surpasses the corresponding classical limit (SQL, upper dashed line) at all distances. The deviation from the expected linear behavior at large $d$ is caused by the decreasing atom number toward the edges of the array. Summing over several adjacent sites further increases the gradient sensitivity (squares) at the expense of degraded spatial resolution for the individual sensors. The summed ensembles also beat the corresponding standard quantum limit (lower dashed line). We find an optimal gradient sensitivity of $\sigma_{\text{grad}} = 12(2)$ pT/μm when all lattice sites are employed.

tial resolution of $5.5\,\mu$m using individual lattice sites, we achieve a single-shot sensitivity of $310$ pT/μm.
This sensitivity is on a competitive level with other gradiometers operating at this length scale, which achieved for example $20$ pT/μm with a spatial resolution of $50\,\mu$m in a cold atom gradiometer [142], or $\sigma_{\text{grad}} \approx 400$ pT/μm and a resolution of $3\,\mu$m with ultracold atoms [137].

## 7.4.2. Measurement of the Magnetic Field Gradient in our Setup

As shown in the previous paragraphs, the differential Ramsey technique allows the precise determination of the gradient of a static magnetic field in our system. From the differential fringes shown in Fig. 7.9, we can directly extract the strength of these gradients by use of Equation 7.12. Employing the full array, we find an average value of $\frac{\partial B}{\partial x} = 19.6(6)$ pT/μm. This small residual gradient is due to magnetic materials in the surroundings of the experiment, such as an ion pump, which have been partially compensated by careful positioning of permanent magnets in the vicinity of the science cell.
Note that these measurements are effectively vectorial measurements, as the large bias field of 9.1 G strongly reduces the sensitivity of our magnetometer in the orthogonal directions

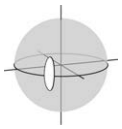

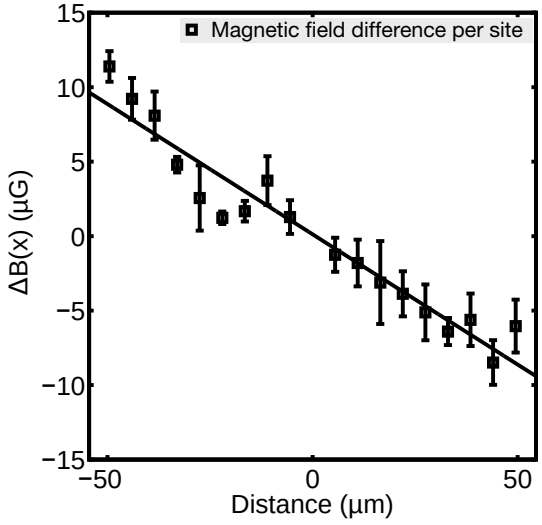


Figure 7.10.: **Magnetic field measurement at varying distances to the center of the array.** Evaluating the magnetic field at different positions of the cloud by referencing the single lattice sites on the central well of the array, we do not observe significant deviations from a linear behavior. This indicates that higher order terms are negligible over the length scale of our array. The absolute value of the field changes by less than 20 μG over the full extension of the cloud.

and thus determines the sensitive axis. This is because the Ramsey sequence is sensitive to the Zeeman shift of the atoms, which is proportional to the absolute value of the field $|\mathbf{B}| = \sqrt{B_x^2 + B_y^2 + B_z^2}$. Assuming that the bias field is in $z$ direction, i.e. $\mathbf{B} = (B_x, B_y, B_z) = (0, 0, B_0)$, we find that the absolute value of the field depends on the components of the gradients $\frac{\partial B_i}{\partial x}$ in $x$ direction (i.e. along the lattice) as

$$|\mathbf{B}(x)| \approx B_0 + \frac{\partial B_z}{\partial x} x + \frac{\left[\left(\frac{\partial B_y}{\partial x}\right)^2 + \left(\frac{\partial B_x}{\partial x}\right)^2\right]}{2B_0} x^2. \tag{7.15}$$

Components that are orthogonal to the bias field thus contribute only quadratically and are suppressed by a factor of $2B_0$ compared to the gradient which is aligned with the offset field. In our experiment, we do not observe a significant deviation from a linear behavior of the measured field at varying distances (see Fig. 7.10). Note that in principle, the full vectorial behavior can be mapped out by changing the direction of the bias field.

### 7.4.3. Beyond Differential Fringe Analysis: Ellipse Fitting

The extraction of the magnetic field gradient based on the differential analysis of the two Ramsey fringes fails in the case of strong fluctuations of the underlying homogeneous bias field. This is because such variations lead to shifts in the offset phase $\phi_{\text{mean}}$ and thus reduce



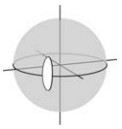

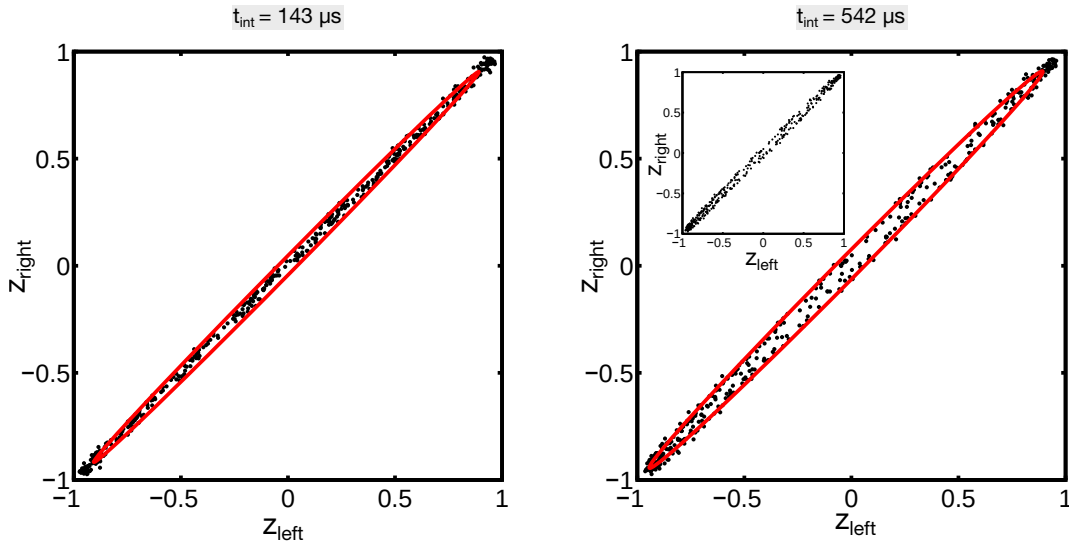


Figure 7.11.: **Elliptical fits for gradiometric evaluation.** In principle, the gradiometric measurement can be evaluated by fitting an ellipse to the interdependence of the two sinusoidal signals $z_{\text{left}}$ and $z_{\text{right}}$. The data points and the corresponding fitted ellipses are shown for interrogation times of $t_{\text{int}} = 143\,\mu\text{s}$ (left panel) and $542\,\mu\text{s}$ (right panel), for which a small phase shift between the signals becomes apparent by the deviation from the linear behavior (see inset without fit). In the current working regime, the elliptical fits do not yield reliable results due the presence of amplitude noise. This broadens the short axis of the ellipse, and thus leads to a smaller eccentricity of the fitted ellipse and an overestimation of the acquired phase [143]. Note that the long axis of the ellipse remains constant for the longer interrogation time, which indicates that the loss of fringe contrast is solely due to dephasing.

the visibility $\mathcal{V}$ of the fringes. In the extreme case that the fluctuations of $\phi_{\text{mean}}$ are so strong that the phase is shifted over the full oscillation period, the resulting signal in $\delta z$ for many repetitions of the experiment vanishes. However, the correlations between the measurements of the two parts of the cloud still exist, but cannot be extracted with this differential method.
An alternative, well-established approach for gradiometric phase estimation in the presence of large common-mode fluctuations is the so-called *ellipse-fitting method* [143], which was introduced in the context of gravity gradiometry in the group of Mark Kasevich.
The ellipse-fitting method relies on the elliptic relationship of the two sinusoidal signals $z_{\text{left}}$ and $z_{\text{right}}$. Plotting the results of $z_{\text{left}}$ for many realizations against the corresponding outcome for $z_{\text{right}}$ yields an ellipse whose eccentricity is related to the phase shift $\delta\phi$ between the two signals. In the case of $\delta\phi = 0$, this collapses onto a straight line. Quantitatively, the relative phase can be extracted using an elliptical fit of the form

$$A \cdot z_{\text{right}}^2 + B \cdot z_{\text{left}} z_{\text{right}} + C \cdot z_{\text{left}}^2 + D \cdot z_{\text{right}} + E \cdot z_{\text{left}} + F = 0 \tag{7.16}$$

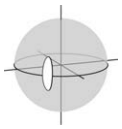

and using $\delta\phi = \arccos(-B/2\sqrt{AC})$ [143]. In contrast to the differential fringe analysis, this method requires multiple shots for evaluation and is typically applied after several hundreds of measurements.

Fig. 7.11 shows the elliptical shapes obtained from our data for interrogation times of $t_{\text{int}} = 143$ and $542\,\mu\text{s}$. As we work in the limit of small phase differences, the data points almost collapse onto a line and show a deviation only for larger interrogation times. The length of the long axis of the ellipse remains constant, indicating that the decrease of the Ramsey fringe visibility at longer evolution times is solely due to the dephasing caused by common mode fluctuations, as also indicated in Fig. 7.6.

However, as our gradiometer operates in the regime of small phase shifts $\delta\phi \approx 0$, the ellipse fitting routine does not yield reliable results due to the presence of amplitude noise [143], which is in our case mainly caused by the projection noise of the samples. This amplitude noise broadens the short axis of the ellipse and thus leads to an overestimation of the acquired phase. Also, the elongated nature of the squeezed states leads to quantum enhancement in only in a specific range of phases of the Ramsey fringes. As the ellipse fitting method requires sampling over many phases, quantum advantage is most likely lost during this process. Thus, this alternative approach can in principle be employed in our setup even for interrogation times where the fringe visibility is strongly reduced by common mode fluctuations of the bias field. However, it is not reliable for the currently employed parameters that yield small phase shifts, and cannot straight-forwardly exploit the full quantum advantage that we find with the differential fringe method.



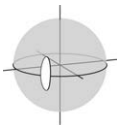

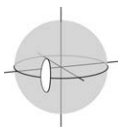

# 8. Outlook

In this thesis, we have demonstrated a scheme for scaling the atom number of spin squeezed states in Bose-Einstein condensates to macroscopic system sizes. In addition, we have shown that this larger quantum resource can be applied for high-precision magnetometry by swapping the population to different internal levels of the atoms.

We experimentally studied two different diabatic schemes for the generation of highly entangled spin squeezed states in the internal levels of an interacting binary Bose-Einstein condensate in a single spatial mode. An experimental and theoretical analysis was presented for both the temporal evolution and the atom number dependence of the well-established *one-axis twisting* scheme and also for a new method exploiting an unstable fixed point in the system's classical phase space, the *bifurcation squeezing* scheme. We could show that both scenarios allow the generation of spin squeezed states containing a few hundred atoms. Under optimal conditions, we found a fluctuation suppression of more than 7 dB with little dependence on the atom number. This is an important prerequisite for our scaling procedure in the presence of atom number inhomogeneities.

Our scheme for scaling up the atom number employs an array of up to 30 independently squeezed small condensates, which we prepare by use of a 1D lattice. This method allows increasing the number of atoms and maintaining the well-controlled generation scenario on the single lattice sites at moderate densities at the same time, avoiding enhanced losses or uncontrolled multi-mode dynamics.
The upscaling was demonstrated for both squeezing schemes and yielded number squeezing of up to $\xi_{\mathrm{N}}^2 = -3.3(4)$ dB for $10^4$ particles using bifurcation squeezing, and $\xi_{\mathrm{N}}^2 = -1.5(6)$ dB with the one-axis twisting scenario. The limiting factor for the scalability of number squeezing, which was extracted from the fluctuations of repeated measurements, was shown to be phase noise resulting from technical fluctuations that were mainly caused by the residual jitter of the magnetic bias field. Our analysis indicates that the influence of technical noise sources can be further suppressed by use of an optimized spin-echo sequence that accounts for the changes in the rotation angle, which are caused by the inherent nonlinearity during the pulse.
To get direct access to the quantum fluctuations of the states, we introduced a differential analysis which quantifies the relative fluctuations between two independent parts of the BEC array. This method is insensitive to technical fluctuations of homogeneous fields, and thus directly reveals the underlying quantum resources of the state. Taking into account the visibility that can be attained in an interferometric measurement, the corresponding relative squeezing parameter determines the sensitivity of a gradiometric measurement. For our upscaled resource, we found $\xi_{\mathrm{rel}}^2 = -5.3(5)$ dB of relative squeezing and a visibility of $\mathcal{V} = 0.95$. With-

out subtraction of detection noise, this resulted in metrologically relevant spin squeezing of $\xi_S^2 = -3.8(5)$ dB, which indicates the directly employable quantum resource of the full 1D array.

This applicability was finally demonstrated with the implementation of a magnetic gradiometer operating beyond the classical precision limit. In the employed scheme, the crucial step was the transfer of the squeezed states to a different set of hyperfine levels in the ground state manifold of Rubidium. The magnetometer is based on a modified Ramsey sequence that exploits the quantum resource of the squeezed states, and combines a spatial resolution of down to 5.5 µm with a high magnetic field sensitivity. It might thus improve magnetic field microscopy, which can for example be employed for surface characterization and flow patterns in solid state devices [114].

The sensitivity of our device might be further increased by extending the lattice geometry to two or even three dimensions, increasing the number of squeezed atoms by orders of magnitude. Additionally, a reduction of the technical fluctuations should allow enlarging the interrogation times to hundreds of milliseconds, until the residual nonlinearity of the transition comes into play.
Going further, the experimental demonstration of state swapping with a squeezed ensemble opens up new possibilities for applications, as the quantum resource can in principle be transferred to arbitrary other levels. Each set of levels is most sensitive to a specific quantity – for the chosen levels $|a\rangle$ and $|c\rangle$, this was the static magnetic field. Other levels which are insensitive to magnetic fields can be used for the detection of light shifts or for the implementation of spin squeezed atomic clocks [57], even though one has to keep in mind that the large collisional shifts make Bose-Einstein condensates a rather unlikely system for an accurate high-performance clock. Transfer to motional states of the BEC could be implemented by use of Raman beam splitters for state swapping. These spin squeezed motional states could be employed for the precise measurement of external forces, such as gravitation and other accelerations, using atom interferometry [55, 54, 53, 8]. The enhanced sensitivity of such measurements might enable improved precision tests of general relativity [112] or the detection of gravitational waves [111].

Apart from the practical applicability of these methods for generating large entangled ultracold ensembles, the BEC array with many individually entangled subsystems and tunable inter-site interaction is also ideally suited for the investigation of other fundamental questions. In the single-mode situation of the individual sites, further studies of the bifurcated system could be able to reveal a divergence in the density of states and consequently yield deeper insights into the physics of excited state quantum phase transitions [144]. In the limit of vanishing potential barriers, the instability of the resulting quasi one-dimensional system and the connected quantum phase transition offer prospects for accessing the role of entanglement in quantum phase transitions [145, 146].

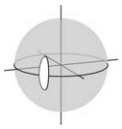

For a two-well system, there are proposals to generate EPR entanglement by combining internal and external squeezing procedures [147, 148, 149]. Studies employing the full array of BECs which are independently entangled in the internal degree of freedom should allow investigations of the spread of quantum correlations [150, 151] in the continuous variable limit. This experimental system could thus provide a basis for addressing a multitude of exciting questions in the future, both from the fundamental physics perspective and in terms of practical applications.



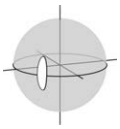

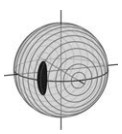

# A. Calculation of the Magnetic Sensitivities

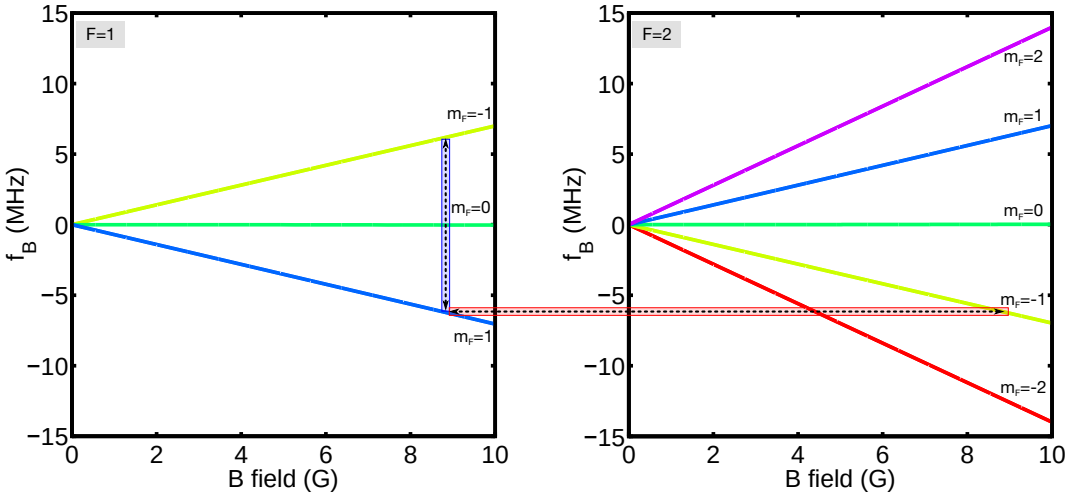


Figure A.1.: **Magnetic field dependent energy shifts for $^{87}$Rb.**. The magnetic field dependent energy shifts are calculated by use of the Breit-Rabi formula with the parameters from table A.1 for the $F = 1$ (left) and the $F = 2$ (right) hyperfine manifolds of the ground state of $^{87}$Rb. The linear shifts for the same magnetic quantum number $m_F$ are opposite for $F = 1$ and $F = 2$. For obtaining the magnetic sensitivities on the two-photon transition (between $|a\rangle = |F = 1, m_F = 1\rangle$ and $|b\rangle = |2, -1\rangle$, red dotted arrow) and during the interferometric sequence (between $|a\rangle$ and $|c\rangle = |1, -1\rangle$, blue dotted arrow), we calculate the derivative of the corresponding frequency shifts on these transitions.

The magnetic field dependence for the energies of the hyperfine levels of the electronic ground state of $^{87}$Rb can be calculated using the Breit-Rabi formula [152]. For Rubidium, this is given by

$$E_{F,m_F}(B) = g_I m_F \mu_B B + (-1)^F \cdot A_{\text{hfs}} \sqrt{1 + m_F x + x^2} \tag{A.1}$$

where $A_{\text{hfs}}$ denotes the hyperfine splitting of the different substates $F$, $m_F$ is the magnetic quantum number, $g_I$ is the nuclear g factor, $\mu_B$ is the Bohr magneton, $B$ is the magnetic field and $x = \mu_B B \cdot (g_J - g_I)/(2A_{\text{hfs}})$. Here, $g_J$ denotes the fine structure Landé g-factor.

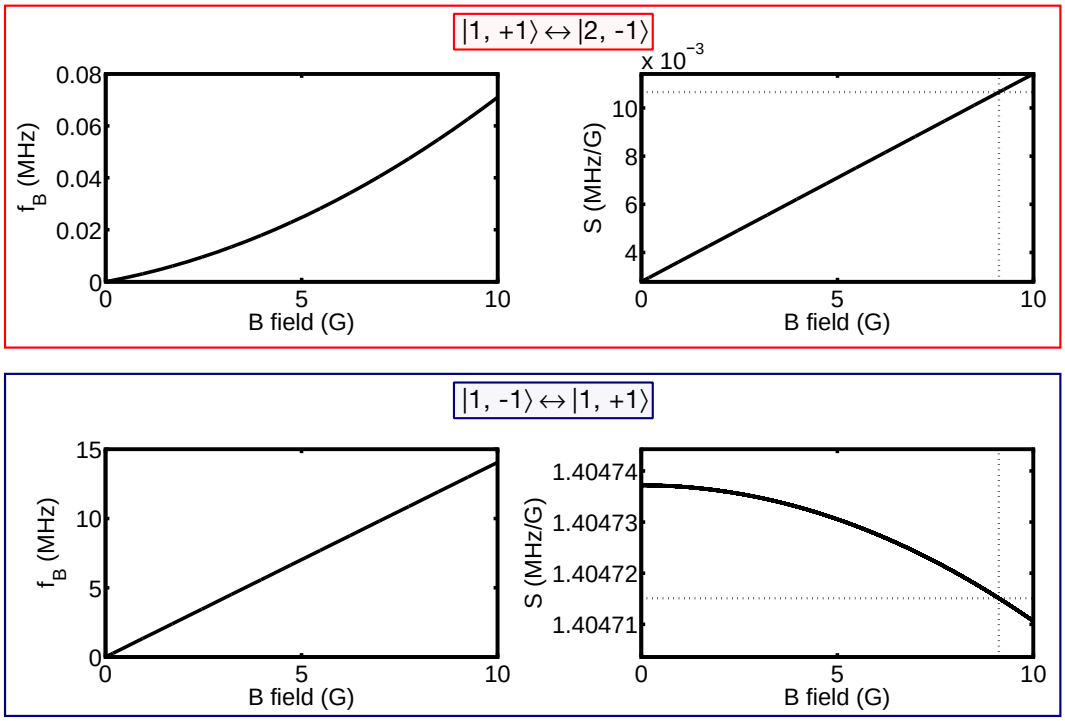


Figure A.2.: **Magnetic field sensitivity $\mathcal{S}$.** The magnetic field sensitivity can be obtained by calculating the frequency shifts on a chosen transition (left panels) and linearizing this shift with a derivative (right panels). This is done for our two-photon transition between $|a\rangle = |1, 1\rangle$ and $|b\rangle = |2, -1\rangle$ (upper panel) and the levels used during the magnetometry sequence, $|a\rangle$ and $|c\rangle = |1, -1\rangle$. The dotted lines indicate the working field of 9.12 G, where we find a sensitivity of $\mathcal{S}_{ab} = 10.654\,\text{kHz/G}$ for the two-photon transition and $\mathcal{S} = 1.404715\,\text{MHz/G}$ for the levels used in the Ramsey magnetometer.

Fig. A.1 shows the magnetic field dependence of all Zeeman sublevels in the ground state, calculated with the parameters stated in Table A.1. The linear shifts of the magnetic sublevels in the $F = 2$ manifold are in opposite direction compared to the dependence of the $F = 1$ manifold.

For our experiments, we are especially interested in the sensitivities of two sets of hyperfine states: The two-photon transition between the levels $|a\rangle = |F = 1, m_F = 1\rangle$ and $|b\rangle = |2, -1\rangle$ (marked in red), which both have the same linear Zeeman shift, and the levels $|a\rangle$ and $|c\rangle = |1, -1\rangle$ which are employed in the magnetometry sequence (marked in blue). The shifts of the transition frequencies for different magnetic fields, obtained from the difference of the Breit-Rabi results, are shown in Fig. A.2, along with the corresponding linearized magnetic sensitivities $\mathcal{S}$. As the levels $|a\rangle$ and $|b\rangle$ only shift quadratically, we find for a field of 9.12 G a magnetic sensitivity of $\mathcal{S}_{ab} = 0.010654\,\text{MHz/G}$. The shifts are much larger for the levels $|a\rangle$ and $|c\rangle$ which are employed in the magnetometry sequence, as their linear shift is in opposite direction. Here, the magnetic sensitivity at 9.12 G is found to be $\mathcal{S} = 1.404715\,\text{MHz/G}$.

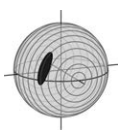

| Parameter name | Value | |
|---|---|---|
| $\mu_B$ | $1.399\,624$ MHz/G | [153] |
| $g_I$ | $-0.000\,995\,141\,4$ | [154] |
| $g_J$ | $2.002\,331$ | [155] |
| $A_{\mathrm{HFS}}$ | $\frac{1}{2} \cdot 6834.682610\,904\,29$ MHz | [156] |

Table A.1.: List of constants that were employed for the calculation of the magnetic field sensitivity.



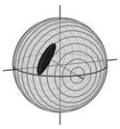

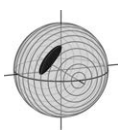

# B. Exact Calculation of Gradiometric Sensitivity from Two Ramsey Fringes

In the following, we will give a derivation of the exact expression for the gradiometric sensitivity without the assumptions of equal population imbalances $z_1 = z_2 = 0$ and visibilities $\mathcal{V}_1 = \mathcal{V}_2$. We will start with the sensitivity calculation of a single Ramsey fringe. In this case, for a Ramsey fringe with visibility $\mathcal{V}_1$, we find a sinusoidal connection between imbalance $z_1$ and the corresponding phase $\phi_1$

$$z_1 = \mathcal{V}_1 \sin(\phi_1). \tag{B.1}$$

The phase $\phi_1$ can thus be estimated by inversion of Eq. B.1, yielding

$$\phi_1 = \arcsin\left(\frac{z_1}{\mathcal{V}_1}\right). \tag{B.2}$$

Taking into account the projection noise $\mathrm{Var}(z_1)$, we find the phase sensitivity by error propagation of Eq. B.2, yielding

$$\mathrm{Var}(\phi_1) = \left(\frac{\partial \phi_1}{\partial z_1}\right)^2 \cdot \mathrm{Var}(z_1) = \frac{1}{\mathcal{V}_1^2 - z_1^2} \cdot \mathrm{Var}(z_1), \tag{B.3}$$

where we made use of the identity $\frac{\partial}{\partial x}\arcsin\left(\frac{x}{y}\right) = \frac{1}{y\sqrt{1-x^2/y^2}}$.
We can proceed analogously in the case of differential phase estimation from two fringes $z_1 = \mathcal{V}_1 \sin(\phi_1)$ and $z_2 = \mathcal{V}_2 \sin(\phi_2)$, where we want to estimate the differential phase $\delta\phi = \phi_2 - \phi_1$ from the difference in the population imbalances $\delta z$ and the imbalance $z_1$. We can obtain the differential phase by inverting identity

$$\delta z = \mathcal{V}_2 \sin(\phi_1 + \delta\phi) - \mathcal{V}_1 \sin(\phi_1), \tag{B.4}$$

yielding

$$\delta\phi = \arcsin\left(\frac{\delta z - z_1}{\mathcal{V}_2}\right) - \arcsin\left(\frac{z_1}{\mathcal{V}_1}\right). \tag{B.5}$$

The full expression for the differential phase sensitivity is then obtained from error propagation of Eq. B.5 in respect to $\delta z$ and $z_1$. For the first part, we find

$$\left(\frac{\partial \delta\phi}{\partial \delta z}\right)^2 \cdot \mathrm{Var}(\delta z) = \frac{1}{\mathcal{V}_2^2 - (\delta z - z_1)^2} \cdot \mathrm{Var}(\delta z), \tag{B.6}$$

whereas the second term yields

$$\left(\frac{\partial \delta\phi}{\partial z_1}\right)^2 \cdot \mathrm{Var}(z_1) = \left(\frac{1}{\sqrt{\mathcal{V}_2^2 - (z_1 - \delta z)^2}} - \frac{1}{\sqrt{\mathcal{V}_1^2 - z_1^2}}\right)^2 \cdot \mathrm{Var}(z_1). \tag{B.7}$$

Thus, the complete expression for the differential phase sensitivity is given by

$$\mathrm{Var}(\delta\phi) = \frac{1}{\mathcal{V}_2^2 - (\delta z - z_1)^2} \cdot \mathrm{Var}(\delta z) + \left(\frac{1}{\sqrt{\mathcal{V}_2^2 - (z_1 - \delta z)^2}} - \frac{1}{\sqrt{\mathcal{V}_1^2 - z_1^2}}\right)^2 \cdot \mathrm{Var}(z_1). \tag{B.8}$$

Note that for $z_1 = \delta z = 0$ and $\mathcal{V}_1 = \mathcal{V}_2$, the second term vanishes, and Eq. B.8 reduces to the simple form

$$\mathrm{Var}(\delta\phi) = \frac{\mathrm{Var}(\delta z)}{\mathcal{V}^2} = \xi_{\mathrm{S}}^2 \cdot \mathrm{Var}(\delta z)_{\mathrm{class}}. \tag{B.9}$$

This shows that for differential phase estimation, the classical sensitivity is increased by the relative spin squeezing factor $\xi_{\mathrm{S}}$, in analogy to the direct spin squeezing analysis with a single Ramsey fringe.

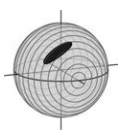

# Bibliography


[1] A. Einstein, B. Podolsky, and N. Rosen. Can Quantum-Mechanical Description of Physical Reality Be Considered Complete? *Phys. Rev.*, 47:777–780, 1935.

[2] E. Schrödinger. Discussion of Probability Relations between Separated Systems. *Mathematical Proceedings of the Cambridge Philosophical Society*, 31:555–563, 1935.

[3] J.-W. Pan, Z.-B. Chen, C.-Y. Lu, H. Weinfurter, A. Zeilinger, and M. Żukowski. Multiphoton entanglement and interferometry. *Rev. Mod. Phys.*, 84:777–838, 2012.

[4] R. Blatt and D. Wineland. Entangled states of trapped atomic ions. *Nature*, 453(7198):1008–1015, 2008.

[5] J. Esteve, C. Gross, A. Weller, S. Giovanazzi, and M. K. Oberthaler. Squeezing and entanglement in a Bose–Einstein condensate. *Nature*, 455(7217):1216–1219, 2008.

[6] B. Vlastakis, G. Kirchmair, Z. Leghtas, S. E. Nigg, L. Frunzio, S. M. Girvin, M. Mirrahimi, M. H. Devoret, and R. J. Schoelkopf. Deterministically Encoding Quantum Information Using 100-Photon Schrödinger Cat States. *Science*, 342(6158):607–610, 2013.

[7] G. Santarelli, Ph. Laurent, P. Lemonde, A. Clairon, A. G. Mann, S. Chang, A. N. Luiten, and C. Salomon. Quantum Projection Noise in an Atomic Fountain: A High Stability Cesium Frequency Standard. *Phys. Rev. Lett.*, 82:4619–4622, 1999.

[8] S. M. Dickerson, J. M. Hogan, A. Sugarbaker, D. M. S. Johnson, and M. A. Kasevich. Multiaxis Inertial Sensing with Long-Time Point Source Atom Interferometry. *Phys. Rev. Lett.*, 111:083001, 2013.

[9] D. S. Durfee, Y. K. Shaham, and M. A. Kasevich. Long-Term Stability of an Area-Reversible Atom-Interferometer Sagnac Gyroscope. *Phys. Rev. Lett.*, 97:240801, 2006.

[10] C.W. Helstrom. *Quantum Detection and Estimation Theory*. Academic Press, New York, 1976.

[11] L. Pezzé and A. Smerzi. Entanglement, Nonlinear Dynamics, and the Heisenberg Limit. *Phys. Rev. Lett.*, 102:100401, 2009.

[12] V. Giovannetti, S. Lloyd, and L. Maccone. Quantum-Enhanced Measurements: Beating the Standard Quantum Limit. *Science*, 306(5700):1330–1336, 2004.

[13] D. F. Walls. Squeezed states of light. *Nature*, 306:141–146, 1983.

[14] LIGO Scientific Collaboration et al. A gravitational wave observatory operating beyond the quantum shot-noise limit. *Nature Physics*, 7(12):962–965, 2011.

[15] R. E. Slusher, L. W. Hollberg, B. Yurke, J. C. Mertz, and J. F. Valley. Observation of Squeezed States Generated by Four-Wave Mixing in an Optical Cavity. *Phys. Rev. Lett.*, 55:2409–2412, 1985.

[16] X.-C. Yao, T.-X. Wang, P. Xu, H. Lu, G.-S. Pan, X.-H. Bao, C.-Z. Peng, C.-Y. Lu, Y.-A. Chen, and J.-W. Pan. Observation of eight-photon entanglement. *Nature Photonics*, 6(4):225–228, 2012.

[17] W.-B. Gao, C.-Y. Lu, X.-C. Yao, P. Xu, O. Gühne, A. Goebel, Y.-A. Chen, C.-Z. Peng, Z.-B. Chen, and J.-W. Pan. Experimental demonstration of a hyper-entangled ten-qubit Schrödinger cat state. *Nature Physics*, 6(5):331–335, 2010.

[18] S. Deleglise, I. Dotsenko, C. Sayrin, J. Bernu, M. Brune, J.-M. Raimond, and S. Haroche. Reconstruction of non-classical cavity field states with snapshots of their decoherence. *Nature*, 455(7212):510–514, 2008.

[19] M. Hofheinz, H. Wang, M. Ansmann, R. C. Bialczak, E. Lucero, M. Neeley, A.D. O'Connell, D. Sank, J. Wenner, J.M. Martinis, and A. N. Cleland. Synthesizing arbitrary quantum states in a superconducting resonator. *Nature*, 459(7246):546–549, 2009.

[20] H. Häffner, W. Hänsel, C.F. Roos, J. Benhelm, D. Chek-al kar, M. Chwalla, T. Körber, U. D. Rapol, M. Riebe, P. O. Schmidt, C. Becher, O. Gühne, W. Dür, and R. Blatt. Scalable multiparticle entanglement of trapped ions. *Nature*, 438(7068):643–646, 2005.

[21] D. Leibfried, E. Knill, S. Seidelin, J. Britton, R. B. Blakestad, J. Chiaverini, D. B. Hume, W. M. Itano, J. D. Jost, C. Langer, R. Ozeri, R. Reichle, and D. J. Wineland. Creation of a six-atom Schrödinger cat state. *Nature*, 438(7068):639–642, 2005.

[22] T. Monz, P. Schindler, J. T. Barreiro, M. Chwalla, D. Nigg, W. A. Coish, M. Harlander, W. Hänsel, M. Hennrich, and R. Blatt. 14-Qubit Entanglement: Creation and Coherence. *Phys. Rev. Lett.*, 106:130506, 2011.

[23] D. Leibfried, M. D. Barrett, T. Schaetz, J. Britton, J. Chiaverini, W. M. Itano, J. D. Jost, C. Langer, and D. J. Wineland. Toward Heisenberg-Limited Spectroscopy with Multiparticle Entangled States. *Science*, 304(5676):1476–1478, 2004.

[24] F. Haas, J. Volz, R. Gehr, J. Reichel, and J. Estève. Entangled States of More Than 40 Atoms in an Optical Fiber Cavity. *Science*, 344(6180):180–183, 2014.

[25] M. Kitagawa and M. Ueda. Squeezed spin states. *Phys. Rev. A*, 47:5138–5143, 1993.

[26] D. Ulam-Orgikh and M. Kitagawa. Spin squeezing and decoherence limit in Ramsey spectroscopy. *Phys. Rev. A*, 64:052106, 2001.

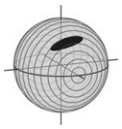

[27] C. Simon and J. Kempe. Robustness of multiparty entanglement. *Phys. Rev. A*, 65:052327, 2002.

[28] Y. Li, Y. Castin, and A. Sinatra. Optimum Spin Squeezing in Bose-Einstein Condensates with Particle Losses. *Phys. Rev. Lett.*, 100:210401, 2008.

[29] J. Ma, X. Wang, C.P. Sun, and F. Nori. Quantum spin squeezing. *Physics Reports*, 509(2-3):89 – 165, 2011.

[30] A. Kuzmich, Klaus Mølmer, and E. S. Polzik. Spin Squeezing in an Ensemble of Atoms Illuminated with Squeezed Light. *Phys. Rev. Lett.*, 79:4782–4785, 1997.

[31] J. Hald, J. L. Sørensen, C. Schori, and E. S. Polzik. Spin Squeezed Atoms: A Macroscopic Entangled Ensemble Created by Light. *Phys. Rev. Lett.*, 83:1319–1322, 1999.

[32] A. Kuzmich, L. Mandel, and N. P. Bigelow. Generation of Spin Squeezing via Continuous Quantum Nondemolition Measurement. *Phys. Rev. Lett.*, 85:1594–1597, 2000.

[33] T. Fernholz, H. Krauter, K. Jensen, J. F. Sherson, A. S. Sørensen, and E. S. Polzik. Spin Squeezing of Atomic Ensembles via Nuclear-Electronic Spin Entanglement. *Phys. Rev. Lett.*, 101:073601, 2008.

[34] J. Appel, P. J. Windpassinger, D. Oblak, U. B. Hoff, N. Kjærgaard, and E. S. Polzik. Mesoscopic atomic entanglement for precision measurements beyond the standard quantum limit. *Proceedings of the National Academy of Sciences*, 106(27):10960–10965, 2009.

[35] M. H. Schleier-Smith, I. D. Leroux, and V. Vuletić. States of an Ensemble of Two-Level Atoms with Reduced Quantum Uncertainty. *Phys. Rev. Lett.*, 104:073604, 2010.

[36] Z. Chen, J. G. Bohnet, S. R. Sankar, J. Dai, and J.+K. Thompson. Conditional Spin Squeezing of a Large Ensemble via the Vacuum Rabi Splitting. *Phys. Rev. Lett.*, 106:133601, 2011.

[37] R. J. Sewell, M. Koschorreck, M. Napolitano, B. Dubost, N. Behbood, and M. W. Mitchell. Magnetic Sensitivity Beyond the Projection Noise Limit by Spin Squeezing. *Phys. Rev. Lett.*, 109:253605, 2012.

[38] J. G. Bohnet, K. C. Cox, M. A. Norcia, J. M. Weiner, Z. Chen, and J. K. Thompson. Reduced spin measurement back-action for a phase sensitivity ten times beyond the standard quantum limit. *Nature Photonics*, 8:731Ű736, 2014.

[39] I. D. Leroux, M. H. Schleier-Smith, and V. Vuletić. Implementation of Cavity Squeezing of a Collective Atomic Spin. *Phys. Rev. Lett.*, 104:073602, 2010.

[40] A. Louchet-Chauvet, J. Appel, J. J. Renema, D. Oblak, N. Kjaergaard, and E. S. Polzik. Entanglement-assisted atomic clock beyond the projection noise limit. *New Journal of Physics*, 12(6):065032, 2010.



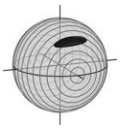

[41] I. D. Leroux, M. H. Schleier-Smith, and V. Vuletić. Orientation-Dependent Entanglement Lifetime in a Squeezed Atomic Clock. *Phys. Rev. Lett.*, 104:250801, 2010.

[42] W. Wasilewski, K. Jensen, H. Krauter, J. J. Renema, M. V. Balabas, and E. S. Polzik. Quantum Noise Limited and Entanglement-Assisted Magnetometry. *Phys. Rev. Lett.*, 104:133601, Mar 2010.

[43] H. Müntinga, H. Ahlers, M. Krutzik, A. Wenzlawski, S. Arnold, D. Becker, K. Bongs, H. Dittus, H. Duncker, N. Gaaloul, C. Gherasim, E. Giese, C. Grzeschik, T. W. Hänsch, O. Hellmig, W. Herr, S. Herrmann, E. Kajari, S. Kleinert, C. Lämmerzahl, W. Lewoczko-Adamczyk, J. Malcolm, N. Meyer, R. Nolte, A. Peters, M. Popp, J. Reichel, A. Roura, J. Rudolph, M. Schiemangk, M. Schneider, S. T. Seidel, K. Sengstock, V. Tamma, T. Valenzuela, A. Vogel, R. Walser, T. Wendrich, P. Windpassinger, W. Zeller, T. van Zoest, W. Ertmer, W. P. Schleich, and E. M. Rasel. Interferometry with Bose-Einstein Condensates in Microgravity. *Phys. Rev. Lett.*, 110:093602, 2013.

[44] A. Sørensen, L.-M. Duan, J. I. Cirac, and P. Zoller. Many-particle entanglement with Bose-Einstein condensates. *Nature*, 409:63, 2001.

[45] C. Gross, T. Zibold, E. Nicklas, J. Esteve, and M. K. Oberthaler. Nonlinear atom interferometer surpasses classical precision limit. *Nature*, 464(7292):1165–1169, 2010.

[46] M. F. Riedel, P. Böhi, Y. Li, T. W. Hänsch, A. Sinatra, and P. Treutlein. Atom-chip-based generation of entanglement for quantum metrology. *Nature*, 464(7292):1170–1173, 2010.

[47] T. Berrada, S. van Frank, R. Bücker, T. Schumm, J.-F. Schaff, and J. Schmiedmayer. Integrated Mach–Zehnder interferometer for Bose–Einstein condensates. *Nature communications*, 4, 2013.

[48] C. F. Ockeloen, R. Schmied, M. F. Riedel, and P. Treutlein. Quantum Metrology with a Scanning Probe Atom Interferometer. *Phys. Rev. Lett.*, 111:143001, 2013.

[49] B. Lücke, M. Scherer, J. Kruse, L. Pezzé, F. Deuretzbacher, P. Hyllus, O. Topic, J. Peise, W. Ertmer, J. Arlt, L. Santos, A. Smerzi, and C. Klempt. Twin Matter Waves for Interferometry Beyond the Classical Limit. *Science*, 334(6057):773–776, 2011.

[50] C. Gross, H. Strobel, E. Nicklas, T. Zibold, N. Bar-Gill, G. Kurizki, and M. K. Oberthaler. Atomic homodyne detection of continuous-variable entangled twin-atom states. *Nature*, 480(7376):219–223, 2011.

[51] B. Lücke, J. Peise, G. Vitagliano, J. Arlt, L. Santos, G. Tóth, and C. Klempt. Detecting Multiparticle Entanglement of Dicke States. *Phys. Rev. Lett.*, 112:155304, 2014.

[52] C. D. Hamley, C. S. Gerving, T. M. Hoang, E. M. Bookjans, and M. S. Chapman. Spin-nematic squeezed vacuum in a quantum gas. *Nature Physics*, 8(4):305–308, 2012.

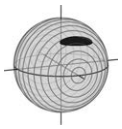

[53] R. Geiger, V. Ménoret, G. Stern, N Zahzam, P. Cheinet, B. Battelier, A. Villing, F. Moron, M. Lours, Y. Bidel, et al. Detecting inertial effects with airborne matter-wave interferometry. *Nature communications*, 2:474, 2011.

[54] A. Peters, K. Y. Chung, and S. Chu. High-precision gravity measurements using atom interferometry. *Metrologia*, 38(1):25, 2001.

[55] T. L. Gustavson, P. Bouyer, and M. A. Kasevich. Precision Rotation Measurements with an Atom Interferometer Gyroscope. *Phys. Rev. Lett.*, 78:2046–2049, 1997.

[56] D. Budker and D. F. J. Kimball. *Optical magnetometry*. Cambridge, 2013.

[57] R. Wynands and S. Weyers. Atomic fountain clocks. *Metrologia*, 42(3):S64, 2005.

[58] A. Sinatra, E. Witkowska, J.-C. Dornstetter, Yun Li, and Y. Castin. Limit of Spin Squeezing in Finite-Temperature Bose-Einstein Condensates. *Phys. Rev. Lett.*, 107:060404, 2011.

[59] M. T. Johnsson, G. R. Dennis, and J. J. Hope. Squeezing in Bose-Einstein condensates with large numbers of atoms. *New Journal of Physics*, 15(12):123024, 2013.

[60] W. Muessel, H. Strobel, D. Linnemann, D. B. Hume, and M. K. Oberthaler. Scalable Spin Squeezing for Quantum-Enhanced Magnetometry with Bose-Einstein Condensates. *Phys. Rev. Lett.*, 113:103004, 2014.

[61] H. Strobel, W. Muessel, D. Linnemann, T. Zibold, D. B. Hume, L. Pezzè, A. Smerzi, and M. K. Oberthaler. Fisher information and entanglement of non-Gaussian spin states. *Science*, 345(6195):424–427, 2014.

[62] W. Muessel, H. Strobel, M. Joos, E. Nicklas, I. Stroescu, J. Tomkovič, D. B. Hume, and M. K. Oberthaler. Optimized absorption imaging of mesoscopic atomic clouds. *Applied Physics B*, 113(1):69–73, 2013.

[63] D. B. Hume, I. Stroescu, M. Joos, W. Muessel, H. Strobel, and M. K. Oberthaler. Accurate Atom Counting in Mesoscopic Ensembles. *Phys. Rev. Lett.*, 111:253001, 2013.

[64] M. J. Steel and M. J. Collett. Quantum state of two trapped Bose-Einstein condensates with a Josephson coupling. *Phys. Rev. A*, 57:2920–2930, 1998.

[65] J. I. Cirac, M. Lewenstein, K. Mølmer, and P. Zoller. Quantum superposition states of Bose-Einstein condensates. *Phys. Rev. A*, 57:1208–1218, 1998.

[66] G. J. Milburn, J. Corney, E. M. Wright, and D. F. Walls. Quantum dynamics of an atomic Bose-Einstein condensate in a double-well potential. *Phys. Rev. A*, 55:4318–4324, 1997.

[67] H.J. Lipkin, N. Meshkov, and A.J. Glick. Validity of many-body approximation methods for a solvable model: (I). Exact solutions and perturbation theory . *Nuclear Physics*, 62(2):188 – 198, 1965.



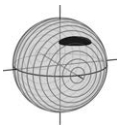

[68] A. Smerzi, S. Fantoni, S. Giovanazzi, and S. R. Shenoy. Quantum Coherent Atomic Tunneling between Two Trapped Bose-Einstein Condensates. *Phys. Rev. Lett.*, 79:4950–4953, 1997.

[69] S. Raghavan, A. Smerzi, S. Fantoni, and S. R. Shenoy. Coherent oscillations between two weakly coupled Bose-Einstein condensates: Josephson effects, $\pi$ oscillations, and macroscopic quantum self-trapping. *Phys. Rev. A*, 59:620–633, 1999.

[70] T. Zibold, E. Nicklas, C. Gross, and M. K. Oberthaler. Classical Bifurcation at the Transition from Rabi to Josephson Dynamics. *Phys. Rev. Lett.*, 105:204101, 2010.

[71] F. T. Arecchi, E. Courtens, R. Gilmore, and H. Thomas. Atomic Coherent States in Quantum Optics. *Phys. Rev. A*, 6:2211–2237, 1972.

[72] R. H. Dicke. Coherence in Spontaneous Radiation Processes. *Phys. Rev.*, 93:99–110, 1954.

[73] J. M. Radcliffe. Some properties of coherent spin states. *Journal of Physics A: General Physics*, 4(3):313, 1971.

[74] W.-M. Zhang, D. H. Feng, and R. Gilmore. Coherent states: Theory and some applications. *Rev. Mod. Phys.*, 62:867–927, 1990.

[75] C. T. Lee. Q representation of the atomic coherent states and the origin of fluctuations in superfluorescence. *Phys. Rev. A*, 30:3308–3310, 1984.

[76] D. J. Wineland, J. J. Bollinger, W. M. Itano, F. L. Moore, and D. J. Heinzen. Spin squeezing and reduced quantum noise in spectroscopy. *Phys. Rev. A*, 46:R6797–R6800, 1992.

[77] A. S. Sørensen and K. Mølmer. Entanglement and Extreme Spin Squeezing. *Phys. Rev. Lett.*, 86:4431–4434, 2001.

[78] A. Micheli, D. Jaksch, J. I. Cirac, and P. Zoller. Many-particle entanglement in two-component Bose-Einstein condensates. *Phys. Rev. A*, 67:013607, 2003.

[79] M. Albiez, R. Gati, J. Fölling, S. Hunsmann, M. Cristiani, and M. K. Oberthaler. Direct Observation of Tunneling and Nonlinear Self-Trapping in a Single Bosonic Josephson Junction. *Phys. Rev. Lett.*, 95:010402, 2005.

[80] S. Levy, E. Lahoud, I. Shomroni, and J. Steinhauer. The ac and dc Josephson effects in a Bose–Einstein condensate. *Nature*, 449(7162):579–583, 2007.

[81] T. Zibold. *Classical Bifurcation and Entanglement Generation in an internal Bosonic Josephson Junction*. PhD thesis, University of Heidelberg, 2012.

[82] B. Juliá-Díaz, T. Zibold, M. K. Oberthaler, M. Melé-Messeguer, J. Martorell, and A. Polls. Dynamic generation of spin-squeezed states in bosonic Josephson junctions. *Phys. Rev. A*, 86:023615, 2012.

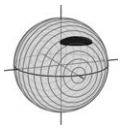

[83] A. Weller. *Dynamics and Interaction of Dark Solitons in Bose-Einstein Condensates*. PhD thesis, University of Heidelberg, 2009.

[84] W. Petrich, M. H. Anderson, J. R. Ensher, and E. A. Cornell. Stable, Tightly Confining Magnetic Trap for Evaporative Cooling of Neutral Atoms. *Phys. Rev. Lett.*, 74:3352–3355, 1995.

[85] M. Erhard, H. Schmaljohann, J. Kronjäger, K. Bongs, and K. Sengstock. Measurement of a mixed-spin-channel Feshbach resonance in $^{87}\mathrm{Rb}$. *Phys. Rev. A*, 69:032705, 2004.

[86] A. Widera, O. Mandel, M. Greiner, S. Kreim, T. W. Hänsch, and I. Bloch. Entanglement Interferometry for Precision Measurement of Atomic Scattering Properties. *Phys. Rev. Lett.*, 92:160406, 2004.

[87] C. Chin, R. Grimm, P. Julienne, and E. Tiesinga. Feshbach resonances in ultracold gases. *Rev. Mod. Phys.*, 82:1225–1286, 2010.

[88] S. Inouye, M.R. Andrews, J. Stenger, H.-J. Miesner, D.M. Stamper-Kurn, and W. Ketterle. Observation of Feshbach resonances in a Bose–Einstein condensate. *Nature*, 392(6672):151–154, 1998.

[89] C. Gross. *Spin squeezing and non-linear atom interferometry with Bose-Einstein condensates*. PhD thesis, University of Heidelberg, 2010.

[90] T. Zibold. Active magnetic shielding and optical magnetometry. Master's thesis, University of Heidelberg, 2007.

[91] S. Tojo, T. Hayashi, T. Tanabe, T. Hirano, Y. Kawaguchi, H. Saito, and M. Ueda. Spin-dependent inelastic collisions in spin-2 Bose-Einstein condensates. *Phys. Rev. A*, 80:042704, 2009.

[92] S. Tojo, Y. Taguchi, Y. Masuyama, T. Hayashi, H. Saito, and T. Hirano. Controlling phase separation of binary Bose-Einstein condensates via mixed-spin-channel Feshbach resonance. *Phys. Rev. A*, 82:033609, 2010.

[93] F. Dalfovo, S. Giorgini, L. P. Pitaevskii, and S. Stringari. Theory of Bose-Einstein condensation in trapped gases. *Rev. Mod. Phys.*, 71:463–512, 1999.

[94] J. Söding, D. Guéry-Odelin, P. Desbiolles, F. Chevy, H. Inamori, and J. Dalibard. Three-body decay of a rubidium Bose–Einstein condensate. *Applied Physics B*, 69(4):257–261, 1999.

[95] W. Ketterle, D.S. Durfee, and D.M. Stamper-Kurn. *Proceedings of the International School of Physics "Enrico Fermi": Making, probing and understanding Bose-Einstein condensates*. IOS Press, Amsterdam, 1999.

[96] T. Ottenstein. A New Objective for High Resolution Imaging of Bose-Einstein Condensates. Master's thesis, University of Heidelberg, 2006.



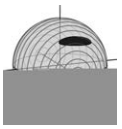

[97] G. Reinaudi, T. Lahaye, Z. Wang, and D. Guéry-Odelin. Strong saturation absorption imaging of dense clouds of ultracold atoms. *Optics letters*, 32(21):3143–3145, 2007.

[98] C. F. Ockeloen, A. F. Tauschinsky, R. J. C. Spreeuw, and S. Whitlock. Detection of small atom numbers through image processing. *Phys. Rev. A*, 82:061606, 2010.

[99] M. Joos. Phase contrast imaging of mesoscopic Bose-Einstein condensates. Master's thesis, University of Heidelberg, 2013.

[100] W. M. Itano, J. C. Bergquist, J. J. Bollinger, J. M. Gilligan, D. J. Heinzen, F. L. Moore, M. G. Raizen, and D. J. Wineland. Quantum projection noise: Population fluctuations in two-level systems. *Phys. Rev. A*, 47:3554–3570, 1993.

[101] D. J. Wineland, J. J. Bollinger, W. M. Itano, and D. J. Heinzen. Squeezed atomic states and projection noise in spectroscopy. *Phys. Rev. A*, 50:67–88, 1994.

[102] X. Wang and B. C. Sanders. Spin squeezing and pairwise entanglement for symmetric multiqubit states. *Phys. Rev. A*, 68:012101, 2003.

[103] J. K. Korbicz, J. I. Cirac, and M. Lewenstein. Spin Squeezing Inequalities and Entanglement of $N$ Qubit States. *Phys. Rev. Lett.*, 95:120502, 2005.

[104] N. Killoran, M. Cramer, and B. Plenio, M.˙ Extracting Entanglement from Identical Particles. *Phys. Rev. Lett.*, 112:150501, 2014.

[105] A. M. Kaufman, R. P. Anderson, Thomas M. Hanna, E. Tiesinga, P. S. Julienne, and D. S. Hall. Radio-frequency dressing of multiple Feshbach resonances. *Phys. Rev. A*, 80:050701, 2009.

[106] K. Mølmer, Y. Castin, and J. Dalibard. Monte Carlo wave-function method in quantum optics. *J. Opt. Soc. Am. B*, 10(3):524–538, 1993.

[107] K. Mølmer and Y. Castin. Monte Carlo wavefunctions in quantum optics. *Quantum and Semiclassical Optics: Journal of the European Optical Society Part B*, 8(1):49, 1996.

[108] C.S. Gerving, T.M. Hoang, B.J. Land, M. Anquez, C.D. Hamley, and M.S. Chapman. Non-equilibrium dynamics of an unstable quantum pendulum explored in a spin-1 Bose-Einstein condensate. *Nature communications*, 3:1169, 2012.

[109] V. S. Shchesnovich and M. Trippenbach. Fock-space WKB method for the boson Josephson model describing a Bose-Einstein condensate trapped in a double-well potential. *Phys. Rev. A*, 78:023611, 2008.

[110] E. W.. Streed, A. P. Chikkatur, T. L. Gustavson, M. Boyd, Y. Torii, D. Schneble, G. K. Campbell, D. E. Pritchard, and W. Ketterle. Large atom number Bose-Einstein condensate machines. *Review of Scientific Instruments*, 77(2):–, 2006.

[111] P. W. Graham, J. M. Hogan, M. A. Kasevich, and S. Rajendran. New Method for Gravitational Wave Detection with Atomic Sensors. *Phys. Rev. Lett.*, 110:171102, 2013.

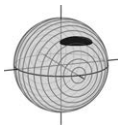

[112] S. Dimopoulos, P. W. Graham, J. M. Hogan, and M. A. Kasevich. Testing General Relativity with Atom Interferometry. *Phys. Rev. Lett.*, 98:111102, 2007.

[113] A. Sugarbaker, S. M. Dickerson, J. M. Hogan, D. M. S. Johnson, and M. A. Kasevich. Enhanced Atom Interferometer Readout through the Application of Phase Shear. *Phys. Rev. Lett.*, 111:113002, 2013.

[114] S. Aigner, L. Della Pietra, Y. Japha, O. Entin-Wohlman, T. David, R. Salem, R. Folman, and J. Schmiedmayer. Long-Range Order in Electronic Transport Through Disordered Metal Films. *Science*, 319(5867):1226–1229, 2008.

[115] A. Sinatra, Y. Castin, and E. Witkowska. Limit of spin squeezing in trapped Bose-Einstein condensates. *EPL (Europhysics Letters)*, 102(4):40001, 2013.

[116] Alexander D. Cronin, Jörg Schmiedmayer, and David E. Pritchard. Optics and interferometry with atoms and molecules. *Rev. Mod. Phys.*, 81:1051–1129, 2009.

[117] N. F. Ramsey. A Molecular Beam Resonance Method with Separated Oscillating Fields. *Phys. Rev.*, 78:695–699, 1950.

[118] H. Lee, P. Kok, and J. P. Dowling. A quantum Rosetta stone for interferometry. *J. Mod. Opt.*, 49:2325–2338, 2002.

[119] J. J . Bollinger, W. M. Itano, D. J. Wineland, and D. J. Heinzen. Optimal frequency measurements with maximally correlated states. *Phys. Rev. A*, 54:R4649–R4652, 1996.

[120] K. M. Mertes, J. W. Merrill, R. Carretero-González, D. J. Frantzeskakis, P. G. Kevrekidis, and D. S. Hall. Nonequilibrium Dynamics and Superfluid Ring Excitations in Binary Bose-Einstein Condensates. *Phys. Rev. Lett.*, 99:190402, 2007.

[121] M. Egorov, B. Opanchuk, P. Drummond, B. V. Hall, P. Hannaford, and A. I. Sidorov. Measurement of $s$-wave scattering lengths in a two-component Bose-Einstein condensate. *Phys. Rev. A*, 87:053614, 2013.

[122] E. G. M. van Kempen, S. J. J. M. F. Kokkelmans, D. J. Heinzen, and B. J. Verhaar. Interisotope Determination of Ultracold Rubidium Interactions from Three High-Precision Experiments. *Phys. Rev. Lett.*, 88:093201, 2002.

[123] A. Widera, F. Gerbier, S. Fölling, T. Gericke, O. Mandel, and I. Bloch. Precision measurement of spin-dependent interaction strengths for spin-1 and spin-2 87 Rb atoms. *New Journal of Physics*, 8(8):152, 2006.

[124] M. Vengalattore, J. M. Higbie, S. R. Leslie, J. Guzman, L. E. Sadler, and D. M. Stamper-Kurn. High-Resolution Magnetometry with a Spinor Bose-Einstein Condensate. *Phys. Rev. Lett.*, 98:200801, 2007.

[125] J. R. Maze, P. L. Stanwix, J. S. Hodges, S. Hong, J. M. Taylor, P. Cappellaro, L. Jiang, M. V. Gurudev Dutt, E. Togan, A. S. Zibrov, et al. Nanoscale magnetic sensing with an individual electronic spin in diamond. *Nature*, 455(7213):644–647, 2008.



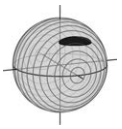

[126] G. Balasubramanian, P. Neumann, D. Twitchen, M. Markham, R. Kolesov, N. Mizuochi, J. Isoya, J. Achard, J. Beck, J. Tissler, et al. Ultralong spin coherence time in isotopically engineered diamond. *Nature materials*, 8(5):383–387, 2009.

[127] S. Steinert, F. Dolde, P. Neumann, A. Aird, B. Naydenov, G. Balasubramanian, F. Jelezko, and J. Wrachtrup. High sensitivity magnetic imaging using an array of spins in diamond. *Review of Scientific Instruments*, 81(4):043705, 2010.

[128] V. M. Acosta, E. Bauch, A. Jarmola, L. J. Zipp, M. P. Ledbetter, and D. Budker. Broadband magnetometry by infrared-absorption detection of nitrogen-vacancy ensembles in diamond. *Applied Physics Letters*, 97(17):174104, 2010.

[129] L. M. Pham, N. Bar-Gill, D. Le Sage, C. Belthangady, A. Stacey, M. Markham, D. J. Twitchen, M. D. Lukin, and R. L. Walsworth. Enhanced metrology using preferential orientation of nitrogen-vacancy centers in diamond. *Phys. Rev. B*, 86:121202, 2012.

[130] K. Jensen, N. Leefer, A. Jarmola, Y. Dumeige, M. Acosta, V. P. Kehayias, B. Patton, and D. Budker. Cavity-Enhanced Room-Temperature Magnetometry Using Absorption by Nitrogen-Vacancy Centers in Diamond. *Phys. Rev. Lett.*, 112:160802, 2014.

[131] H. J. Mamin, T. H. Oosterkamp, M. Poggio, C. L. Degen, C. T. Rettner, and D. Rugar. Isotope-Selective Detection and Imaging of Organic Nanolayers. *Nano Letters*, 9(8):3020–3024, 2009.

[132] V. Shah, S. Knappe, P. D. D. Schwindt, and J. Kitching. Subpicotesla atomic magnetometry with a microfabricated vapour cell. *Nature Photonics*, 1(11):649–652, 2007.

[133] M. L. Terraciano, M. Bashkansky, and F. K. Fatemi. Faraday spectroscopy of atoms confined in a dark optical trap. *Phys. Rev. A*, 77:063417, 2008.

[134] H. B. Dang, A. C. Maloof, and M. V. Romalis. Ultrahigh sensitivity magnetic field and magnetization measurements with an atomic magnetometer. *Applied Physics Letters*, 97(15):151110, 2010.

[135] F. Baudenbacher, L. E. Fong, J. R. Holzer, and M. Radparvar. Monolithic low-transition-temperature superconducting magnetometers for high resolution imaging magnetic fields of room temperature samples. *Applied Physics Letters*, 82(20):3487–3489, 2003.

[136] M. I. Faley, U. Poppe, K. Urban, D. N. Paulson, and R. L. Fagaly. A New Generation of the HTS Multilayer DC-SQUID Magnetometers and Gradiometers. *Journal of Physics: Conference Series*, 43(1):1199, 2006.

[137] S. Wildermuth, S. Hofferberth, I. Lesanovsky, S. Groth, P. Krüger, J. Schmiedmayer, and I. Bar-Joseph. Sensing electric and magnetic fields with Bose-Einstein condensates. *Applied Physics Letters*, 88(26):264103, 2006.

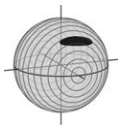

[138] Y. Eto, H. Ikeda, H. Suzuki, S. Hasegawa, Y. Tomiyama, S. Sekine, M. Sadgrove, and T. Hirano. Spin-echo-based magnetometry with spinor Bose-Einstein condensates. *Phys. Rev. A*, 88:031602, 2013.

[139] A. Sandhu, A. Okamoto, I. Shibasaki, and A. Oral. Nano and micro Hall-effect sensors for room-temperature scanning hall probe microscopy. *Microelectronic Engineering*, 73-74(0):524–528, 2004.

[140] J. R. Kirtley, M. B. Ketchen, K. G. Stawiasz, J. Z. Sun, W. J. Gallagher, S. H. Blanton, and S. J. Wind. High-resolution scanning SQUID microscope. *Applied Physics Letters*, 66(9):1138–1140, 1995.

[141] D. Le Sage, K. Arai, D. R. Glenn, S. J. DeVience, L. M. Pham, L. Rahn-Lee, M. D. Lukin, A. Yacoby, A. Komeili, and R. L. Walsworth. Optical magnetic imaging of living cells. *Nature*, 496(7446):486–489, 2013.

[142] M. Koschorreck, M. Napolitano, B. Dubost, and M. W. Mitchell. High resolution magnetic vector-field imaging with cold atomic ensembles. *Applied Physics Letters*, 98(7):074101, 2011.

[143] G. T. Foster, J. B. Fixler, J. M. McGuirk, and M. A. Kasevich. Method of phase extraction between coupled atom interferometers using ellipse-specific fitting. *Opt. Lett.*, 27(11):951–953, 2002.

[144] G.. Engelhardt, V.M. Bastidas, and T. Brandes. Signatures of the excited-state quantum phase transition in the periodic dynamics of the Lipkin-Meshkov-Glick model. *arXiv preprint arXiv:1405.3514*, 2014.

[145] A. Osterloh, L. Amico, G. Falci, and R. Fazio. Scaling of entanglement close to a quantum phase transition. *Nature*, 416(6881):608–610, 2002.

[146] T. J. Osborne and M. A. Nielsen. Entanglement in a simple quantum phase transition. *Phys. Rev. A*, 66:032110, 2002.

[147] N. Bar-Gill, C. Gross, I. Mazets, M. Oberthaler, and G. Kurizki. Einstein-Podolsky-Rosen Correlations of Ultracold Atomic Gases. *Phys. Rev. Lett.*, 106:120404, 2011.

[148] Q. Y. He, M. D. Reid, T. G. Vaughan, C. Gross, M. Oberthaler, and P. D. Drummond. Einstein-Podolsky-Rosen Entanglement Strategies in Two-Well Bose-Einstein Condensates. *Phys. Rev. Lett.*, 106:120405, 2011.

[149] H. Kurkjian, K. Pawłowski, A. Sinatra, and P. Treutlein. Spin squeezing and Einstein-Podolsky-Rosen entanglement of two bimodal condensates in state-dependent potentials. *Phys. Rev. A*, 88:043605, 2013.

[150] M. Cheneau, P. Barmettler, D. Poletti, M. Endres, P. Schauß, T. Fukuhara, C. Gross, I. Bloch, C. Kollath, and S. Kuhr. Light-cone-like spreading of correlations in a quantum many-body system. *Nature*, 481(7382):484–487, 2012.



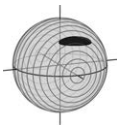

[151] T. Langen, R. Geiger, M. Kuhnert, B. Rauer, and J. Schmiedmayer. Local emergence of thermal correlations in an isolated quantum many-body system. *Nature Physics*, 2013.

[152] G. Breit and I. I. Rabi. Measurement of Nuclear Spin. *Phys. Rev.*, 38:2082–2083, 1931.

[153] P. J. Mohr, B. N. Taylor, and D. B. Newell. CODATA Recommended Values of the Fundamental Physical Constants: 2010a). *Journal of Physical and Chemical Reference Data*, 41(4), 2012.

[154] C. W. White, W. M. Hughes, G. S. Hayne, and H. G. Robinson. Determination of $g$-Factor Ratios for Free $\mathrm{Rb}^{85}$ and $\mathrm{Rb}^{87}$ Atoms. *Phys. Rev.*, 174:23–32, 1968.

[155] E. Arimondo, M. Inguscio, and P. Violino. Experimental determinations of the hyperfine structure in the alkali atoms. *Rev. Mod. Phys.*, 49:31–75, 1977.

[156] S. Bize, Y. Sortais, M. S. Santos, C. Mandache, A. Clairon, and C. Salomon. High-accuracy measurement of the 87 Rb ground-state hyperfine splitting in an atomic fountain. *EPL (Europhysics Letters)*, 45(5):558, 1999.

# Danksagung

Soll zwischen uns kein fernster Zwist sich regen,
Ich liebe mir den Zaubrer zum Collegen.

*Schatzmeister zu Faust*
*J. W. von Goethe, 'Faust – Der Tragödie zweiter Teil'*

Im Laufe der letzten Jahre haben mir so viele zauberhafte Menschen ihre Unterstützung zukommen lassen, dass es mir schwer fällt, meinen Dank auf so wenig Papier zusammenzufassen.
Zu allererst gilt mein Dank Markus, der mich für die Quanten, die kalten Atome und die 'Quetscherei' begeistert und mir diese Arbeit ermöglicht hat. Die Mischung aus Physik-Begeisterung, kritischem Hinterfragen und den zugehörigen Antworten, die tiefgründigen Diskussionen und das große Vertrauen haben mich hervorragend durch die Promotionszeit geführt.
Philipp Treutlein danke ich vielmals für die freundliche und schnelle Zusage zur Übernahme des Zweitgutachtens trotz der weiten Anreise zur Prüfung.

Ohne meine fantastischen BEC-Kollegen wäre diese Arbeit nicht im Ansatz zu Stande gekommen. Die intensiven Diskussionen und ständigen Anregungen, die neuen Denkanstösse, die fruchtbare Laborarbeit auch in komplizierten Situationen, aber auch die lustigen und schönen Momente (hier drei meiner Favoriten: die Laborspitzmaus, das ablenkungsgesicherte Coherent-Poster für den Kühlschrank und die Photoshop-Kunstwerke) haben entscheidenden Anteil daran – auch, weil sich das Experiment trotz ständigem Fiepen stets kooperativ zeigte. Ich danke euch vielstmals für all die Zauberei, eure immer offenen Ohren und die in allen menschlichen und fachlichen Dingen tolle Zusammenarbeit!

Alle Matterwaver haben mich nicht nur in physikalischer und fachlicher Sicht großartig unterstützt. Ich denke gerne an die vielen tollen gemeinsamen Momente zurück - ob beim individuellen oder dem kollektiven Frühstück und dem 'Kaffeekranz', der Schulterglatze, auf den Gruppen- und Institutsausflügen, den Grill-Schwenker-Abenden, der Trennseitenerstellung, den Pizzatagen (auch wenn ich meistens kurz vor dem Verhungern war), oder bei den Heimwegsunterhaltungen. Außerdem verdanke ich der *Kühlschrank-Kommune* die in finanzieller Hinsicht vielleicht beste und die mit Sicherheit *exquisit*esten und wohlschmeckendesten Investitionen der letzten Jahre! Abgesehen davon besitze ich nun den vermutlich schönsten Tisch im ganzen Institut...

Zutiefst dankbar bin ich auch für die große Unterstützung und die Hilfe, die mir bei allen Verwaltungs-, EDV-, Organisations- und sonstigen Papierkramfragen zuteil wurde, und die mir das Promovieren sehr erleichtert hat.

Der Studienstiftung des deutschen Volkes, insbesondere der Promotionsbetreuung um Herrn Dr. Peter Antes und Herrn Dr. Hans-Ottmar Weyand, bin ich zu großem Dank verpflichtet – für die tiefgehende Förderung, die so viele Dinge möglich gemacht hat, und die stets freundliche, hilfsbereite und unkomplizierte Betreuung.

Unendlich dankbar bin ich allen Menschen, die mich auch außerhalb von Labor und Büro während des Studiums und der Doktorarbeit begleitet haben – meinen tollen Freunden für die vielen schönen Stunden, aber vor allem auch meinen Geschwistern und meinen Eltern, die mir all das erst ermöglicht haben und jederzeit mit Rat und Tat zur Seite standen. Es ist schön, solch ein Zuhause zu haben!
Ganz besonders danke ich der einen Frau, ohne die die Welt nicht halb so schön wäre, und mit der ich so gerne durch all die warmen und auch die kaalten Tage gehe.

# Erklärung

Ich versichere, dass ich diese Arbeit selbstständig verfasst habe und keine anderen als die angegebenen Quellen und Hilfsmittel benutzt habe.

Heidelberg, den 06.10.2014 . . . . . .